EFDC+ Propeller Wash Module
White Paper

January 26, 2023

This page left intentionally blank.

Abstract

DSI, LLC has developed a numerical algorithm for propeller wash modeling to simulate flow and sediment transport patterns due to ship traffic, integrating this algorithm into Environmental Fluid Dynamics Code Plus (EFDC+). In this method, propeller wash velocity profiles for each ship are computed based on Hamill's approaches (Hamill, 1987; Hamill and Kee, 2016; Hamill et al., 2015) and other empirical equations (Fuehrer and Römisch, 1977; Hashmi et al., 2007; Lam et al., 2011; Maynord, 2000; Stewart, 1992; Toutant, 1982). Using these velocity profiles, the resultant shear stress at the water-sediment interface is calculated using the Maynord (2000) method. Given the bottom shear stress, sediment transport processes due to the propeller wash are then computed following either van Rijn's sediment transport equations (van Rijn, 1984a,b,c) or the Sediment Dynamics Algorithms developed by Ziegler, Lick, and Jones (SEDZLJ) (Jones and Lick, 2001). These propeller wash results are fully coupled to the three-dimensional hydrodynamic and sediment transport computation in EFDC+. As a result, the EFDC+ propeller wash module can dynamically simulate combinations of propeller wash-induced processes, such as sediment resuspension and bed scour due to ship movement, subsequent transport behaviors in the water column (e.g., advection, diffusion, settling), and redeposition in the sediment bed.

Several case studies, including a flume experiment (Hong et al., 2016), a San Diego Bay field test (Wang et al., 2016), and Washington State ferry operations (Kastner et al., 2019), demonstrated that the EFDC+ propeller wash module can reasonably reproduce observed propeller wash data (i.e., flow velocity, shear stress, and erosion depth). Other case studies presented here also confirmed that the EFDC+ propeller wash approach works correctly with van Rijn's sediment transport theories (van Rijn, 1984a,b,c) and SEDZLJ methodology (Jones and Lick, 2001). Based on these findings, it can be concluded that the EFDC+ propeller wash module provides a reliable representation of the sediment transport processes induced by propeller wash, including scour, bedload, sediment resuspension, and movements of the resuspended sediments under various conditions. The EFDC+ propeller wash modeling features will be beneficial for researchers, engineers, and regulators in their efforts to properly evaluate propeller wash effects for contaminant remediation planning, scour mitigation, and structure design.

Contents

CONTENTS

Acknowledgments

References

List of Figures

LIST OF FIGURES

List of Tables

List of Abbreviations

2D   Two-dimensional

3D   Three-dimensional

ADV   Acoustic Doppler Velocimeter

ADVP   Acoustic Doppler Velocity Profiler

AIS   Automatic Identification System

CRADA   Cooperative Research And Development Agreement

DEM   Digital Elevation Model

DSI   DSI, LLC

EEMS   EFDC_Explorer Modeling System

EFDC   Environmental Fluid Dynamics Code

EFDC+   Environmental Fluid Dynamics Code Plus

GUI   Graphic User Interface

hp   Horsepower

Hz   Hertz

JSON   JavaScript Object Notation

M/V   Motor Vessel

MLLW   Mean Lower Low Water

MMSI   Maritime Mobile Service Identity

NIWC-Pacific Naval Information Warfare Center Pacific

NSE	Nash-Sutcliffe Efficiency
PDT	Pacific Daylight Time
PIV	Particle Image Velocimetry
rpm	Revolutions Per Minute
rps	Revolutions Per Second
SEDZLJ	Sediment Dynamics Algorithms Developed By Ziegler, Lick, And Jones
TKE	Turbulent Kinetic Energy
TSS	Total Suspended Sediments
UTM	Universal Transverse Mercator
UW	University Of Washington
WSDOT	Washington State Department Of Transportation
WSF	Washington State Ferries

Chapter 1

Introduction

1.1. Background

Propeller wash is the flow generated behind a rotating propeller. The propeller wash from ships may significantly impact the sediment bed in water systems, especially in areas of substantial ship traffic. The propeller wash can cause resuspension and redistribution of contaminated sediments, as documented in numerous field studies over the years (e.g., San Diego Bay, Gowanus Canal, Newtown Creek, Lower Duwamish River, and Portland Harbor Superfund sites). One such study conducted in San Diego Bay demonstrated that berthing/docking at only three naval piers resuspended a total of 26 tons per day of sediments into the water column (Wang et al., 2016). The resuspended contaminated sediments can be further transported by ship traffic-induced currents in addition to ambient flows, acting as a significant source of recontamination at other locations nearby (Michelsen et al., 1998). In addition, propeller wash has been identified as the primary cause of scour around quay structures (e.g., piers and docks); such scour may result in structural instability, or even failure (PIANC, 2015). Research on propeller wash-induced scour at the Kingston Ferry Terminal in Washington state (Kastner et al., 2019) observed that an undersea cliff face at a ferry slip had migrated shoreward in recent years; the study then showed that the propeller wash associated with ferries' arrivals and departures had up to 10 to 30 times higher water velocities and up to 10 to 100 times higher resulting shear stresses than ambient conditions, with serious potential impacts for the seabed.

Over the decades, several approaches have been proposed to estimate the impacts of propeller wash on sediment resuspension (Garcia et al., 1999; Gucinski, 1982; Hong et al., 2016) and seabed scours around quay walls (Blaauw and van de Kaa, 1978; Fuehrer and Römisch, 1977; Hamill, 1987; Hong et al., 2013; Verhey et al., 1987). These studies have relied primarily on experiment results and have provided laboratory-based empirical formulations for propeller wash effect estimation. Recently, numerical modeling studies of propeller wash have been conducted to compute flow and sediment transport patterns due to propeller wash in nearshore areas, linking them to numerical sediment transport models (Chadwick et al., 2008; Maynord, 2000; Wang et al., 2016). However, most modeling approaches have been limited to representations of propeller wash that are uncoupled with the sediment transport models. Specifically, the existing approaches are es-

tablished based on empirical formulations that only address propeller wash-induced velocity and shear stress at the sediment bed, which prevents dynamic coupling to the far-field transport processes. For example, the modelers calculated the propeller wash sediment resuspension using the empirical equations externally (i.e., by hand), and then they manually added this as a source term to a far-field model simulation for subsequent sediment transport (Chadwick et al., 2008). Additionally, most current modeling efforts are limited to steady-state flow conditions, neglecting propeller wash-induced momentum for hydrodynamic flow field computation. Moreover, their applications are frequently limited to a single type of vessel, with additional limitations in modeling ship paths.

1.2. Objective

DSI, LLC (DSI) has developed a numerical algorithm for propeller wash modeling, integrating this algorithm into Environmental Fluid Dynamics Code Plus (EFDC+) as a module. This algorithm is fully coupled to a three-dimensional (3D) hydrodynamic and sediment transport computation in EFDC+. Therefore, EFDC+ with the propeller wash module can dynamically simulate combinations of propeller wash-induced processes, such as sediment resuspension and bed scour due to ship traffic, subsequent transport processes in the water column (e.g., advection, diffusion, settling), and redeposition in the sediment bed, as illustrated in Figure 1.1.
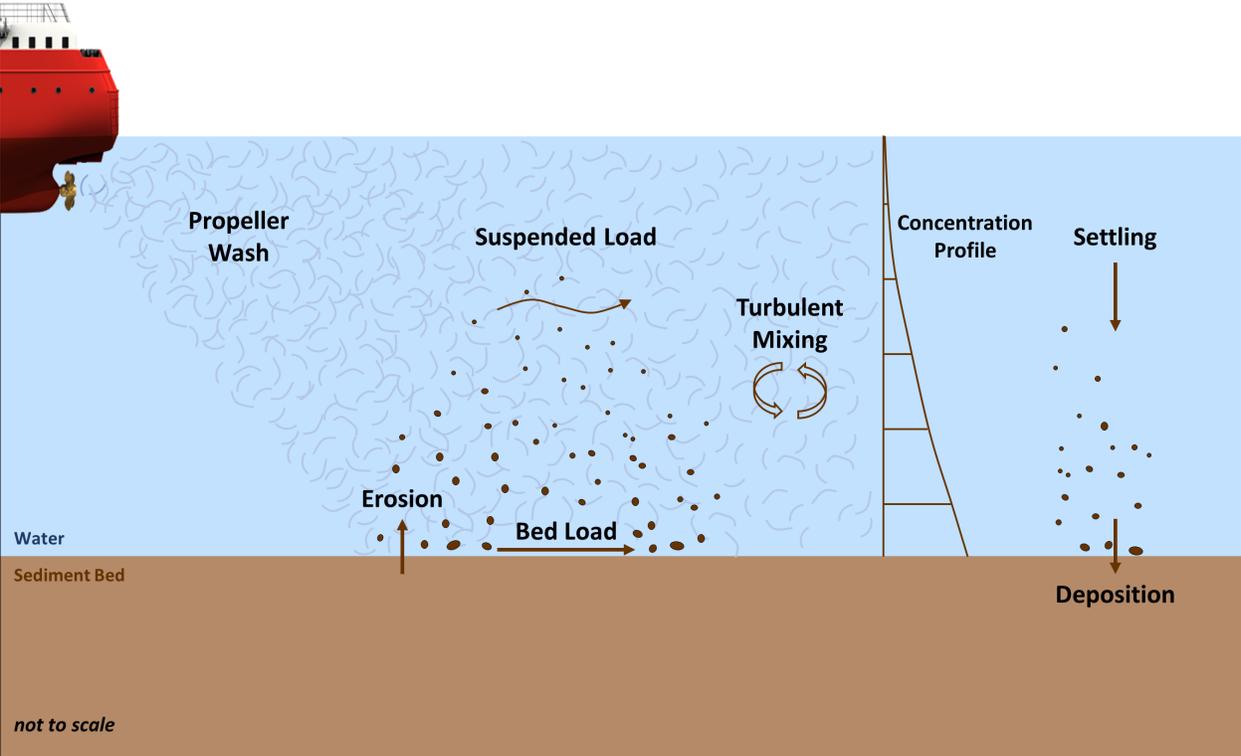
Figure 1.1: Schematic diagram of propeller wash-induced sediment transport processes.

Major capabilities of the EFDC+ propeller wash modeling features are highlighted below.

- Computes propeller wash effects based on an independent sub-grid mesh for each ship and integrates them into general model grid cells;

- Addresses any number of ships simultaneously for the characteristics of ship and propeller properties illustrated in Figures 1.2 and 1.3;

- Specifies ship paths by interpolating Automatic Identification System (AIS) or user-defined ship tracking data;

- Calculates propeller wash-induced shear stress, including ambient currents;

- Applies a superposition approach to address multiple-propeller impacts;

- Computes sediment transport processes linked to the Original Environmental Fluid Dynamics Code (EFDC) Sediment Transport module (van Rijn, 1984a,b,c) and the Sediment Dynamics Algorithms developed by Ziegler, Lick, and Jones (SEDZLJ) module (Jones and Lick, 2001);

- Simulates geomorphic feedback for the Original EFDC Sediment Transport and the SEDZLJ modules; and

- Incorporates propeller wash momentum into the 3D hydrodynamic flow field.

The fully coupled modeling features of the EFDC+ propeller wash module will be beneficial for researchers, engineers, and regulators in their efforts to properly evaluate propeller wash effects for contaminant remediation planning, scour mitigation, and structure design. To assist in developing, running, and analyzing EFDC+ propeller wash models, EFDC_Explorer Modeling System (EEMS) software provides pre-and post-processing tools with a Graphic User Interface (GUI). More information about the EEMS software is available online (www.eemodelingsystem.com).

This document provides comprehensive information on the EFDC+ propeller wash module as follows. Chapter 2 describes the theoretical basis for the propeller wash velocity solutions used in the EFDC+ propeller wash module. Chapter 3 addresses the algorithmic structures and implementation procedures of the EFDC+ propeller wash module. Chapter 4 provides the details of four input files required for the propeller wash simulation using EFDC+, and this chapter also suggests general guidelines for ship and propeller specifications that can be used as model inputs when the required information is not available. Chapter 6 presents several case studies that demonstrate and validate the EFDC+ propeller wash modeling features coupled to hydrodynamic and sediment transport processes.
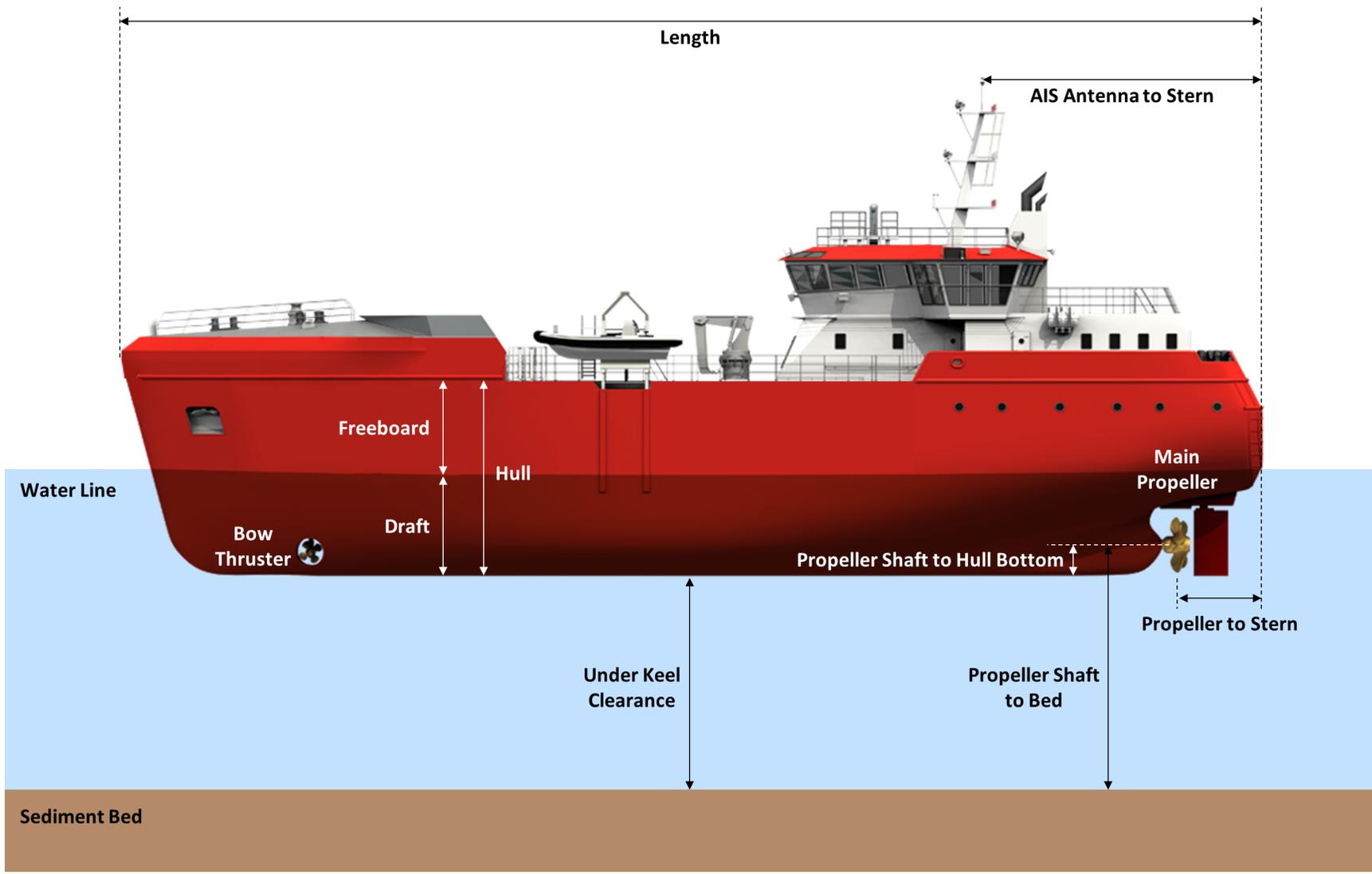
Figure 1.2: Definition for key ship properties (side view). The ship image is adapted from Damen Shipyards (2021).

Beam

Number of Propellers = 2
Number of Propeller Blades = 4

Propeller Hub Diameter

Water Line

Propeller Depth

Propeller Diameter

Propeller Shaft to Bed

Distance Between Propellers

Sediment Bed
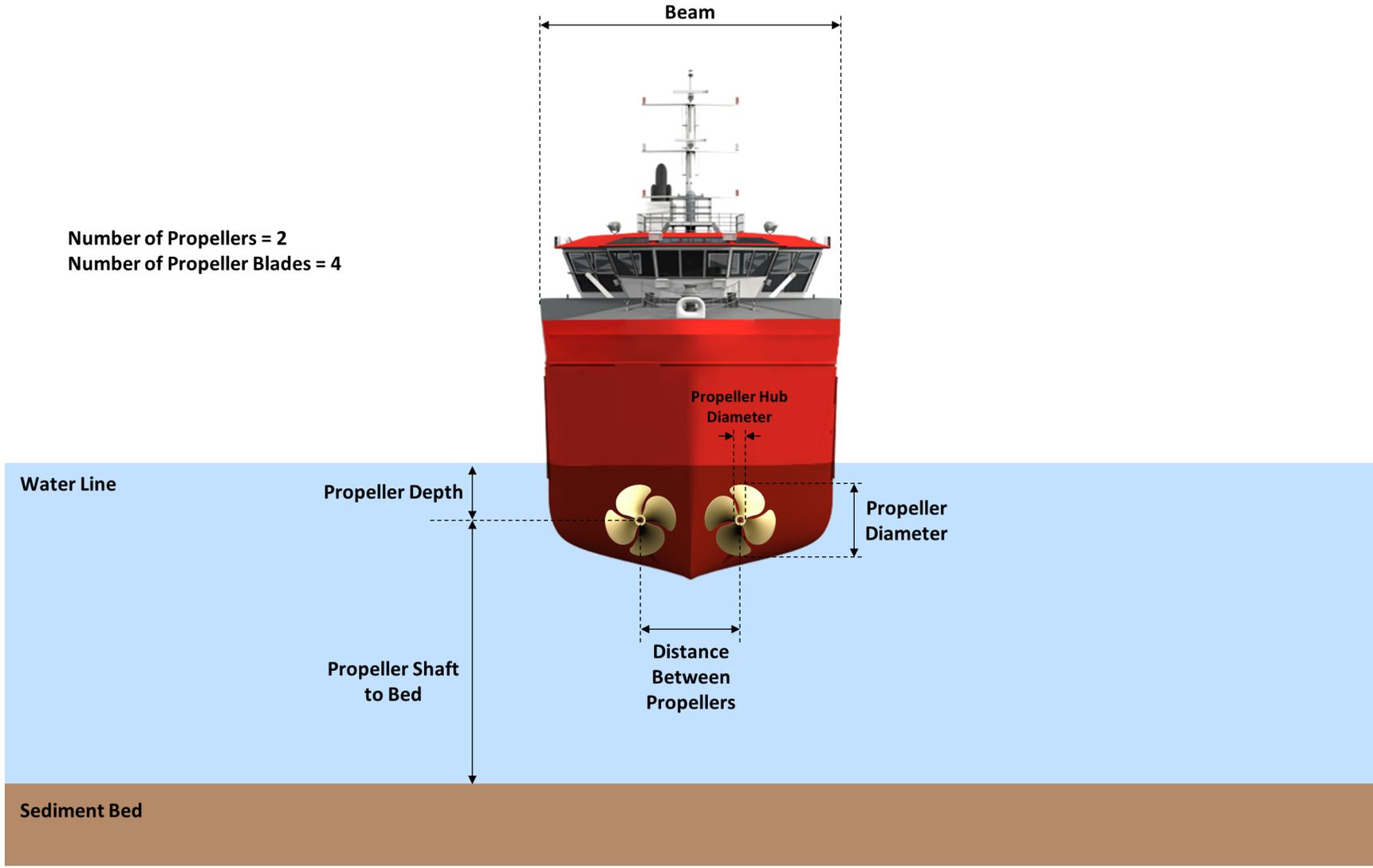
Figure 1.3: Definition for key ship properties (back view). The ship image is adapted from Damen Shipyards (2021).

Chapter 2

Theoretical Approach

Over the decades, through laboratory experiments and field measurements, numerous studies have proposed empirical relationships to represent the flow velocity field induced by the rotation of a propeller. The studies to identify the main variables influencing propeller wash calculations have been conducted based on traditional dimensional analysis techniques for physical modeling. The advent of laser-based technologies for measurements has improved the data precision and has facilitated the development of various empirical relationships. These empirical studies have found that propeller wash velocity fields depend primarily on two parameters: propeller diameter and applied power to the propeller. The studies also established that propeller wash forms a symmetrical velocity distribution with respect to the propeller shaft axis.

The EFDC+ propeller wash module computes analytical propeller wash velocity profiles by adopting Hamill's approaches (Hamill, 1987; Hamill and Kee, 2016; Hamill et al., 2015) and other empirical equations (Fuehrer and Römisch, 1977; Hashmi et al., 2007; Lam et al., 2011; Maynord, 2000; Stewart, 1992; Toutant, 1982). Figure 2.1 presents a schematic diagram summarizing the adopted equations for the following three propeller wash zones: efflux zone, zone of flow establishment, and zone of established flow.

The propeller wash formation and diffusion processes both differ explicitly among these three zones. As the propeller is rotating, the maximum propeller wash velocity occurs at the face of the propeller, which is termed the efflux velocity. This velocity remains constant (i.e., does not decay) within the efflux zone, a short distance behind the propeller. All subsequent velocity values (at any location within the diffusing propeller wash) are dependent on the magnitude of this initial maximum propeller wash velocity. As the propeller wash moves beyond the efflux zone, it enters the zone of flow establishment, where the propeller wash becomes established and disperses inward and outward. Within this zone, the maximum axial velocities decrease with distance due to lateral mixing, and the lateral velocity profile forms two peaks due to the hub's influence at the propeller center. Beyond the zone of flow establishment, the propeller wash subsequently decays to merge with any background flow in the zone of established flow, and the lateral profile of the propeller wash velocities shows only one velocity peak along the rotation axis in this region. The length of each propeller wash zone can be specified relative to the propeller diameter, D_p. The following sections describe the empirical formulations for each of the three zones adopted in the EFDC+ propeller wash module.

$$13°$$

$$V_0 = 1.59 n D_p C_t^{0.5}$$

or

$$V_0 = 1.13 \frac{1}{D_0} \sqrt{\frac{T}{\rho_w}}$$

$$V_{x,r} = V_0$$

$$\frac{V_{x,max}}{V_0} = 1.51 - 0.175 \frac{x}{D_p} - 0.46 P'$$

$$R_{mo} = 0.67 (R_p - R_h)$$

$$\frac{V_{x,r}}{V_{x,max}} = \exp\left[-\frac{1}{2}\left(\frac{r - R_{mo}}{\sigma}\right)^2\right]$$

$$\frac{V_{x,max}}{V_0} = A'\left(\frac{x}{D_p}\right)^{B'}$$

$$A' = -11.4 C_t + 6.65 \beta + 2.16 P'$$

$$B' = -C_t^{-0.216} \times \beta^{1.024} \times P'^{-1.0}$$

$$\frac{V_{x,r}}{V_{x,max}} = \exp\left[-22.2 \left(\frac{r}{x}\right)^2\right]$$

X : Longitudinal distance from the propeller (m)

D_p : Propeller diameter (m)

Efflux Zone	**Zone of Flow Establishment**	**Zone of Established Flow**
$0 < X/D_p < 0.35$	$0.35 < X/D_p < 3.25$	$3.25 < X/D_p < 50$
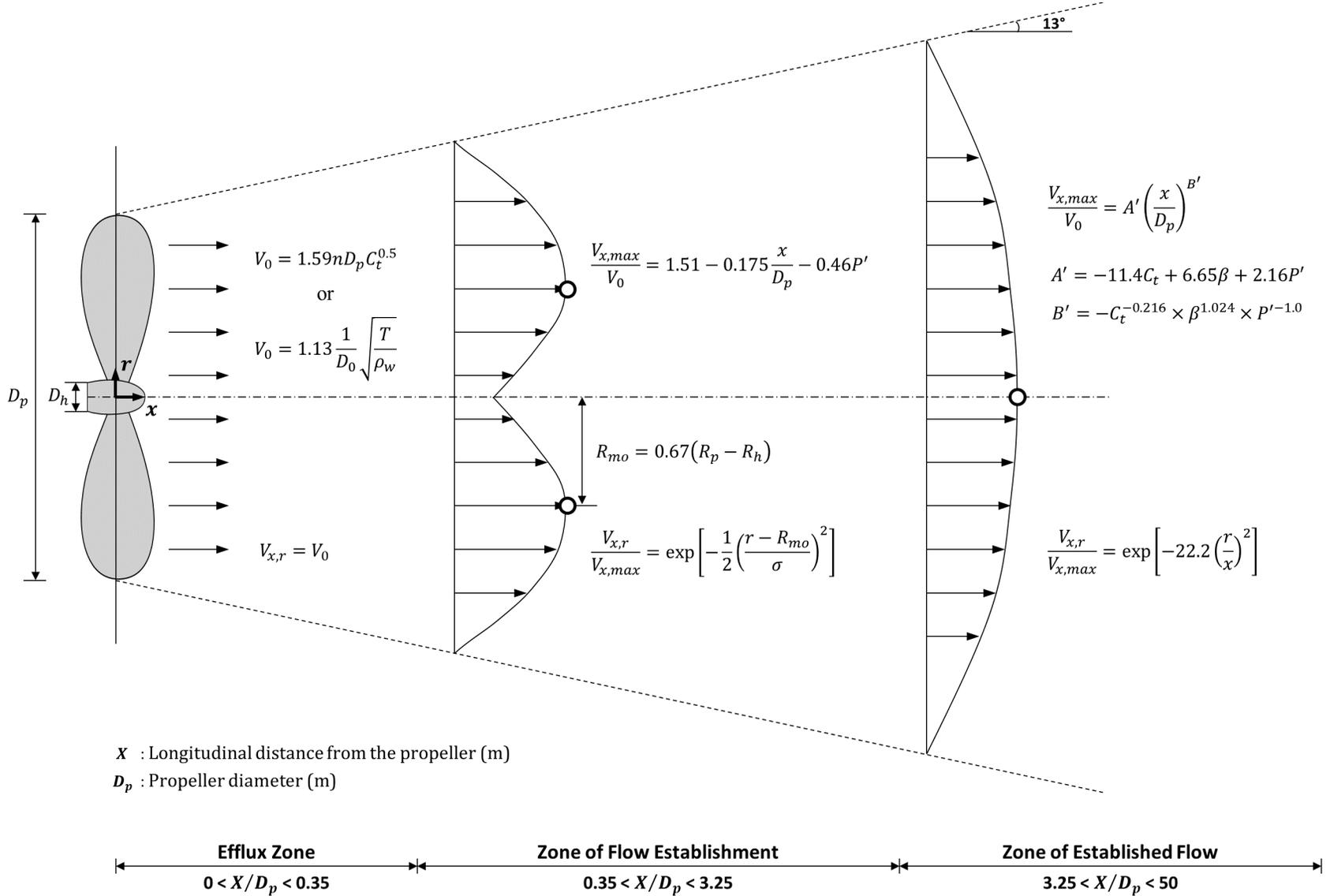
Figure 2.1: Adopted formulations for the three propeller wash zones in EFDC+ propeller wash module.

2.1. Efflux Zone

The maximum velocity at the face of the propeller is termed the efflux velocity, V_0 (Fuehrer and Römisch, 1977). Hamill (1987) suggested that there is no decay of the efflux velocity (i.e., it remains constant) within a short distance of approximately $x/D_p = 0.35$ behind the propeller (the efflux zone). Additionally, the flume experiments reported by Hamill and Kee (2016) suggested that the efflux velocity is distributed approximately uniformly along the efflux plane.

Therefore, for the analytical velocity profile, EFDC+ applies the efflux velocity V_0, which is laterally uniform with no decay within the efflux zone ($x/D_p < 0.35$), as shown in Figure 2.1. The following describes how the EFDC+ propeller wash module calculates the magnitude of the efflux velocity using either an applied propeller rotational speed or an applied ship engine power.

When a propeller rotational speed is applied, the propeller efflux velocity V_0 is computed as suggested by Fuehrer and Römisch (1977):

$$V_0 = 1.59 \times n \times D_p \times C_t^{0.5} \tag{2.1}$$

where,

V_0 : propeller efflux velocity (m/s)

n : propeller rotational speed (revolutions per second, rps)

D_p : propeller diameter (m)

C_t : propeller thrust coefficient (dimensionless)

Fuehrer and Römisch (1977) derived the above equation from axial momentum theory, and this approach has been widely accepted to predict the propeller efflux velocity (Jiang et al., 2019). In this equation, the propeller's rotational speed, diameter, and thrust coefficient are user-defined model input parameters (see Chapter 4).

When a ship engine power is applied, the propeller efflux velocity V_0 is determined in relationship with the propeller thrust T (or effective push EP). Given the applied engine power, the effective push EP (in pounds-force, lbf) is calculated using Toutant equations (1982):

$$EP = \begin{cases} 23.57P^{0.974} - 2.3V_w^2 P^{0.5} & \text{for non-ducted propeller} \\ \\ 31.82P^{0.974} - 5.4V_w^2 P^{0.5} & \text{for ducted propeller} \end{cases} \tag{2.2}$$

where,

$$V_w = |V_a - V_g| \tag{2.3}$$

where,

EP : effective push equivalent to thrust (lbf)

P : applied engine power (horsepower, hp)

V_a : ambient current velocity (mph), which is close to zero in tidal environments

V_g : ship speed relative to ground (mph)

The effective push EP in pounds-force is then converted to the thrust T in newtons as:

$$T(\mathrm{N}) = 4.45 \times EP(\mathrm{lbf}) \tag{2.4}$$

After that, the propeller efflux velocity V_0 is computed as a function of the thrust T and contracted propeller wash diameter D_0 (Maynord, 2000) as:

$$V_0 = 1.13 \times \frac{1}{D_0} \times \sqrt{\frac{T}{\rho_w}} \tag{2.5}$$

where,

$$D_0 = \begin{cases} 0.71 \times D_p & \text{for non-ducted propeller} \\\\ D_p & \text{for ducted propeller} \end{cases} \tag{2.6}$$

where,

T : thrust (N)

D_0 : contracted propeller wash diameter (m)

ρ_w : water density (kg/m^3)

2.2. Zone of Flow Establishment

Beyond the efflux zone, the propeller wash forms the zone of flow establishment. In this region, the maximum axial velocities decrease with distance from the propeller due to lateral mixing Hamill (1987). Due to the hub's influence at the center of the propeller, the propeller wash has a low-velocity core along the axis of rotation within the zone of flow establishment. Consequently, the lateral velocity profiles within the zone of flow establishment form two peaks, as shown in Figure 2.1. The fluid is mixing with the surrounding water both inwardly and outwardly along the axis of rotation. The hub's influence then disappears gradually along the longitudinal axis due to the penetration of high-velocity fluid into the low-velocity central core.

Fuehrer and Römisch (1977) and Blaauw and van de Kaa (1978) found the end of the zone of flow establishment occurred at a relative distance of $x/D_p = 2.6$ from the propeller face. Verhey

et al. (1987) suggested the zone length was $x/D_p = 2.77$, while Stewart (1992) proposed the zone extended to approximately $x/D_p = 3.25$ from the propeller face. EFDC+ allows modelers to determine the length for the zone of flow establishment as a model input parameter; the value of $x/D_p = 3.25$ (Stewart, 1992) is recommended per Hamill and Kee (2016).

Once outside of the efflux zone, as per Hamill and Kee (2016), the EFDC+ velocity profile applies the maximum axial velocity ($V_{x,max}$) decreasing linearly with distance and computes its magnitude dependent on the initial efflux velocity magnitude V_0 as:

$$\frac{V_{x,max}}{V_0} = 1.51 - 0.175\left(\frac{x}{D_p}\right) - 0.46P' \tag{2.7}$$

where,

$V_{x,max}$: maximum velocity at an axial distance x (m/s)

x : axial distance from the propeller face (m)

P' : propeller pitch to diameter ratio (dimensionless)

The lateral distribution of the velocity in the zone of flow establishment is then computed as suggested in Hamill and Kee (2016):

$$\frac{V_{x,r}}{V_{x,max}} = \exp\left[-\frac{1}{2}\left(\frac{r - R_{mo}}{\sigma}\right)^2\right] \tag{2.8}$$

where,

$$\sigma = \begin{cases} 0.5R_{mo} & \text{for } x/D_p < 0.5 \\ \\ 0.5R_{mo} + 0.075\,(x + 0.5D_p) & \text{for } x/D_p \geq 0.5 \end{cases} \tag{2.9}$$

where

$$R_{mo} = 0.67\,(R_p - R_h) \tag{2.10}$$

where,

$V_{x,r}$: velocity at an axial distance x and at a radial distance r (m/s)

r : radial distance from the propeller shaft axis (m)

R_{mo} : radial distance of maximum velocity from propeller shaft axis (m)

R_p : radius of propeller (m)

R_h : radius of propeller hub (m)

2.3. Zone of Established Flow

At a certain distance downstream, the flow will only be mixing outwardly; this is referred to as the zone of established flow. In this region, there is only one maximum velocity peak, which is located at the axis of rotation. Through direct experimental measurements and based on propeller blade characteristics, Hamill (1987) proposed the following empirical equation for the decay of the maximum axial velocity in the zone of established flow:

$$\frac{V_{x,max}}{V_0} = A' \left(\frac{x}{D_p} \right)^{B'} \tag{2.11}$$

$$A' = -11.4C_t + 6.65\beta + 2.16P' \tag{2.12}$$

$$B' = -C_t^{-0.216} \times \beta^{1.024} \times P'^{-1.87} \tag{2.13}$$

where,

β : propeller blade area ratio, usually referred to as disk area coefficient (dimensionless)

The lateral distribution of the velocity profile in the zone of established flow is then computed according to Fuehrer and Römisch (1977), per the recommendation of Hamill and Kee (2016):

$$\frac{V_{x,r}}{V_{x,max}} = \exp \left[-22.2 \left(\frac{r}{x} \right)^2 \right] \tag{2.14}$$

2.4. Computation of Velocity at Water-Sediment Interface

The propeller wash velocity at the water-sediment interface for a specific location is then calculated based on Equations 2.8 and 2.14 by specifying the longitudinal distance x and radial distance r from the propeller as:

$$x = X_p \tag{2.15}$$

$$r = \sqrt{Y_P^2 + H_P^2} \tag{2.16}$$

where,

X_p : longitudinal distance from the propeller (m)

Y_P : lateral distance from the propeller shaft axis (m)

H_p : vertical distance from the propeller shaft axis to sediment bed (m)

Chapter 3

EFDC+ Algorithm Implementation

This chapter describes the algorithmic structure and implementation processes for EFDC+ propeller wash module computation. Overall, EFDC+ implements the propeller wash computation based on an independent sub-grid for each ship. It can simulate multiple ships with a single model and specify the ship paths by utilizing ship tracking data (derived from AIS or user-defined tracking data). EFDC+ then dynamically links the propeller wash sub-grids and model grid cells to compute hydrodynamic and sediment transport processes for every sediment transport time step.

Figure 3.1 shows the flow chart for the EFDC+ propeller wash implementation procedures. The white-filled boxes indicate the general EFDC+ computation steps based on model grid cells, whereas the blue-filled boxes indicate the propeller wash module processes. The following provides the conceptual and mathematical details for each computation step, presenting the related schematic diagrams sequentially.

EFDC+ Model

EFDC+ Propeller Wash Module

Step 1
Compute EFDC+ Hydrodynamic Flow Field

Step 2
Specify Ship Position

Step 3
Generate Sub-grid Points

Step 4
Determine Bottom Elevation

Step 5
Compute Propeller Wash Velocity at Bottom

Step 6
Combine Propeller Wash and Ambient Velocities

Step 7
Compute Shear Stress at Bottom

Step 8
Compute Erosion Rate at Bottom

Step 9
Calculate Erosion Mass for Sub-grid Areas

Step 10
Aggregate Sub-grid Erosion Mass to EFDC+ Sediment Transport Model Grid

Step 11
Compute EFDC+ Sediment Transport Process

SEDSTEP = SEDSTEP + 1

Step 12
(Optional)
Add Propeller Momentum to EFDC+ Hydrodynamic Flow Field

Figure 3.1: Flow chart of the EFDC+ propeller wash module computation process.

Step 1. Compute EFDC+ Hydrodynamic Flow Field

When a simulation starts, EFDC+ computes a 3D hydrodynamic flow field at the general model grid cell resolution. Figure 3.2 displays an example of a two-dimensional (2D) plan view for model grid cells and depth-averaged ambient current velocity vectors simulated at a time step.

Step 2. Specify Ship Position

Propeller wash module computation starts with specifying the location, heading, speed, and applied power of the ships to be considered. For each ship, the EFDC+ propeller wash module establishes this information by interpolating ship tracking data, which are derived from AIS or manually defined by the modeler (see details in Section 4.4). Figure 3.2 shows a ship heading west within a model grid cell, along with the ship path.
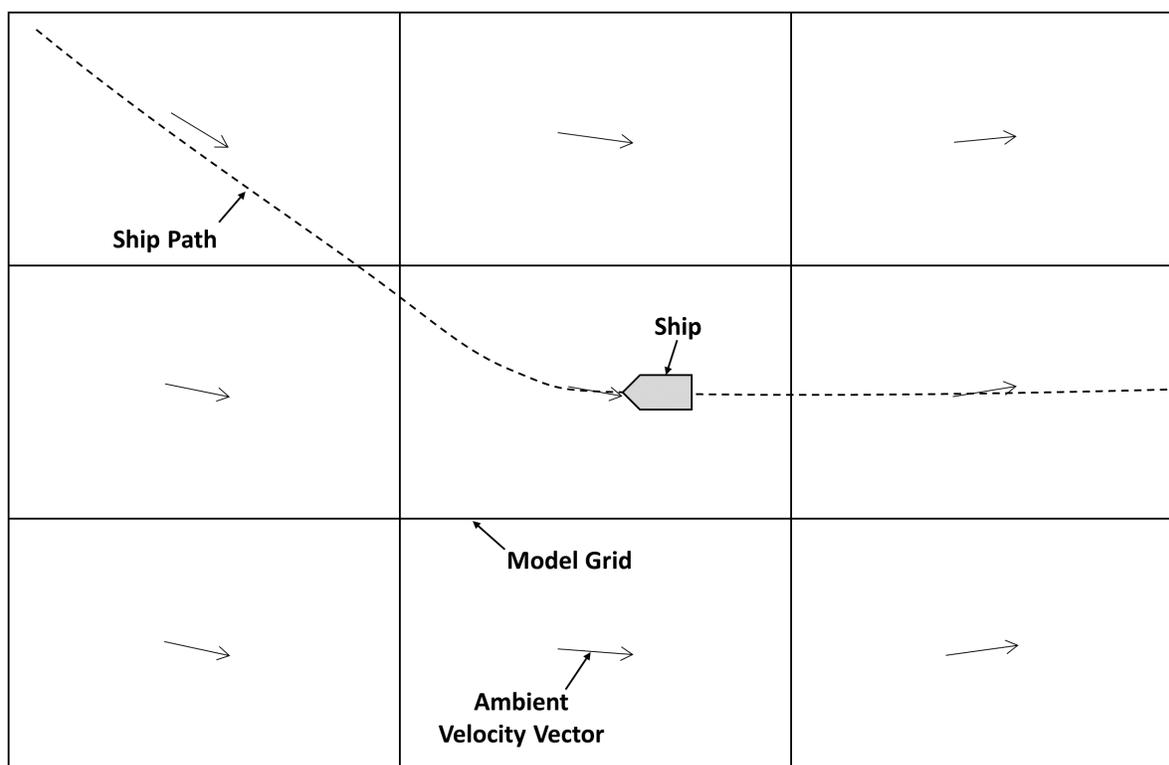
Figure 3.2: Hydrodynamic velocity field for EFDC+ model grid cells and specification of ship position based on a ship path (plan view).

Step 3. Generate Sub-grid Points

After specifying the ship positions, the EFDC+ propeller wash module generates an independent 2D sub-grid behind each ship, as shown in Figure 3.3. The sub-grid points are used for the propeller wash computation for each ship, as described in the following steps. The modeler can define the sub-grid dimensions to be a function of the propeller diameters (see details in Section 4.2).

Step 4. Determine Bottom Elevation

The bottom elevations of the sub-grid points are determined based on the bottom elevation of the model grid cells. For each sub-grid point, the EFDC+ propeller wash module uses an inverse distance squared scheme to interpolate the bottom elevation of the center of each surrounding model grid cell. Figure 3.3 presents an example of resultant sub-grid bottom elevations.
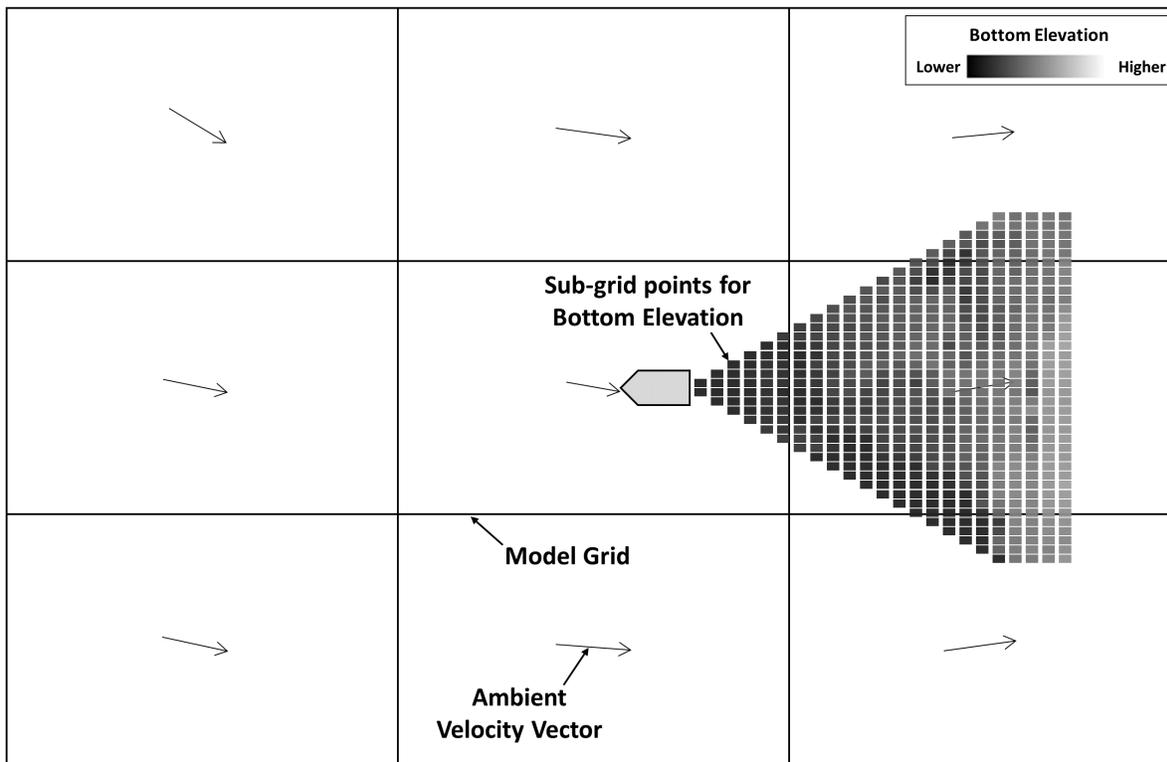
Figure 3.3: Generation of sub-grid mesh behind ship and determination of bottom elevation for each sub-grid point (plan view).

Step 5. Compute Propeller Wash Velocity at the Bottom

Given the bottom elevation, the EFDC+ propeller wash module computes the propeller wash velocities at the bottom (water-sediment interface) for each sub-grid point using the approach described in Chapter 2. Figure 3.4 presents a vertical side view of conceptual diagrams summarizing the velocity formulations for the three propeller wash zones and indicating sub-grid points for velocity computation at the water-sediment bed interface.

For ships with multiple propellers, the EFDC+ propeller wash module computes the propeller wash velocity field for each propeller separately, then superposes them according to the distance between propellers. In this case, a ship with multiple propellers still has a single sub-grid mesh, indicating the velocity caused by multiple propellers. Figure 3.5 illustrates the superposition process for a two-propeller ship from a vertical back view.
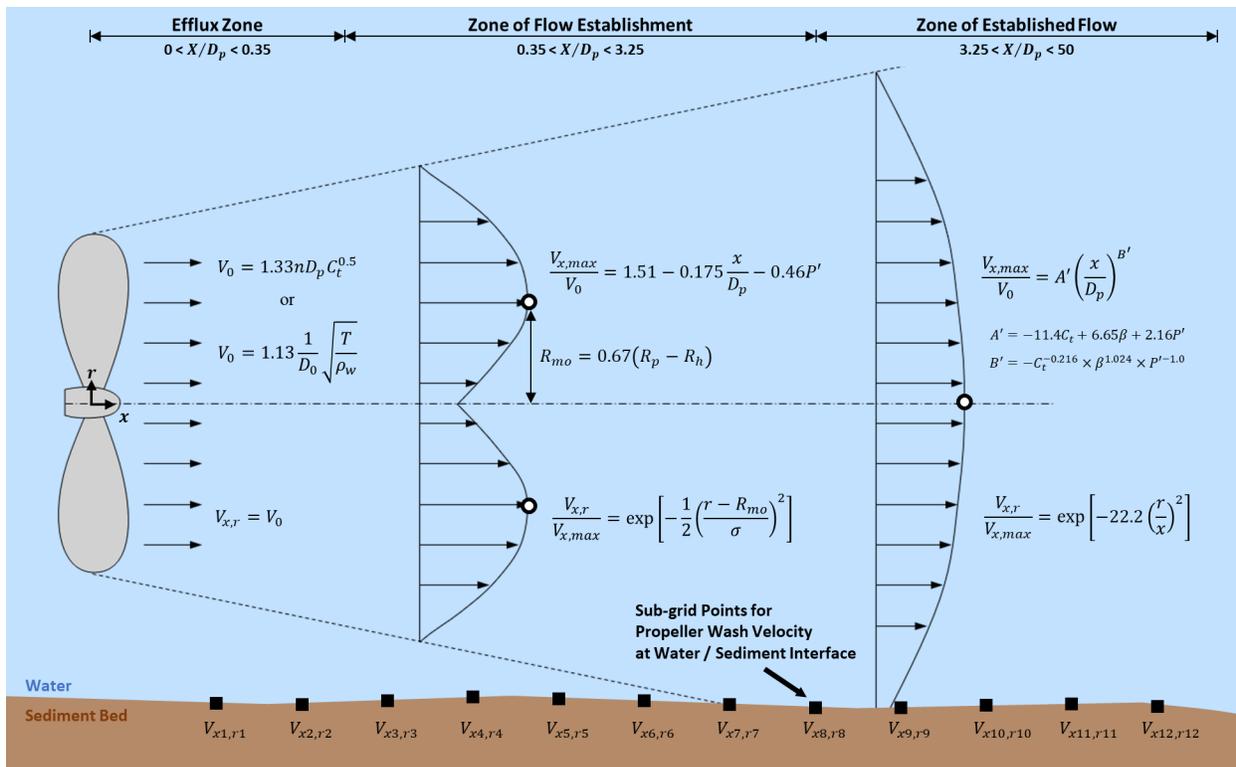
Figure 3.4: Sub-grid points for velocity computation at water-sediment bed interface (side view).
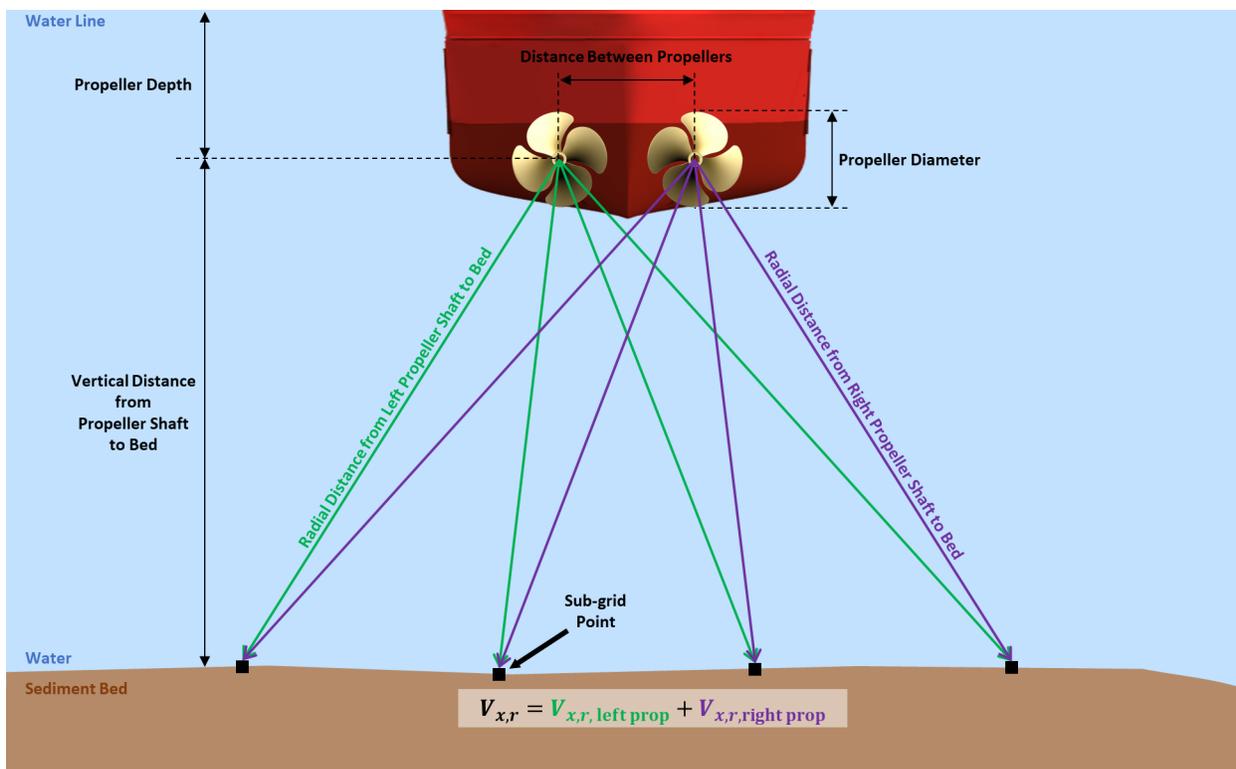
Figure 3.5: Superposition of propeller wash velocities for a two-propeller ship (back view).

Step 6. Combine Propeller Wash and Ambient Velocities

Figure 3.6 displays the ambient current velocity vectors for model grid cells computed from Step 1 and the propeller wash velocities for sub-grid points (red for higher values and blue for lower values) computed from Step 5. At this step, the EFDC+ propeller wash module calculates a near-bed velocity for each sub-grid point, combining the ambient current and propeller wash velocities.
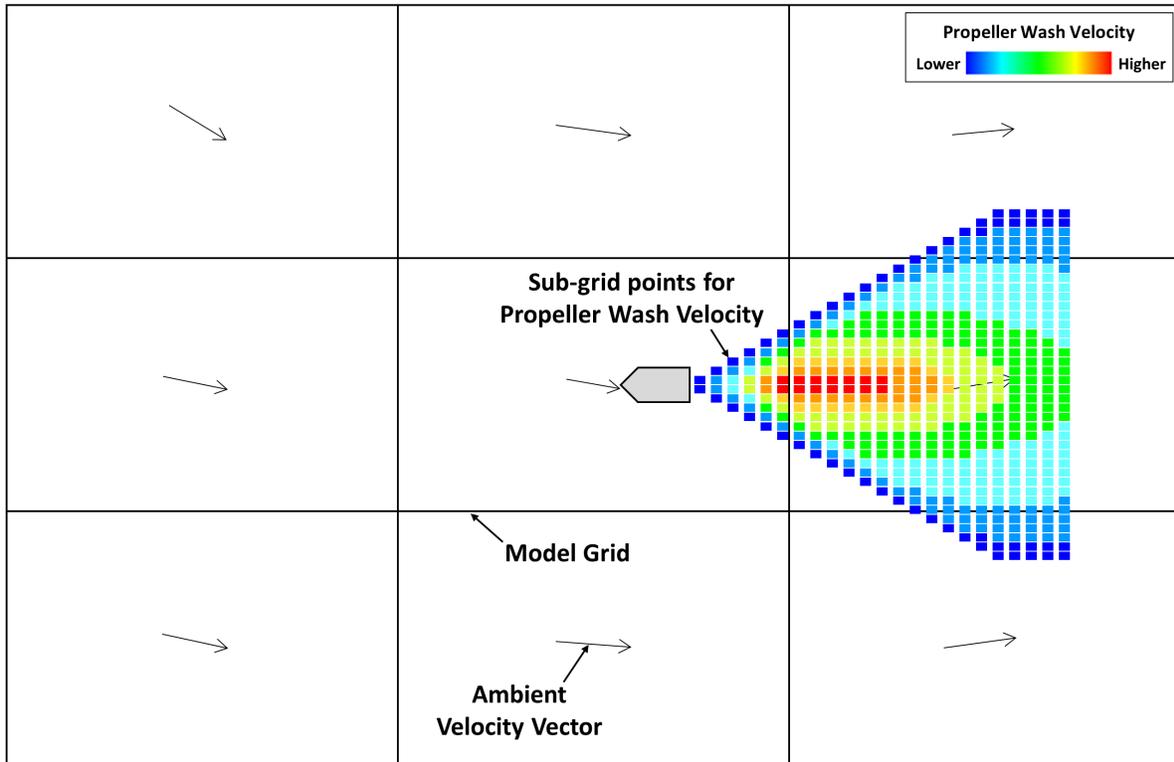
Figure 3.6: Propeller wash velocities at sub-grid points and ambient current velocity vectors for model grid cells (plan view).

Step 7. Compute Shear Stress at the Bottom

Given the near-bed velocity, the EFDC+ propeller wash module computes bottom shear stress τ_p (N/m^2) for each sub-grid point using the Maynord (2000) approach as follows:

$$\tau_p = 0.5 \times \rho_w \times C_f \times (V_{bed})^2 \tag{3.1}$$

$$C_f = 0.01 \times \frac{D_p}{H_p} \tag{3.2}$$

where,

ρ_w : water density (kg/m^3)

C_f : friction coefficient (dimensionless)

V_{bed} : near-bed velocity (m/s)

D_p : propeller diameter (m)

H_p : distance between propeller shaft and sediment bed (m)

Step 8. Compute Erosion Rate at the Bottom

Given the bottom shear stress, the EFDC+ propeller wash module computes an erosion rate E_{rate} for each sub-grid point. The propeller wash erosion rate is calculated using either the Original EFDC Sediment Transport approach (in g/m^2/s) (van Rijn, 1984a,b,c) or the SEDZLJ Sediment Transport approach (in g/cm^2/s) (Jones and Lick, 2001) in accordance with the approach used for the general EFDC+ sediment transport processes at the model grid cells (in Step 11). Additionally, this step computes the erosion rates for bedload and suspended load separately with respect to the applied bottom shear stress, critical shear stress of bed materials, and particle settling velocities. EFDC+ Theory Document Chapter 6 (DSI, 2020) provides detailed theories and mathematical descriptions for the Original EFDC and SEDZLJ Sediment Transport approaches. In Figure 3.7, the sub-grid points with a color ramp show an example of the resultant bottom shear stress or erosion rate, where red indicates higher value and blue indicates lower value.
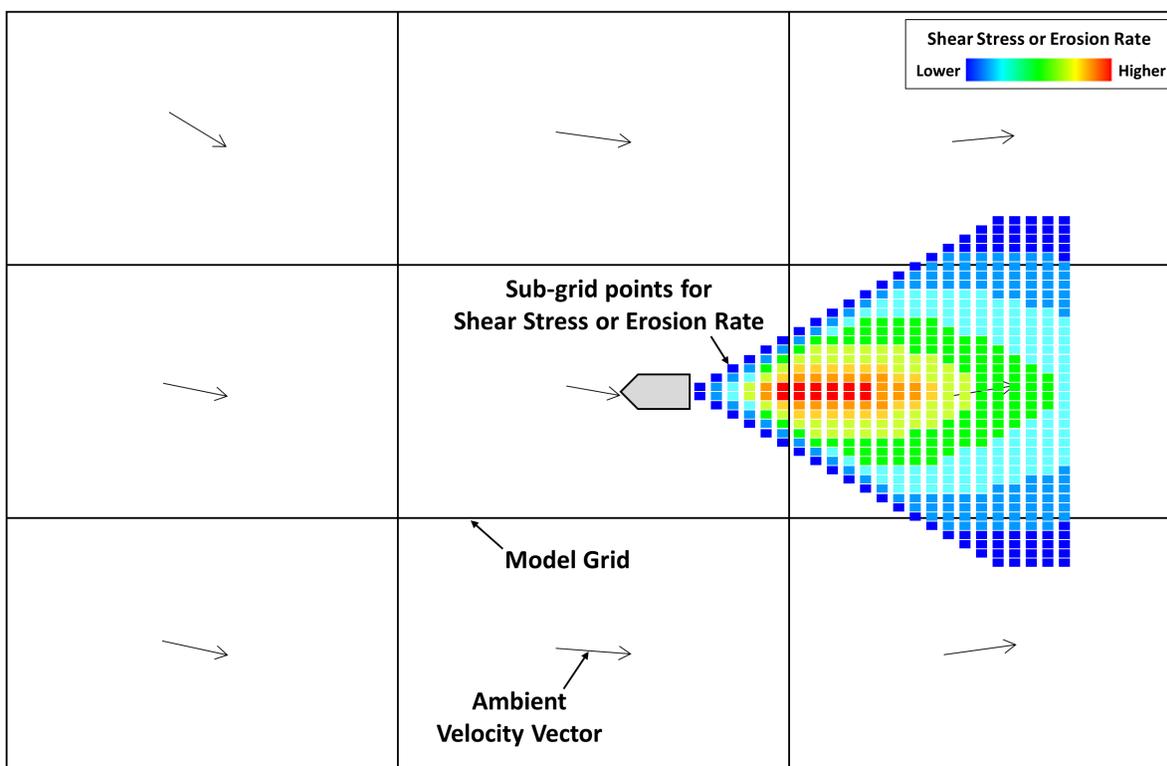
Figure 3.7: Shear stress or erosion rate induced by propeller wash at sub-grid points (plan view).

Step 9. Calculate Erosion Mass for Sub-grid Areas

Figure 3.8 displays sub-grid points and sub-grid areas, indicating the associated erosion quantities with colors. The EFDC+ propeller wash module applies an assumption that the erosion rate at the sub-grid point represents the erosion amount within the surrounding sub-grid area. It then calculates the erosion mass E_m (g) for each sub-grid area during a sediment time step using the erosion rate (g/m^2/s for the Original EFDC Sediment Transport approach or g/cm^2/s for the SEDZLJ approach) of each sub-grid point as follows.

$$E_m = E_{rate} \times A_{sub} \times T_{sed} \tag{3.3}$$

where,

E_m : erosion mass at a sub-grid area (g)

E_{rate} : erosion rate at a sub-grid point (g/m^2/s or g/cm^2/s)

A_{sub} : area of a sub-grid area (m^2 or cm^2)

T_{sed} : sediment time step (s)
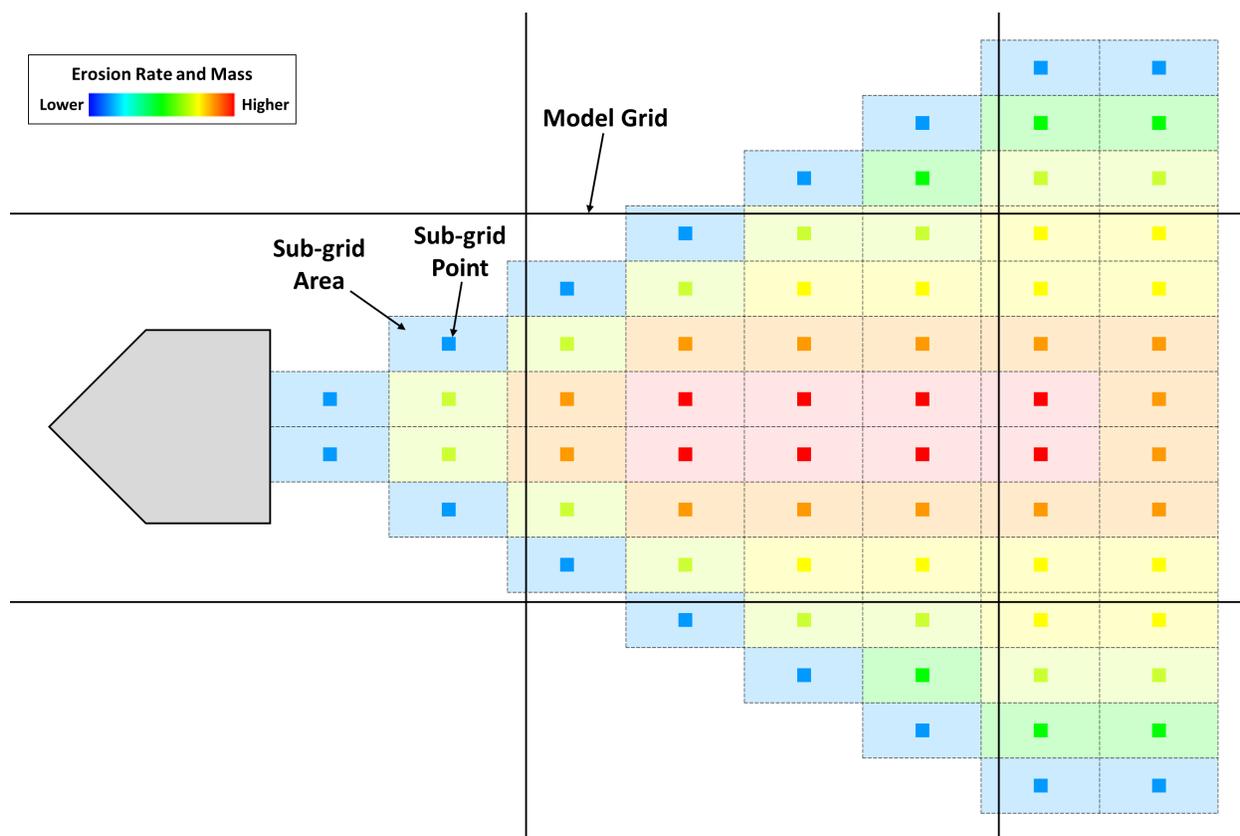
Figure 3.8: Sub-grid points, sub-grid area, and model grid cells for propeller wash-induced erosion mass calculation (plan view).

Step 10. Aggregate Sub-grid Erosion Mass to EFDC+ Model Grid

Once the erosion mass (g) is calculated for each sub-grid area, the EFDC+ propeller wash module computes a total erosion mass (g) at each model grid cell by aggregating the sub-grid area erosion masses within the corresponding model grid cell. Figure 3.8 shows the sub-grid points, sub-grid areas, and model grid cells that are related to the total erosion mass calculation.

Step 11. Compute EFDC+ Sediment Transport Process

EFDC+ then simulates the sediment transport processes for the model grid cells via a user-defined approach: either Original EFDC Sediment Transport or SEDZLJ Sediment Transport. Figure 3.9 conceptually illustrates the general sediment transport processes that EFDC+ simulates for the water column and the sediment bed. The sediments eroded from the bed (computed from Step 10) are transported as bedload and suspended load, as specified from Step 8. For the bedload computation, the eroded sediments are transported to the top sediment bed layer of the adjacent model cell downstream, which represents the process of sediments saltating (i.e., rolling and bouncing) along the sediment bed surface. For the suspended load computation, the eroded sediments are distributed into the water column (i.e., resuspension), and subsequent transport processes (i.e., advection, mixing, settling, and deposition) of the resuspended sediments are then simulated in response to the hydrodynamic flow field. Theories and mathematical descriptions for the sediment transport processes are described in detail in EFDC+ Theory Document Chapter 6 (DSI, 2020).
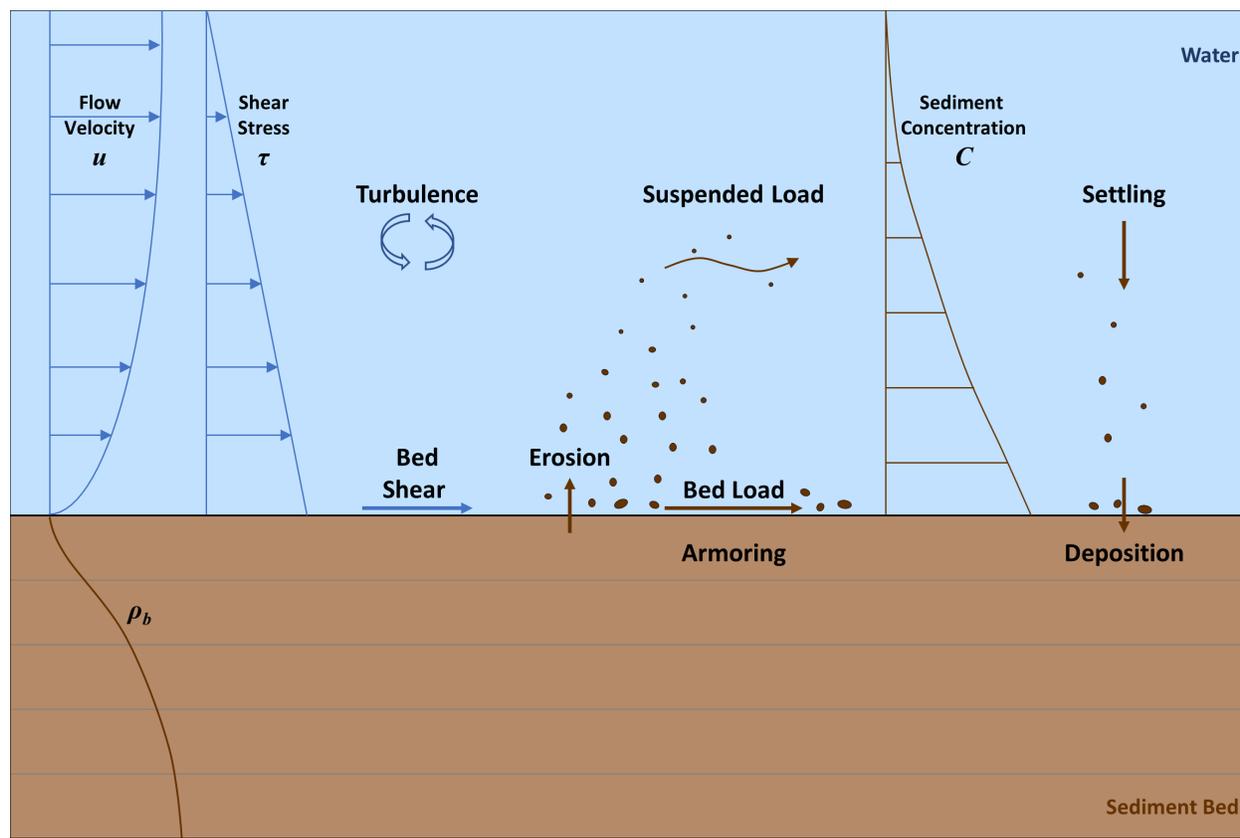
Figure 3.9: Conceptual diagram for EFDC+ sediment transport processes (side view).

Step 12. Add Propeller Momentum to EFDC+ Hydrodynamic Flow Field (Optional)

The EFDC+ propeller wash module has an option to add the momentum associated with the pro-
peller efflux velocity V_0 (calculated from Equation 2.1 or 2.5) to a 3D hydrodynamic flow field
as a source term (see EFDC+ Theory Document Chapter 2 [DSI, 2020] for the momentum equa-
tions in detail). If this option is activated, the EFDC+ hydrodynamic model includes the propeller
wash momentum effects when it computes the 3D hydrodynamic flow field for the next time step.
The resulting flow velocities then impact the movement of the resuspended sediments in the water
layers of the EFDC+ model grid. Section 4.1 describes the input model parameter requirements
to activate this option, and Section 6.4 demonstrates the propeller wash momentum effects on the
flow velocity field and sediment transport processes.

Figure 3.10(a) shows a 2D conceptual diagram for the velocity vector components of a ship pass-
ing through an EFDC+ model grid cell. Based on the angle between the ship's heading and the
EFDC+ model grid rotation, the EFDC+ propeller wash module vectorially splits the propeller
efflux velocity V_0 into the computational grid space (in i and j directions) as:

$$V_i = V_0 \times \cos(\theta_3 - \theta_1) \tag{3.4}$$

$$V_j = V_0 \times \sin(\theta_3 - \theta_1) \tag{3.5}$$

$$\theta_3 = \theta_2 - \frac{\pi}{2} \tag{3.6}$$

where,

V_0 : propeller efflux velocity from the propeller plane (m/s)

V_i : grid-oriented efflux velocity component in the i direction (m/s)

V_j : grid-oriented efflux velocity component in the j direction (m/s)

θ_1 : EFDC+ model grid cell rotation (radian)

θ_2 : ship heading in compass orientation (radian)

θ_3 : propeller wash efflux angle (radian)

Given the velocity components V_i and V_j, the EFDC+ propeller wash module computes the rate
of momentum change (i.e., mass $\times$ velocity / time) due to propeller wash for each direction as
follows:

$$M_{pi} = |V_i \times A| \times V_i \times \rho_w \tag{3.7}$$

$$M_{pj} = |V_j \times A| \times V_j \times \rho_w \tag{3.8}$$

where,

M_{Pi} : rate of momentum change due to propeller wash in the i direction (kg·m/s^2)

M_{Pj} : rate of momentum change due to propeller wash in the j direction (kg·m/s^2)

A : area of propeller wash face in the efflux zone (m^2)

ρ_w : water density (kg/m^3)

The EFDC+ propeller wash module then incorporates the resultant momentum change rates M_{Pi} and M_{Pj} into the momentum equations of EFDC+ hydrodynamic model computations as a source term (see EFDC+ Theory Document Chapter 2 [DSI, 2020]). The EFDC+ propeller wash module also applies a factor to adjust the propeller wash-induced momentum change rates to account for losses and turbulence that are not directly simulated. This factor is a user-defined input parameter of the EFDC+ propeller wash module, and the default factor is 0.75 (see Section 4.2).

Vertically, the EFDC+ propeller wash module distributes the propeller wash-induced momentum effects proportionately across the EFDC+ model grid water layers that the propeller intersects. The vertical splitting process for the momentum change rates M_{Pi} and M_{Pj} is implemented with relative to the ship draft, propeller diameter, water depth, and the number of the model grid water layers where the propeller is located. Figure 3.10(b) shows an example of vertical fractions (%) for the propeller wash-induced momentum change rates over the EFDC+ model grid water layers.
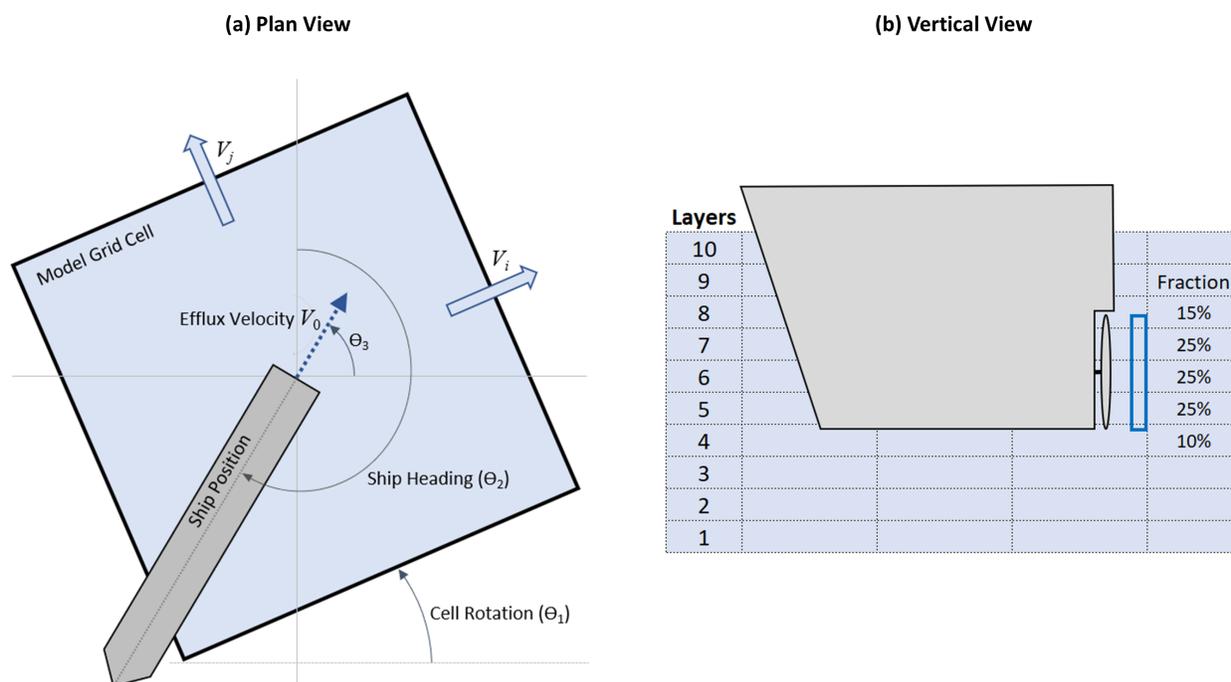
Figure 3.10: Diagrams for propeller wash-induced momentum (a) coupling with a EFDC+ model grid cell and (b) splitting over vertical water layers.

Repeat Propeller Wash Computation Every EFDC+ Sediment Transport Time Step

EFDC+ repeats the above propeller wash module computation processes (Steps 1 to 12) for every sediment transport time step while the ships are located within the model domain. Figures 3.11 to 3.13 provide an example of how a ship with a sub-grid mesh is moving along a ship path and ambient currents vary sequentially during a simulation.

Additionally, EFDC+ can implement direct geomorphic feedback between hydrodynamic and sediment transport processes during a simulation. Specifically, the bed elevation changes predicted by the propeller wash-induced sediment transport computation update the bathymetry (i.e., bottom elevations) used in the hydrodynamic computation for the next time step. This modeling capability of EFDC+ would lead to a more reasonable representation of flow field and sediment transport behaviors due to ship traffic.
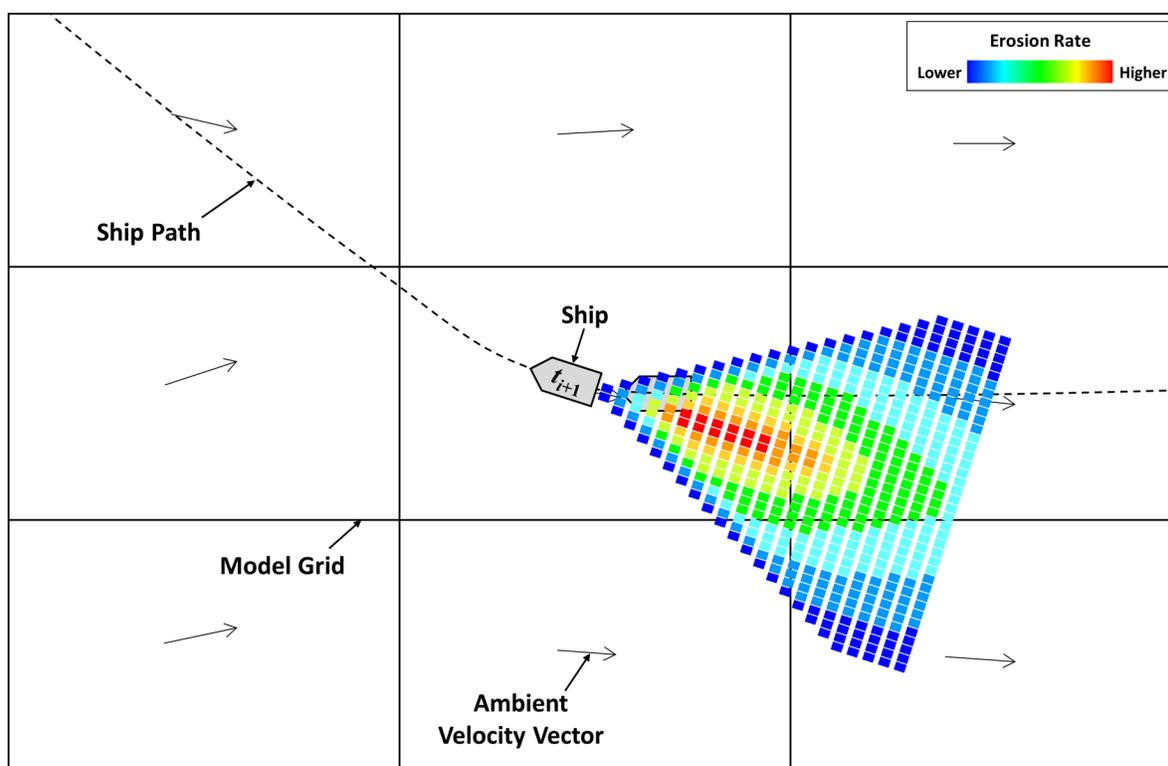
Figure 3.11: Example of a moving ship with a sub-grid mesh at time step t_{i+1} (plan view).
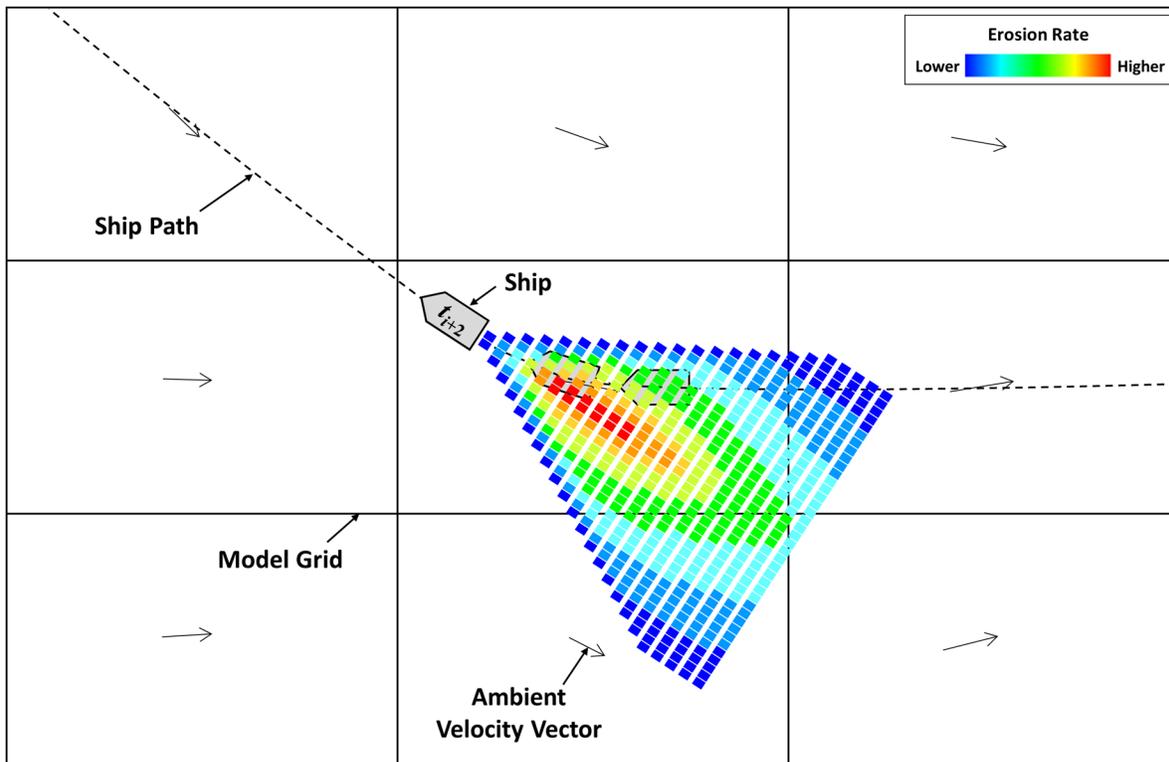
Figure 3.12: Example of a moving ship with a sub-grid mesh at time step t_{i+2} (plan view).
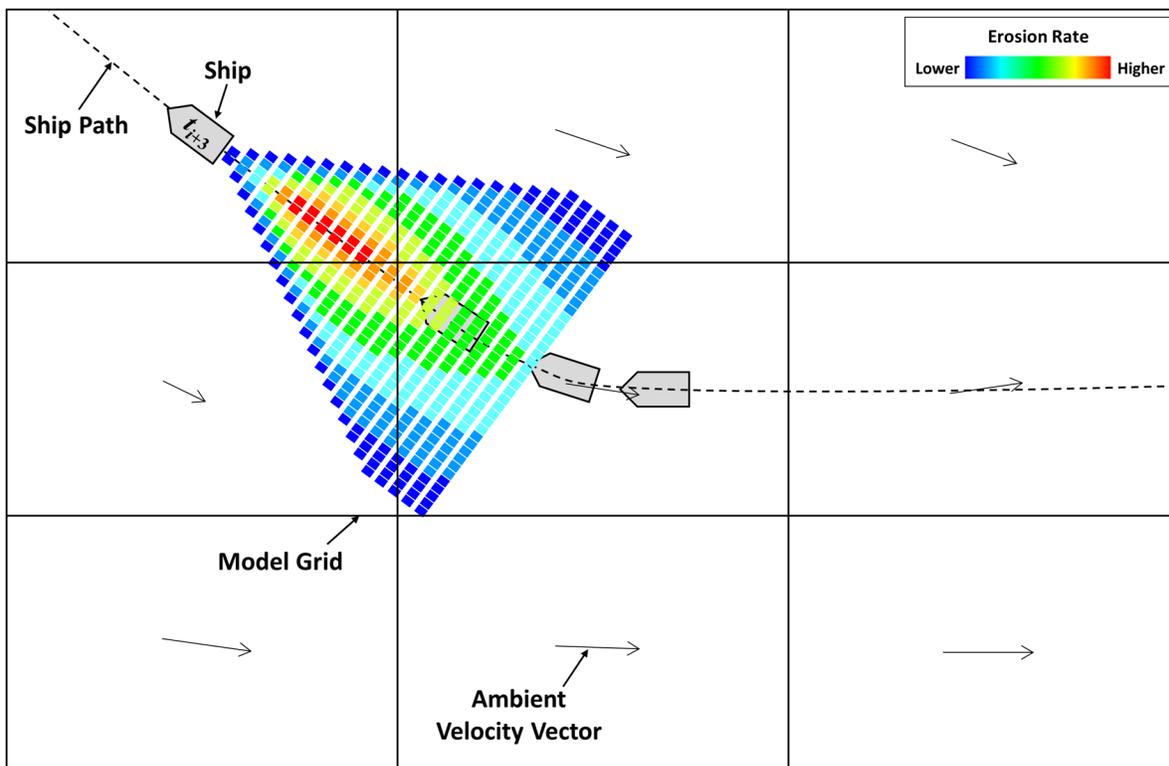
Figure 3.13: Example of a moving ship with a sub-grid mesh at time step t_{i+3} (plan view).

Chapter 4

EFDC+ Input Requirements

The EFDC+ propeller module performs a propeller wash simulation by reading four input files, which contain module control parameters, sub-grid configuration, ship and propeller properties, and ship tracking data. First, this chapter provides the details of the model parameters and input data necessary for the four input files. Then, we suggest general guidelines for ship and propeller specifications, which can be used as the model inputs when the required information is missing or unavailable.

4.1. efdc.inp

"efdc.inp" is the master input file of EFDC+. It is an ASCII-formatted file containing computational options and data setting parameters, structured into card groups with respect to input objectives. In card group 14, the parameter "ISPROPWASH" offers options for whether the propeller wash module is activated for a simulation, as described in Table 4.1. When "ISPROPWASH" = 0, the propeller wash module is deactivated, so the simulation does not implement the propeller wash computation at all. When "ISPROPWASH" = 1, the propeller wash module is activated, so the simulation computes the propeller wash-induced sediment transport processes following Steps 1 to 11 in Chapter 3, but no impact on the flow field (i.e., propeller efflux momentum is not incorporated). When "ISPROPWASH" = 2, the simulation incorporates the propeller momentum effects into the hydrodynamic flow field computation (Step 12 in Chapter 3) so that the resulting flow velocities impact the movement of resuspended sediments in the water column.

Table 4.1: Propeller wash module control fields in efdc.inp file.

Card	Field	Value	Description
C14	ISPROPWASH	0	No propeller wash
		1	Activate propeller wash computation
		2	Activate propeller wash computation with incorporating propeller efflux momentum

4.2.   propwash_config.jnp

"propwash_config.jnp" specifies the general settings for propeller wash simulation in JavaScript Object Notation (JSON) format (see details at www.json.org/json-en.html). These settings are separated into "mesh" and "parms" groups, as shown in Table 4.2.

The "mesh" group parameters are to specify the propeller wash sub-grid mesh configuration. The longitudinal and lateral dimensions of the sub-grid mesh are determined by multiplying "mesh_length" and "mesh_width" parameters by a propeller diameter D_p, respectively. For two-propeller ships, the lateral dimension of the sub-grid mesh can be determined as "mesh_width" $\times$ (D_p + distance between two propellers). The number of sub-grid points is defined by "num_axial_elems" for the longitudinal dimension and "radial_elems_per-axial" for the lateral dimension.

In the "parms" group, three distance multipliers are applied to the propeller diameter D_p to define the lengths for the efflux zone, zone of flow establishment, and zone of established flow, as described in Figure 2.1. The default values are also given in Figure 2.1, and users may adjust them regarding the several suggestions described in Chapter 2.

"efflux_mag_mult" is a multiplier factor to adjust the efflux velocity momentum M_P to account for losses and turbulence, as described in Step 12 in Chapter 3. This parameter is used only when the simulation adds the propeller efflux momentum to the hydrodynamic flow field (i.e., when ISPROPWASH = 2), with a default of 0.75.

Table 4.2: Propeller wash configuration parameters in propwash_config.jnp file.

Group	Field	Description
mesh	num_axial_elems	Number of sub-grid points in the axial direction
	num_radial_elems	Number of sub-grid points in the radial direction
	mesh_length	Multiplier for sub-grid length in the axial direction
	mesh_width	Multiplier for sub-grid length in the radial direction
parms	efflux_zone_mult	Distance multiplier for the efflux zone
	flow_est_zone1_mult	Distance multiplier for the zone of flow establishment
	flow_est_zone2_mult	Distance multiplier for the zone of established flow
	efflux_mag_mult	Efflux velocity momentum factor (for ISPROPWASH = 2)

4.3.   propwash_ships.jnp

"propwash_ships.jnp" contains the ship characteristics and propeller specifications in JSON format. The EFDC+ propeller wash module performs the propeller wash computation for multiple ships (no limitation in numbers) in a single simulation, so this input file should include the information for all the ships being modeled. Table 4.3 lists the ship and propeller specification parameters required for each ship (refer also to Figures 1.2 and 1.3 for illustrations of these ship features). In a simulation, the EFDC+ propeller wash module identifies each ship using the parameter "mmsi", which indicates a Maritime Mobile Service Identity (MMSI) number. The parameter "mmsi" is used to link the ship characteristics in this input file to the corresponding ship tracking records in the "propwash_tracks.jnp" file (see Section 4.4).

In Table 4.3, essential parameters are marked with an asterisk. Unfortunately, public and commercial databases generally provide only basic ship data (e.g., MMSI, vessel type, length, beam, gross tonnage), which are not sufficient to specify the parameter values required for model simulations. For instance, the installed engine power (max_power or max_rps) is the most important piece of ship information for the propeller wash computation, but it is rarely available. To overcome such limitations in data availability, several approaches were devised to estimate the most important properties of ships and propellers using public and commercial databases; these approaches are described in Section 4.5.

Table 4.3: Ship and propeller specification parameters in propwash_ships.jnp file.

Field	Description
mmsi*	MMSI number
IMO	International Maritime Organization (IMO) identification number
USCG	United States Coast Guard (USCG) documentation number
name	Ship name
call_sign	Radio transmission license identifier
type	Vessel type
year_built	Year the ship was built
length*	Ship length overall: distance between bow and stern (m)
beam*	Ship width at its widest point (m)
hull_depth	Depth of the watertight body of the ship (draft + freeboard) (m)
gross_tonnage	Overall internal volume of the ship (all enclosed spaces)
net_tonnage	Molded volume of the cargo spaces (dimensionless)
max_rps*	Maximum propeller rotation speed in revolutions per second (rps)
max_power*	Maximum installed engine power in horsepower (hp)
max_draft	Maximum distance between the waterline and hull bottom (m)
min_draft	Minimum distance between the waterline and hull bottom (m)
ais_to_stern	Distance between the AIS antenna location and stern (m)
dist_from_stern	Distance between the propeller and stern (m)
dist_between_props*	Distance between propeller shafts (for multiple propellers) (m)
prop_offset	Distance from the hull bottom to the propeller shaft (m)
num_props*	Number of propellers
num_blades*	Number of propeller blades
ducted*	0 for non-ducted propeller, 1 for ducted propeller
thrust_coeff*	Propeller thrust coefficient
prop_diam*	Propeller diameter (m)
prop_hub_diam*	Propeller hub diameter (m)
blade_area_ratio*	Blade area ratio (dimensionless)
pitch_ratio*	Pitch ratio (dimensionless)
freq_out*	Frequency for propeller wash sub-grid output (in minutes)
active_flag*	0 for deactivation, 1 for activation of the ship simulation
num_fixed_cells	Number of model cells for a fixed ship simulation
fixed_cells	I and J of the model cells for the fixed ship simulation
fixed_frac	Cell fractions of propeller impacts for the fixed ship simulation

Essential model parameters

4.4.   propwash_tracks.jnp

"propwash_tracks.jnp" contains the tracking records for all the ships being simulated in JSON format. Figure 4.1 shows an example of the "propwash_tracks.jnp" file format, and Table 4.4 provides the descriptions for each field grouping with respect to hierarchical levels.

At the general level, "name" is for the title of ship tracking datasets recorded in this input file; "utm_zone" defines the Universal Transverse Mercator (UTM) coordinate zone for ship locations; and "base_date" sets the base date (Julian day time) applied to the tracking records in this file.

Under the "all_ship_tracks" field, "mmsi" is used to identify each ship being modeled and links to the ship characteristics and propeller specifications defined in the "propwash_ships.jnp" file (see Section 4.3). Each ship can have multiple tracks under the "ship_tracks" field, where a track indicates a series of continuous ship path records ("track field").

The "track" field contains a series of time records for each track. Each record specifies a set of ship data at a given time "t", including ship status "n", speed "s", course "c", heading "h", draft "d", applied engine power "p", and location "x" and "y". The "track" field also contains the parameter "o", which can specify the sub-grid computation output frequency for a certain track duration. Unless it is set to zero, this parameter will override the general sub-grid output frequency "freq_out" in "propwash_ships.jnp". Additionally, Table 4.5 provides the ship status code descriptions available for the parameter "n".

In the "track" field, the applied power "p" is defined as a fraction of either a maximum installed engine power in horsepower (hp) or a maximum propeller rotation speed in revolutions per second (rps). Modelers should use a positive value for "p" if the applied power is determined based on the maximum installed engine power (e.g., "p = 0.5" indicates that a ship is operating with 50% of the maximum engine power). In contrast, the "p" value should be negative if the applied power is specified based on the maximum propeller rotation speed (e.g., "p = -0.5" indicates that a propeller is rotating at 50% of the maximum revolution speed). The maximum installed engine power (max_power) and maximum propeller rotation speed (max_rps) are recorded in "propwash_ships.jnp" (see Section 4.3).

```
{
  "name": Propwash Example,
  "utm_zone": 10,
  "base_date": "2021-01-01 00:00:00",
  "all_ship_tracks": [
    {
      "mmsi": 366759130,
      "ship_tracks": [
        {
          "track": [
            {
              "n": 15,
              "s": 0.874555647,
              "c": 119.0,
              "h": 117.0,
              "d": 3.0,
              "o": 0.0,
              "p": 0.346,
              "t": 76.269039,
              "x": 537962.060303,
              "y": 5293592.013733
            },
            {
              "n": 15,
              "s": 1.491889,
              "c": 119.0,
              "h": 119.0,
              "d": 3.0,
              "o": 0.0,
              "p": 0.522,
              "t": 76.269144,
              "x": 537972.955284,
              "y": 5293586.149296
            },
```

Figure 4.1: Example of the propwash_tracks.jnp file format.

Table 4.4: Ship track data fields in the propwash_tracks.jnp file.

Level	Field	Description
General	name	Title of ship track datasets
	utm_zone	UTM coordinate zone for ship locations x, y
	base_date	Base date for Julian date track time t
	all_ship_tracks	Field to contain track datasets for all ships
All Ship Tracks	mmsi	MMSI number for each ship
	ship_tracks	Field to contain multiple tracks for each ship
Ship Tracks	track	Field to contain a series of time records for each track
	n	Ship Status Code (see Table 4.5)
	s	Speed (m/s)
	c	Course (degree): direction of travel through the water
	h	Heading (degree): direction the ship is pointing
	d	Draft (m): distance between the waterline and hull bottom
	o	Sub-grid output frequency (minutes)
	p	Applied power as a fraction of max_power (+) or max_rps (-)
	t	Time (Julian date)
	x	Ship location in x-coordinate (UTM-based)
	y	Ship location in y-coordinate (UTM-based)

Table 4.5: Ship status code descriptions for parameter "n".

n	Ship Status Description
0	Under way using its engine
1	Anchored
2	Not under command
3	Has restricted maneuverability
4	Ship draft is limiting its movement
5	Moored
6	Aground
7	Engaged in fishing
8	Under way sailing
9 & 10	Reserved for modifying reported status of ships carrying dangerous goods / harmful substances / marine pollutants
11	Power-driven ship towing astern
12	Power-driven ship pushing ahead/towing alongside
13	Reserved for future use
14	Any of the following are active: AIS-SART (Search and Rescue Transmitter) AIS-MOB (Man Overboard) AIS-EPIRB (Emergency Position Indicating Radio Beacon)
15	Undefined (default)

4.5. Data Input Guidelines

This section provides general guidelines for ship and propeller specifications to be used as model inputs for EFDC+ propeller wash simulations. In general, public and commercial AIS databases provide only basic information such as ship ID, vessel type, length, beam, gross tonnage, and time track records (location, speed, and heading direction). Such basic information is insufficient to specify the detailed ship characteristics and operations required for model simulations. To overcome the limitation in data availability, we first collected public and commercial data associated with ship and propeller properties from various sources, including PIANC (2015), NYSDOT (2005), MAN (2018), and TugboatInformation.com (2021). Several approaches were devised to estimate the most important properties of ships and propellers based on the basic ship information (refer to Figures 1.2 and 1.3 for illustrations of ship features). The guidelines described in this section will be beneficial to modelers when the information needed for model inputs is not available.

4.5.1 Ship Properties

4.5.1.1 Draft

A ship's draft is the distance between the waterline and the hull bottom. Modelers can specify the maximum draft as a function of a ship's length. Figure 4.2 shows the relationship between the overall length and the draft of fully loaded ships from PIANC (2015) data for different vessel types (e.g., tankers, carriers, container ships, cargo ships, passenger ships, and fishing boats). Overall, the fully loaded draft usually falls within 2.5% to 6.5% of the length. The ratio varies slightly depending on the vessel type (higher for tankers and lower for passenger ships). Therefore, modelers may choose a ratio between 2.5% and 6.5% of the ship's length when estimating the maximum draft of the ship.

Table 4.6 presents the light draft and loaded draft of self-propelled oil tankers provided by NYS-DOT (2005). Modelers may estimate the minimum draft as about 45% to 70% of the maximum draft based on this information.

4.5.1.2 Hull Depth

The parameter hull depth refers to the depth of the watertight body of a ship, which includes the draft and freeboard. Figure 4.3 shows the relationship between the hull depth and the draft of fully loaded ships from the PIANC (2015) data. Generally, the hull depth is 1.2 to 2.4 times greater than the fully loaded draft. The ratio varies depending on the vessel type (higher for cargo ships and lower for tankers). Based on this, modelers may estimate the hull depth as a function of the maximum draft according to the vessel type.
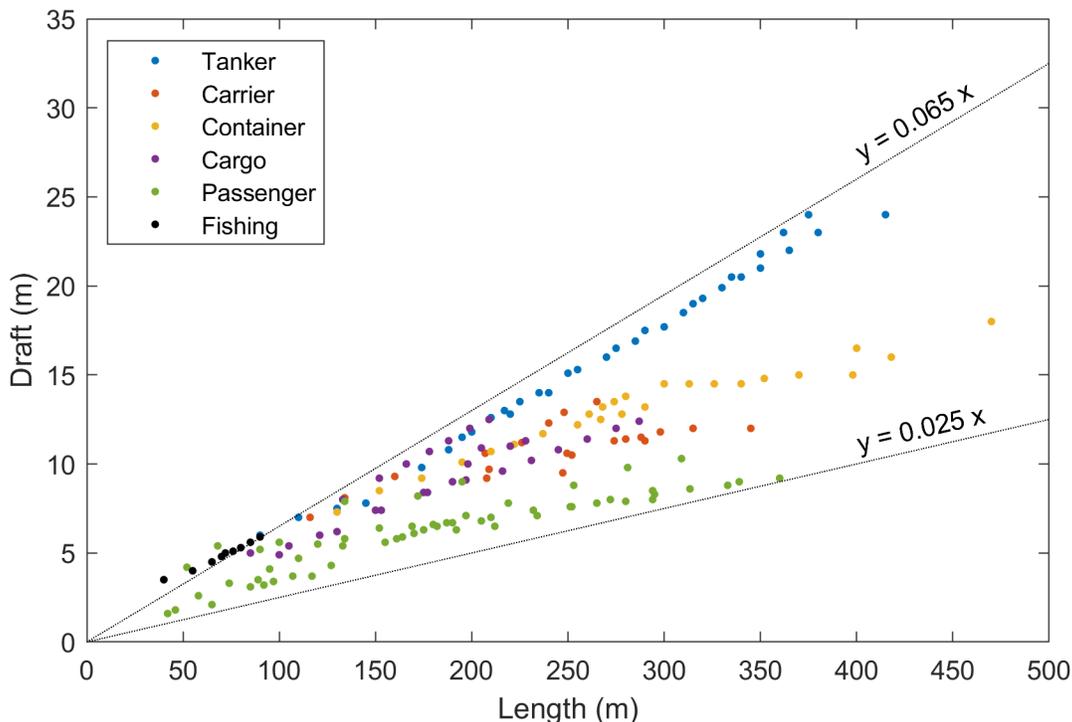
Figure 4.2: Length and draft of fully loaded ships according to PIANC (2015) data.

Table 4.6: Characteristics of self-propelled oil tankers per NYSDOT (2005).

Ship Name	Length (m)	Beam (m)	Light Draft (m)	Loaded Draft (m)	Light to Loaded Draft Ratio (%)
Kiristin Poling	85.6	12.2	2.7	5.2	52.3
Coral Queen	57.3	8.5	2.3	3.7	63.3
John B. Caddell	56.4	11.0	2.1	3.6	58.8
Patricia Gellatly	55.2	9.1	2.6	4.3	61.4
Patrick Sky	38.4	9.4	1.7	3.8	44.4
Scott Sky	35.7	9.8	1.7	3.2	52.8
Great Gull	84.1	16.8	2.9	5.1	57.8
Newtown Creek	98.8	15.2	3.4	5.1	65.5
North River	98.8	15.2	3.4	5.1	65.5
Owls Head	86.3	14.0	2.7	4.0	69.2
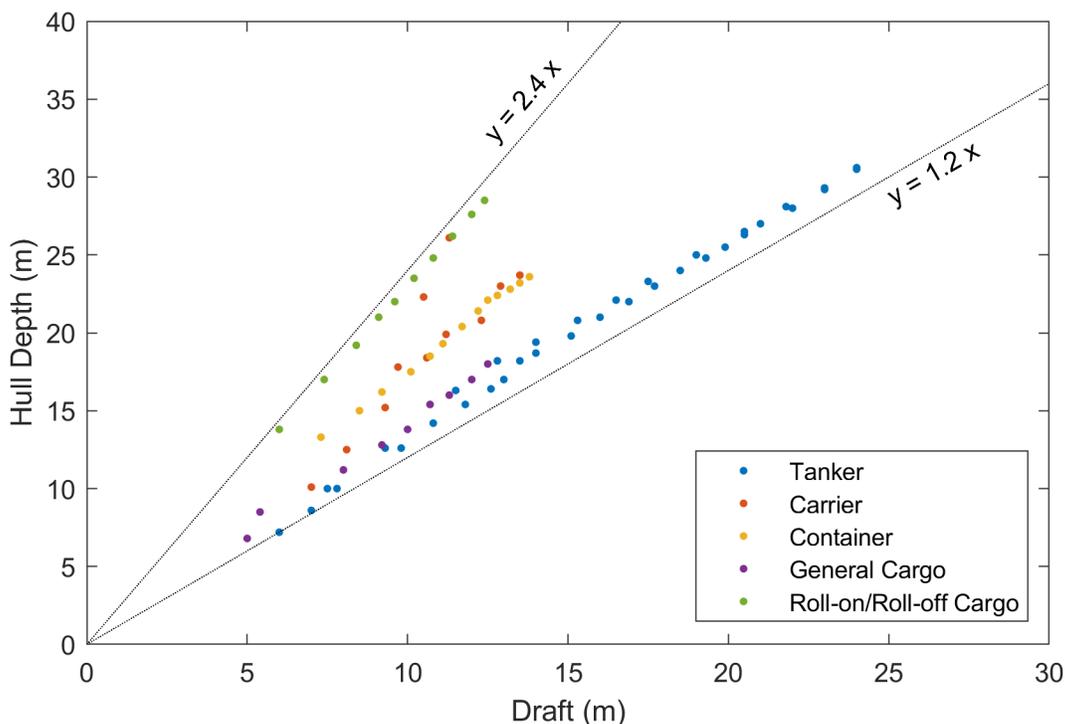
Figure 4.3: Hull depth and draft of fully loaded ships according to PIANC (2015) data.

4.5.1.3 Distance from AIS Antenna to Stern

The AIS antenna generally stands above the central control room of a ship. Modelers may estimate the distance between the AIS antenna and stern (rear end of the ship) according to the vessel type. For tankers, carrier ships, container ships, and cargo ships, the AIS antenna is usually located nearer to the ship's stern. In this case, the distance from the AIS antenna to the stern is estimated to be 15% to 30% of the ship length. In contrast, passenger ships and smaller boats have the AIS antenna toward the bow, then the distance from the AIS antenna to the stern may be 70% to 85% of the ship length. If no information is available, modelers may specify the AIS antenna as located in the middle of the ship (setting the distance as 50% of the ship length).

4.5.1.4 Distance from Stern to Propeller

Most ships have their main propeller(s) near the stern, so the modeler may specify the distance from the stern to propeller as about 2% of the ship length. However, some tugboats have their main propeller toward the bow or in the middle of the ship and a rudder-shaped fin on the aft side, so the distance from the stern to propeller can be set as 50% to 70% of the ship length in this case. The distance from the AIS antenna to the stern "ais_to_stern" and the distance from the stern to the propeller "dist_from_stern" are used during a simulation to identify the propeller location relative to the AIS tracking records.

4.5.1.5   Distance from Hull Bottom to Propeller Shaft

The parameter "prop_offset" indicates the vertical distance between the hull bottom and the propeller shaft (see Figure 4.4). Modelers should use a positive value for "prop_offset" if the propeller shaft is located lower than hull bottom (the hull's deepest point). In contrast, the "prop_offset" value should be negative if the propeller shaft is located higher than the hull bottom.

For merchant ships (tankers, carriers, container ships, cargo ships, and passenger ships), the propeller is not allowed to extend below the hull bottom. A small margin is included to ensure that the propeller is not damaged in the event of grounding, dry docking, or similar. Interference between the propeller and the seabed or a rock can damage the propeller blades, the propeller shaft, the gearbox, and the main engine itself. Therefore, if the hull bottom and propeller shaft distance is unknown, the modeler may specify this parameter value based on an estimate of the main propeller size and the ship's draft.
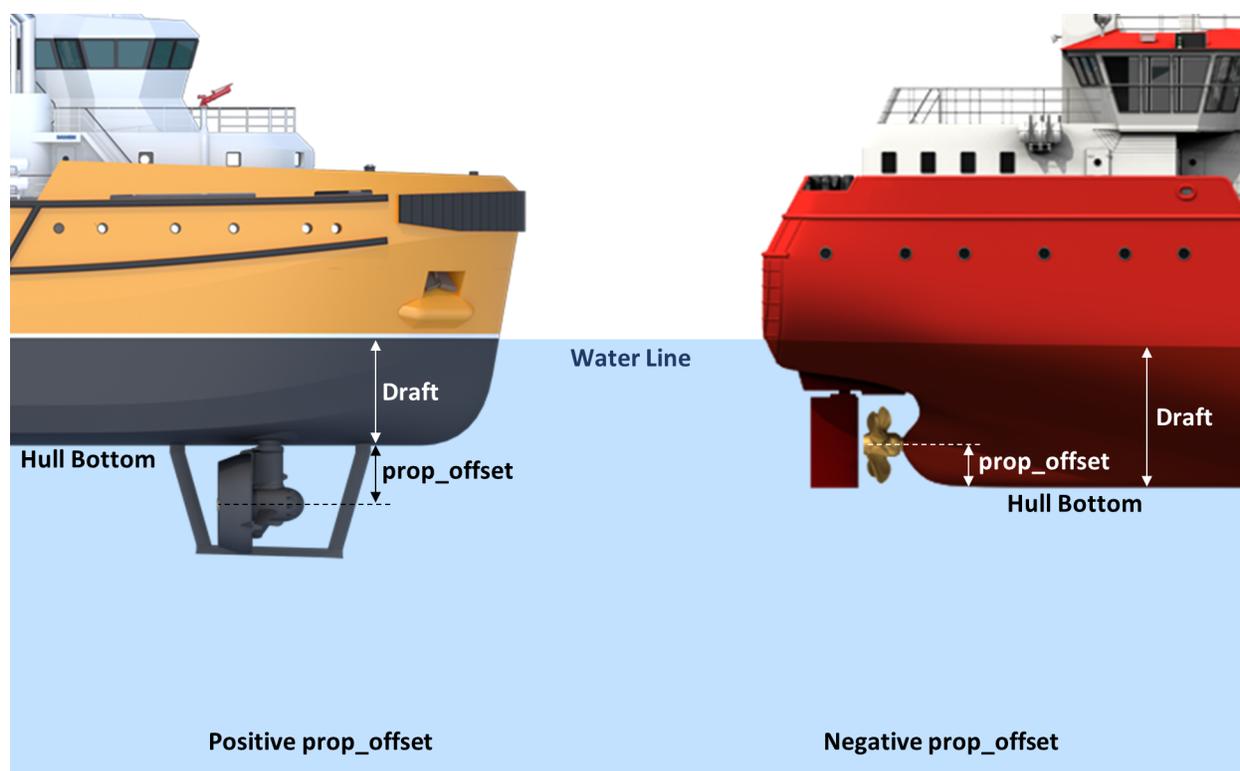
Figure 4.4: Propeller offset parameter for distance from the hull bottom to the propeller shaft.

4.5.1.6 Main Engine Power

Since ship owners in competitive markets are reluctant to disclose detailed information about their ships, it is difficult for the modeler to identify the installed power of the main propulsion systems for the ship of interest. Therefore, this section suggests some approaches to predict the installed main engine power based on ship dimensions. For instance, modelers may compute the deadweight tonnage using the identified vessel type and length and then estimate the installed engine power using the computed deadweight tonnage. The following describes the suggested process to estimate a ship's installed engine power.

Figure 4.5 shows data from PIANC (2015) on ships' overall length and deadweight tonnage. The deadweight represents the ship's loading capacity, including bunkers, fuel, lube oils, and other supplies necessary for the ship's operation. With these datasets, we identified the relationship between ship length (L) and deadweight tonnage (DWT) using the power function regression for ships overall and for each vessel type separately, as:

$$DWT = \begin{cases} 0.0021 \times L^{3.10} & \text{for All Vessels} \\[2ex] 0.0003 \times L^{3.52} & \text{for Tankers} \\[2ex] 0.0002 \times L^{3.50} & \text{for Carriers} \\[2ex] 0.0335 \times L^{2.57} & \text{for Container Ships} \\[2ex] 0.0028 \times L^{3.09} & \text{for General Cargo Ships} \\[2ex] 0.0160 \times L^{2.65} & \text{for Roll-on/Roll-off Cargo Ships} \\[2ex] 0.0037 \times L^{2.97} & \text{for Passenger Ships} \\[2ex] 0.0018 \times L^{3.15} & \text{for Fishing Boats} \end{cases} \tag{4.1}$$

PIANC (2015) includes some samples that relate the installed engine power (in hp) and deadweight tonnage at design draught, as shown in Figure 4.6. We conducted a regression analysis to define the installed engine power (P) as a function of deadweight tonnage (DWT) for these samples. In this case, the relationship shows different behaviors when the deadweight tonnage is greater than 50,000 tons vs. less than 50,000 tons, so we applied different regression functions for each condition. The regression results are presented in Equation 4.2 and Figure 4.6.

$$P(\text{hp}) = \begin{cases} 0.0326 \times DWT^{1.3167} & \text{for } DWT < 50,000 \text{ tons} \\[2ex] 64,696 \times \ln(DWT) - 650,483 & \text{for } DWT \geq 50,000 \text{ tons} \end{cases} \tag{4.2}$$
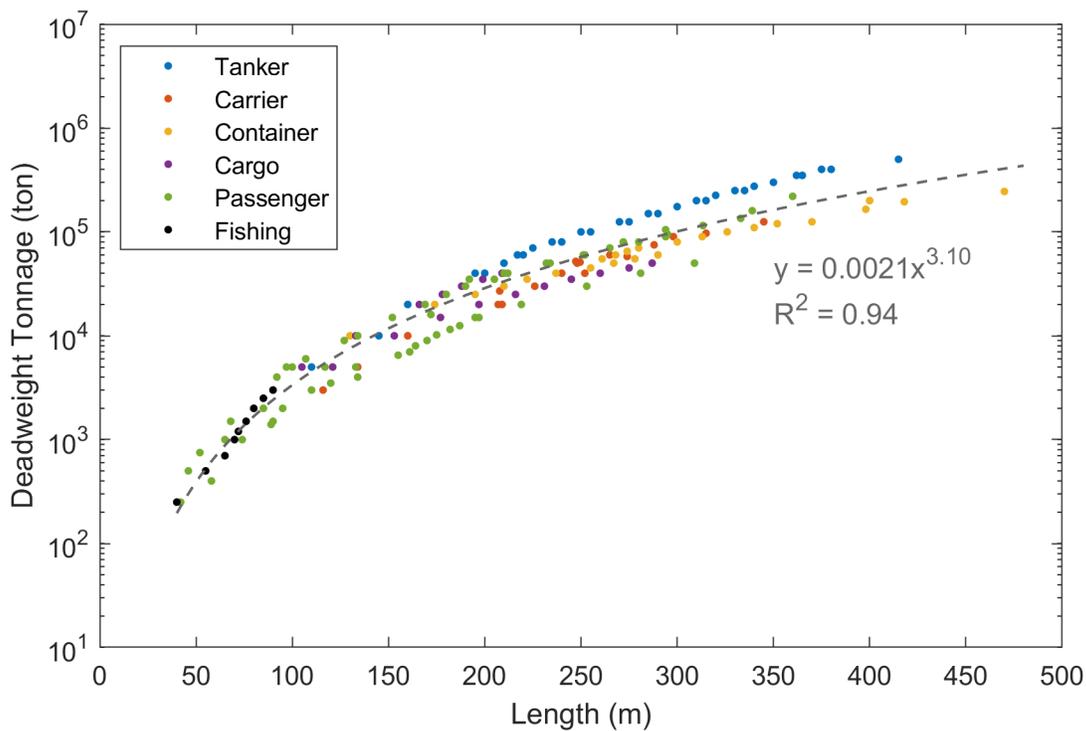
Figure 4.5: Length and deadweight tonnage based on PIANC (2015) data.
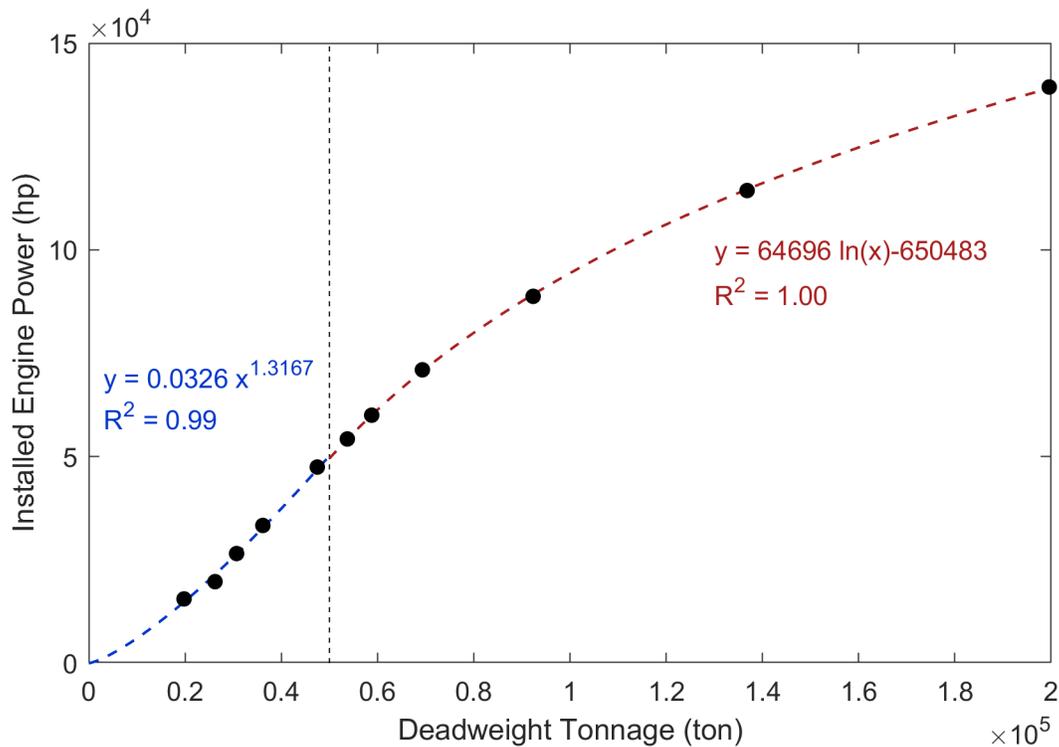
Figure 4.6: Installed engine power as a function of deadweight tonnage per PIANC (2015) data.

As a result of this analysis, modelers seeking to estimate missing ship data can use Equation 4.1 to calculate the deadweight tonnage using the identified vessel type and length, and then can employ Equation 4.2 to estimate the installed engine power using the previously calculated deadweight tonnage.

The PIANC (2015) data does not include sufficient information for ships with a length of less than 50 m (see Figure 4.5). Typically, deadweight tonnage information is not available for such small vessels, so the approach suggested above might not apply to small tugboats, which usually have high engine powers to push or pull a barge. Tugboats may also represent a large portion of ship traffic in harbor or bay areas. To fill the data gap, we collected 110 samples of ship dimensions and engine power for tugboats smaller than 50 m from a tugboat database website, TugboatInformation.com (2021). The collected tugboat dataset indicates a positive correlation between installed engine power (P) and ship beam (B), which can be expressed as the exponential function regression shown in Equation 4.3 and Figure 4.7. Therefore, modelers may employ this approach when estimating the installed engine power (in hp) for such small-sized tugboats.

$$P(\text{hp}) = 828.31 \times \exp\left(0.1587 \times B\right) \tag{4.3}$$
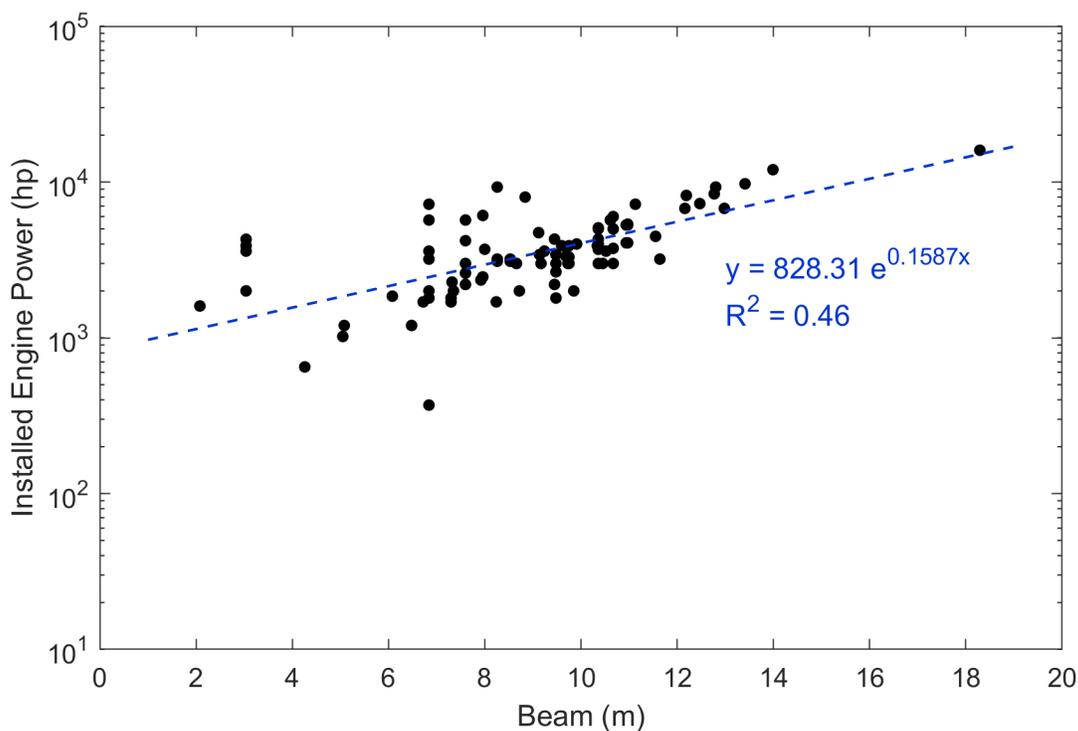
Figure 4.7: Installed engine power as a function of ship beam per TugboatInformation.com (2021) data.

4.5.2 Propeller Properties

4.5.2.1 Propeller Diameter

PIANC (2015) includes an empirical relation between propeller diameter D_p (m) and installed engine power P (hp), which is generally applicable to various vessel types of propellers. Empirical Equation 4.4 can be used to estimate the diameter of both ducted and non-ducted propellers.

$$D_p = 0.1636 \times \left(\frac{P}{1.341} \right)^{0.3656} \tag{4.4}$$

4.5.2.2 Propeller Hub Diameter

Propeller hub diameter is usually 15% to 20% of the propeller diameter, retaining high propeller efficiency. Sometimes, the propeller has a relatively larger hub, with a hub/propeller diameter ratio of approximately 22% to 30%; in this case, the propeller efficiency would be slightly lower (MAN, 2018).

4.5.2.3 Number of Blades

Propellers can have 2, 3, 4, 5, 6, or 7 blades. In general, the fewer blades, the higher the propeller efficiency will be. However, because of strength and vibration issues, 4-, 5-, and 6-bladed propellers are typically used on merchant ships, with four blades being the most common.

4.5.2.4 Pitch Ratio

The pitch ratio expresses the ratio of pitch to the diameter of the propeller. The propeller pitch indicates the distance the propeller screws itself forward through the water per revolution. Generally, the propeller manufacturer's manual provides the pitch ratio information. The pitch ratio typically falls between 0.5 and 2.5, with an optimal value for most ships closer to between 0.8 and 1.8 (MAN, 2018).

4.5.2.5 Blade Area Ratio

The blade area ratio (usually referred to as disk area coefficient) defines the developed surface area of the propeller in relation to its blade area. This area must be sufficiently large to avoid harmful cavitation that can lead to erosion, but not too large, as this will increase the frictional drag on the propeller. A ratio of 0.4 to 0.6 is typical for 4-bladed propellers. Highly loaded single propeller container ships can see values as high as 1.0 (MAN, 2018).

4.5.3   Applied Power for Tracking Data

The ship track file ("propwash_track.jnp") requires specification of the applied power for each track point as a fraction of either maximum engine power or maximum revolution speed. Modelers may specify the applied power based on the general engine operation guidelines for vessel types and sailing conditions described below.

For regular sailing, ships typically use about 75% of the installed engine power when they operate at the design service speed under normal load and weather conditions.

For berthing and departure maneuvering, PIANC (2015) recommends the applied power as about 5% to 15% of the installed engine power for the main propellers of large ships (e.g., tankers, carriers, container ships, and passenger cruises). A value of 5% might be applied for sheltered berth locations with bed protection and no currents (e.g., berthing in harbor basins). A value of 15% is recommended for exposed berth locations with riverine or tidal currents and bed protection (e.g., quay walls along the river). For smaller ships, the applied power for berthing and departure may be 30% to 40% of the installed engine power. Additionally, tugboats can operate at 75% to 100% of the installed power when they are maneuvering with pushing or pulling a barge.

Chapter 5

EFDC+ GUI Descriptions

Chapter 6

Case Studies

This chapter presents case studies conducted to demonstrate and validate the EFDC+ propeller wash modeling features coupled to hydrodynamic and sediment transport processes.

6.1.   Validation Using Flume Experiment Data

The purpose of this analysis is to evaluate the velocity formulations used in the EFDC+ propeller wash module (described in Chapter 2) by comparing them to the observation data from a published paper.

Hong et al. (2016) conducted a flume experiment to measure the flow velocity introduced by propeller wash under flat and non-erodible bed conditions. They used a recirculating flume of 30 m long, 0.7 m wide, and 0.6 m deep, where water was pumped from a reservoir to the flume slowly until the still water level was reached. A propeller was placed along the centerline of the flume. The propeller had a diameter of 0.075 m with three blades and a hub diameter of 0.016 m, and the propeller shaft was placed 0.2 m above the bed surface. While the propeller was rotating at 1,000 revolutions per minute (rpm), they collected instantaneous 3D velocity components using an Acoustic Doppler Velocity Profiler (ADVP), measuring the water column over a 3-cm vertical range with 1-mm resolution, with a sampling rate of 100 hertz (Hz) (i.e., 100 samples per second). Time-averaged velocities were obtained by varying the measuring times between 3 and 10 minutes according to the turbulence intensity. Specifically, the measuring time was comparatively longer for locations near the propeller and bed than at other locations.

Figure 6.1 compares the velocity profiles computed by the EFDC+ propeller wash module formulations to the ADVP measurements along the longitudinal distances at x/D_p = 1.47, 2, 2.67, 6, and 8. In this figure, the x-axis represents the velocity magnitude at each longitudinal location, and the y-axis indicates the vertical distance from the propeller axis. Hong et al. (2016) did not provide detailed information about the propeller specifications such as thrust coefficient, blade area ratio, and pitch ratio. Hence, this study computed the propeller wash velocity profiles by specifying those propeller parameters as presented in Table 6.1 marked with an asterisk, which are within the typical value ranges (refer Section 4.5.2). In Figure 6.1, the results show reasonable agreements

between the computed results and the measured flume data for both the zone of flow establishment ($x/D_p < 3.25$) and the zone of established flow ($3.25 < x/D_p$). Specifically, the EFDC+ propeller wash module formulations reproduced the maximum measured velocities well over all locations. The predictions are much better in the zone of established flow, especially near the bottom, than in the zone of flow establishment.

Table 6.1: Modeled propeller properties used for the Hong et al. (2016) experiment case.

Properties	Values
Propeller diameter	7.5 cm
Propeller hub diameter	1.6 cm
Thrust coefficient	0.20*
Blade area ratio	0.55*
Pitch ratio	0.80*
Applied revolution speed	1,000 rpm

Values assigned from typical ranges
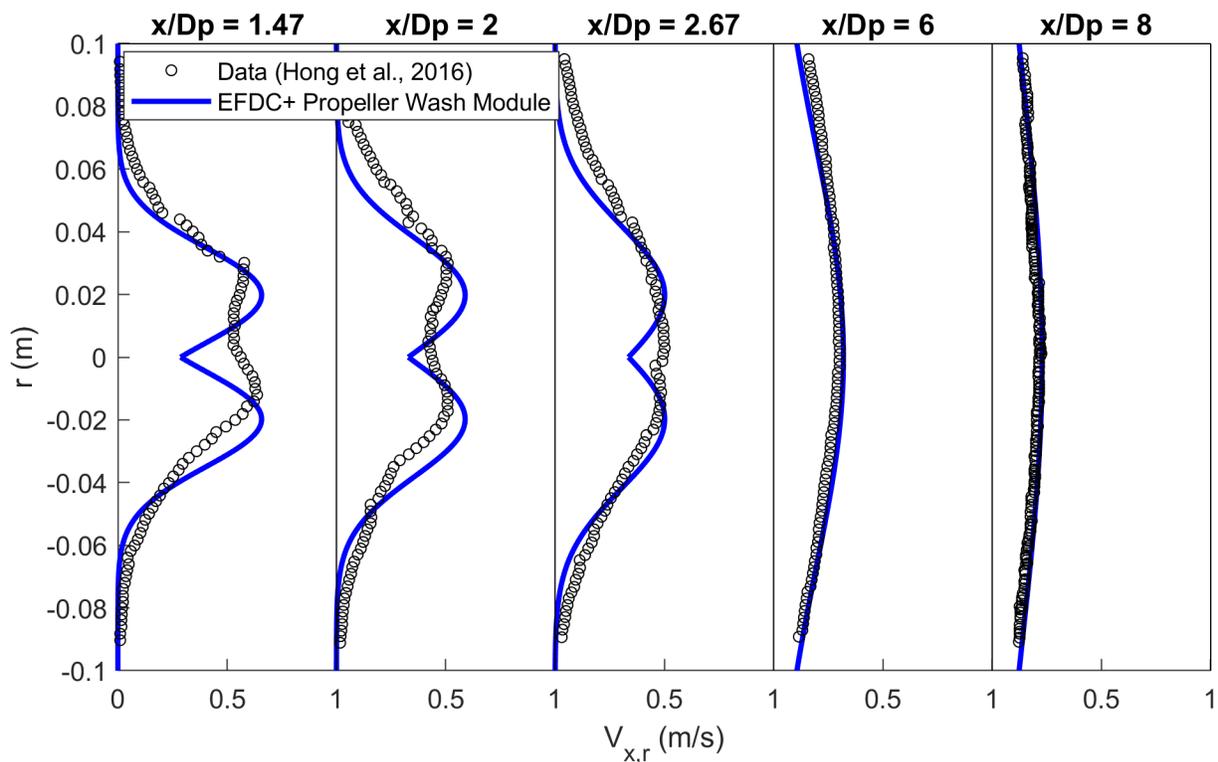
Figure 6.1: Velocity profiles from EFDC+ propeller wash module computations compared to Hong et al. (2016) experiment data.

6.2.   Validation Using San Diego Bay Field Data

During the development of the EFDC+ propeller wash module, DSI collaborated with Naval Information Warfare Center Pacific (NIWC-Pacific) via a Cooperative Research and Development Agreement (CRADA). Under this agreement, NIWC-Pacific provided propeller wash field data collected at a U.S. Navy facility in San Diego Bay, as reported in Wang et al. (2016). DSI then used the San Diego Bay data to test and validate the EFDC+ propeller wash module. This section evaluates the EFDC+ model performance for propeller wash-induced flow velocity, shear stress, and erosion depth using the field data provided by NIWC-Pacific.

Wang et al. (2016) conducted a field study to investigate propeller wash impacts under controlled conditions using a Navy-contracted tugboat (Tractor C-14). Figure 6.2 illustrates the configuration of the tugboat propeller wash measurements, and Table 6.2 provides the details for the tugboat characteristics. In the field study, the tugboat was moored between Piers 4 and 5 (Naval Base) with the bow pushing against the pier wall and the propellers thrusting toward the water from 13:50 to 14:30 Pacific Daylight Time (PDT) on July 19, 2012. During the survey, the propellers were operated at four different revolution speeds for different periods, starting with a period of about 7 minutes at 20 rpm, which is the lowest rpm possible without stalling the tugboat engine. The revolution speed was then increased to 50 rpm for about 11 min, followed by subsequent increases to 100 rpm for about 9 min and 150 rpm for about 9 min. After the 150 rpm period, the propellers were brought to a stop. An Acoustic Doppler Velocimeter (ADV) had been installed on the bottom at 110 meters behind the tugboat, to measure the water velocity at 15 cm above the bottom during the study period. The ADV-measured velocity data were then used to estimate the bottom shear stress. A Particle Image Velocimetry (PIV) was also deployed at the same location to capture the water velocity profile near the bottom, but the PIV velocity data were not available for the higher speed conditions (50 rpm and above) due to interference by resuspended sediments. Instead, the PIV images were used to analyze the bottom elevation changes during the survey period.

DSI developed a propeller wash model using EFDC+ for the San Diego Bay tugboat test area. Figure 6.3 presents the model grid cells, bottom elevations, tugboat location, ADV and PIV locations, and sub-grid points (showing the simulated propeller wash velocities as an example). The model domain covered the area around Piers 4 and 5, using a Cartesian horizontal grid of 4,556 cells with a uniform cell dimension of 10 m × 10 m. A vertical grid used ten layers for the water column. Within the model domain, bottom elevations varied between -11.74 m and -8.00 m, with a mean elevation of -9.72 m based on the Mean Lower Low Water (MLLW) vertical datum. The bathymetry data was provided by NIWC-Pacific.

For the EFDC+ hydrodynamic module, the model applied a time series of tidal conditions to open boundary cells. For the EFDC+ sediment transport module, the model used the SEDZLJ approach (see Steps 8 and 11 in Chapter 3). Because no data were available to determine sediment bed properties in this area (e.g., particle sizes, erodibility, porosity), a representative sediment bed configuration was defined by adopting sediment data sources from other harbor areas. Specifically, the sediment bed was assumed to have a 30 cm thickness using a vertical grid of five layers. The sediment content fractions were different for each layer to represent vertically-varied sediment properties observed in other harbor areas. The arithmetic average composition of the five sediment layers consisted of 60% clay, 20% silt, 10% fine sand, and 10% coarse sand.
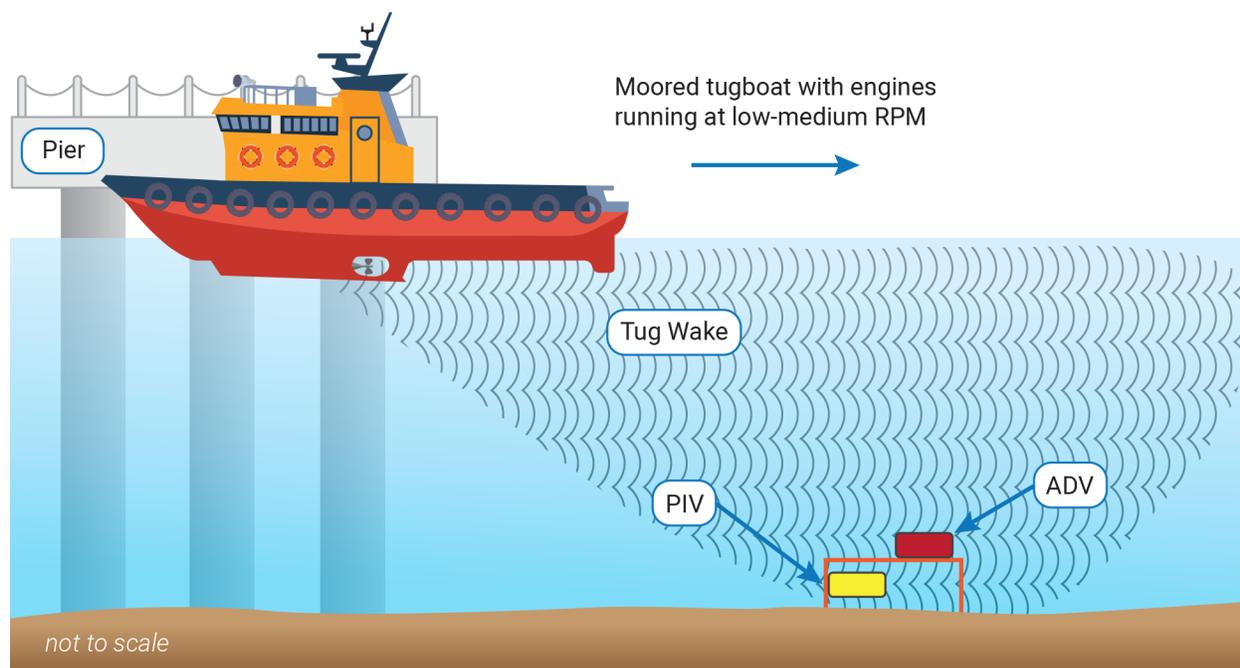
Figure 6.2: Configuration of tugboat propeller wash measurements.

Table 6.2: Tugboat Tractor C-14 information and field study conditions.

Characteristics	Values
Ship length	28.65 m
Ship beam	10.36 m
Ship draft	3.35 m
Water depth	9.14 m
Underkeel clearance	2.99 m
Ship speed	0 m/s
Installed engine power	4,800 hp
Propeller type	Ducted propellers
Number of propellers	2
Number of propeller blades	4
Propeller diameter	2.28 m
Propeller thrust coefficient	0.39
Distance from ship stern to propeller	15.24 m
Distance between propellers	4.88 m
Distance from water surface to propeller axis	4.88 m
Distance from propeller axis to bottom	4.26 m
Applied revolution speeds	20, 50, 100, 150 rpms
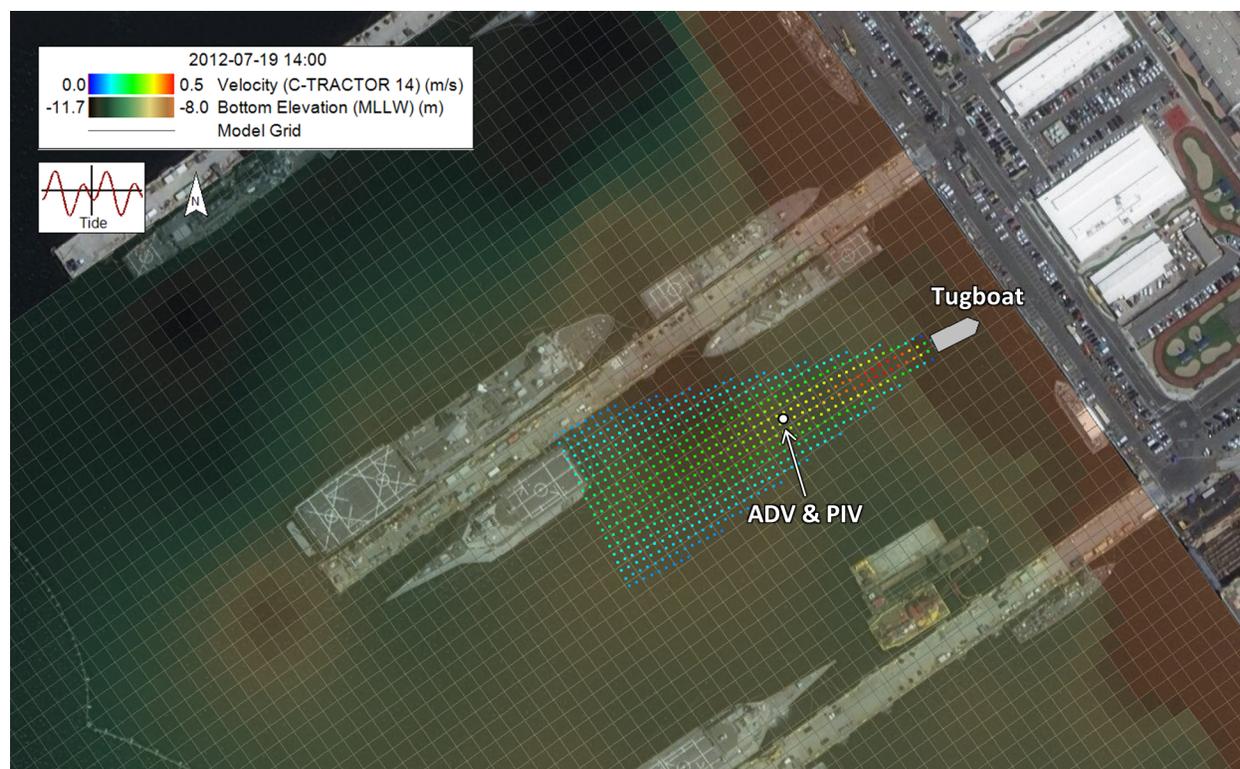
Figure 6.3: Model conditions for the San Diego Bay field test case.

For the EFDC+ propeller wash module, the model used the tugboat and propeller specifications presented in Table 6.2. The sub-grid configuration for the tugboat was set as 225 m in length and 100 m in width, including 50 points in the longitudinal dimension and 20 points in the lateral dimension. The model simulated the propeller operations for different revolution speeds (20, 50, 100, and 150 rpms), as mentioned above.

6.2.1 Near-bed Flow Velocity

This study evaluated the propeller wash velocities simulated using the EFDC+ propeller wash module at a sub-grid point near the ADV location from the model, comparing them to the ADV-measured velocities. Both the sub-grid-based model results and the ADV data represented the propeller wash-induced velocities at the bottom of the waterbody (water-sediment interface). Figure 6.4 presents the ADV-measured data and model results for the propeller wash velocities at the ADV site. In this figure, the x-axis indicates relative times (in minutes) from the time the propeller-induced velocity was first detected, and the y-axis shows velocity magnitudes. Vertical black lines represent the effective starting time for each rpm operation.

In Figure 6.4, the ADV raw data (grey line) show near-bottom flow velocities with large fluctuations due to turbulence. It is important to note that the measured velocities with propeller operations may include influences from other sources. For example, the applied propeller revolution speeds (20, 50, 100, 150 rpms) were estimated and controlled by the tugboat captain, so the actual

rotating speeds could be unsteady and inconsistent, especially for lower speeds (Wang et al., 2016). Additionally, the ADV signals could have been disturbed by other ship traffic nearby or by flow circulation due to pier structures. To address such influences when analyzing the ADV-measured data, the average and standard deviation of the fluctuating velocities were considered for each rpm run. Figure 6.4 uses red markers for the average data values and displays red whiskers for the standard deviation extending from the average points. Overall, the observed velocities increased with the propeller rpm, although the increase was not linear. For instance, when the propeller speed increased from 100 rpm to 150 rpm (a 50% increase), the average velocity increased only from 0.53 m/s to 0.57 m/s (an 8% increase).
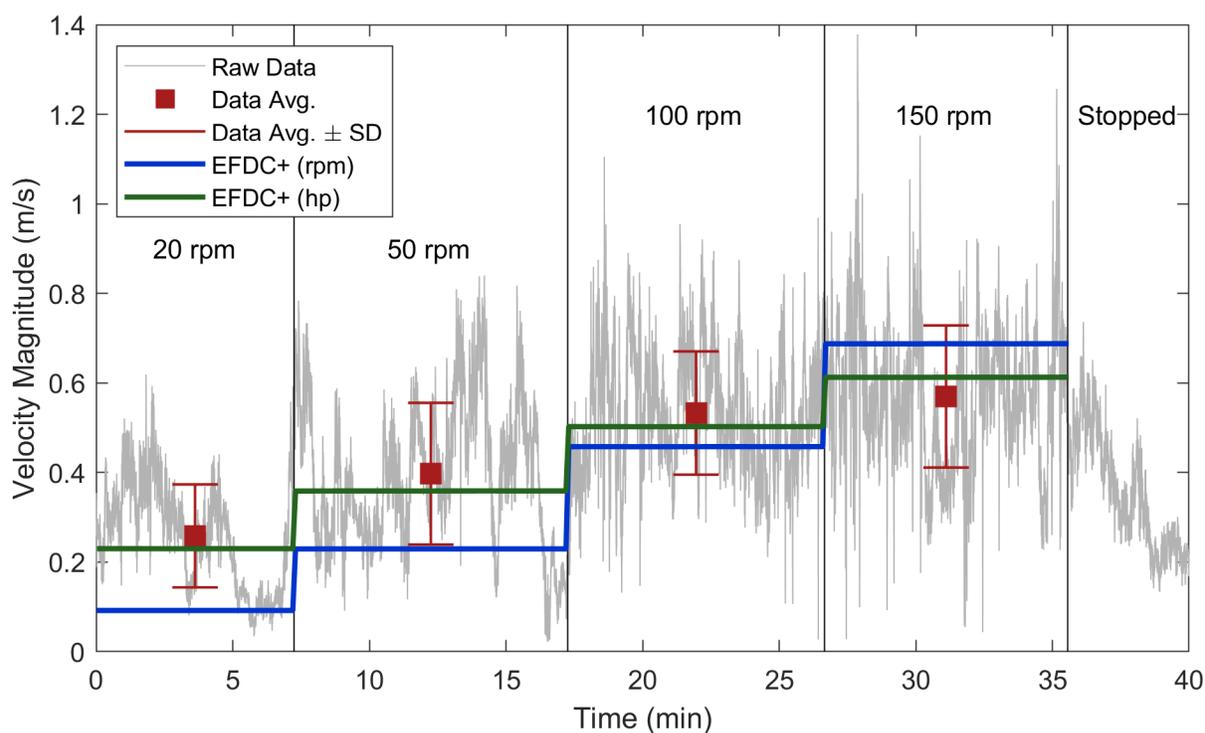
Figure 6.4: Propeller wash velocity from ADV-measured data and model results at 110 m behind tugboat Tractor C-14.

Figure 6.4 shows the simulated propeller wash velocities for each propeller operation speed as a blue line. The model results are presented as a step function of the applied rpms because the EFDC+ propeller wash module computed the fixed tugboat's propeller wash velocities at a sub-grid point using the analytical formulations in Chapter 2. Overall, the simulated propeller wash velocities increased linearly as the applied rpms increased. It is the expected result because the velocity magnitudes in a propeller wash field (see Equations 2.7 and 2.11) are dependent on the efflux velocity V_0, which has a linear relationship with the applied propeller revolution speed, as described in Equation 2.1. For this simulation, the average propeller wash velocity magnitude observed for a rotational propeller speed of 100 rpm was reproduced by the model. The model underestimated the velocity magnitudes for lower rotational propeller speeds at 20 and 50 rpms, but the underestimation diminished as the rotational speed increased. For the 150 rpm period,

the simulated velocity magnitudes exceeded the measured values, but the model results were still within a standard deviation range from the average data value.

In addition to the rpm-based simulation, the model was also used to simulate propeller wash velocities when applying four different engine power levels (320, 800, 1600, 2400 hp); these model results are shown as the green lines in Figure 6.4. This hp-based simulation was implemented by assuming the applied engine power for each rpm condition as follows. Wang et al. (2016) stated that operating speeds for the tugboat Tractor C-14 typically range between 100 rpm and 200 rpm during ship husbanding tasks (e.g., customs formalities, fueling, supply activities, and repairs). Based on this information, it was assumed that 50% of the installed engine power would be required for operating the propellers in the ship husbanding conditions, which indicates a median revolution speed of 150 rpm. This assumption is supported by the information in Wang et al. (2016) indicating that the low to medium propeller rotation speeds of tugboat Tractor C-14 were in the 20 to 150 rpm range. Additionally, the efflux velocity at 150 rpm (calculated by Equation 2.1) is almost the same as the efflux velocity at 2,400 hp (calculated by Equation 2.5), which is 50% of the installed engine power of the tugboat (4,800 hp; see Table 6.2).

The applied engine power for each of the four operation periods was then estimated with respect to the applied rpm levels relative to the 150 rpm median, as follows: 320 hp for 20 rpm, 800 hp for 50 rpm, 1,600 hp for 100 rpm, and 2,400 hp for 150 rpm. The model results indicate that the engine power-based simulation performed much better in reproducing the ADV-measured velocities than all of the comparable propeller revolution speeds. The engine power-based model also simulated the velocity magnitudes to be increasing non-linearly with the applied engine power, which provides a better representation of the field data. These results are expected, because the efflux velocity and the applied engine power are non-linearly related for the EFDC+ analytical solutions as defined through Equations 2.2 to 2.5.

Based on the model-to-ADV data comparison results, we conclude that the EFDC+ propeller wash module can reasonably predict propeller wash velocities at berthing/docking facilities.

6.2.2   Bottom Shear Stress

Using the ADV-measured velocity data, Wang et al. (2016) calculated the bottom shear stress based on a modified Turbulent Kinetic Energy (TKE) method (Kim et al., 2000), which is defined as:

$$\tau_b = 0.9 \times \rho_w \times \overline{w'^2} \tag{6.1}$$

where,

τ_b : bottom shear stress (N/m^2)

ρ_w : water density (kg/m^3)

$\overline{w'^2}$: temporal average of squared vertical velocity fluctuation (m^2/s^2)

The modified TKE method requires only the vertical velocity fluctuations to address the total energy balance regarding the propeller wash turbulence and the bottom shear stress dissipation. Hence, this approach has widely been used with ADV velocity data because the ADV provides a lower level of noise errors for vertical velocity variances compared to the noise errors associated with horizontal velocity fluctuations (Voulgaris and Trowbridge, 1998). In Wang et al. (2016), the vertical velocity fluctuation statistics ($\overline{w'^2}$) were calculated over an averaging window of 10 seconds, which corresponded to 300 ADV data points with a sample rate of 30 Hz.

This study used the shear stress values estimated using the modified TKE method by Wang et al. (2016) as measurements for the bottom shear stress induced by the tugboat propeller wash. The calculated modified TKE values were compared to the shear stress simulated by the EFDC+ propeller wash module (Equation 3.1) at a sub-grid point near the ADV location. Figure 6.5 presents the modified TKE method-based measurements and the model results for the bottom shear stress at the ADV site. In this figure, the x-axis shows relative times (in minutes) measured from when the propeller-induced velocity was first detected, and the vertical black lines represent the effective starting time for each rpm operation. The left y-axis indicates the shear stress (in N/m^2) as a gray line, and the right y-axis indicate the cumulative shear stress over time (in N/m^2-Hour), presented with colored lines.
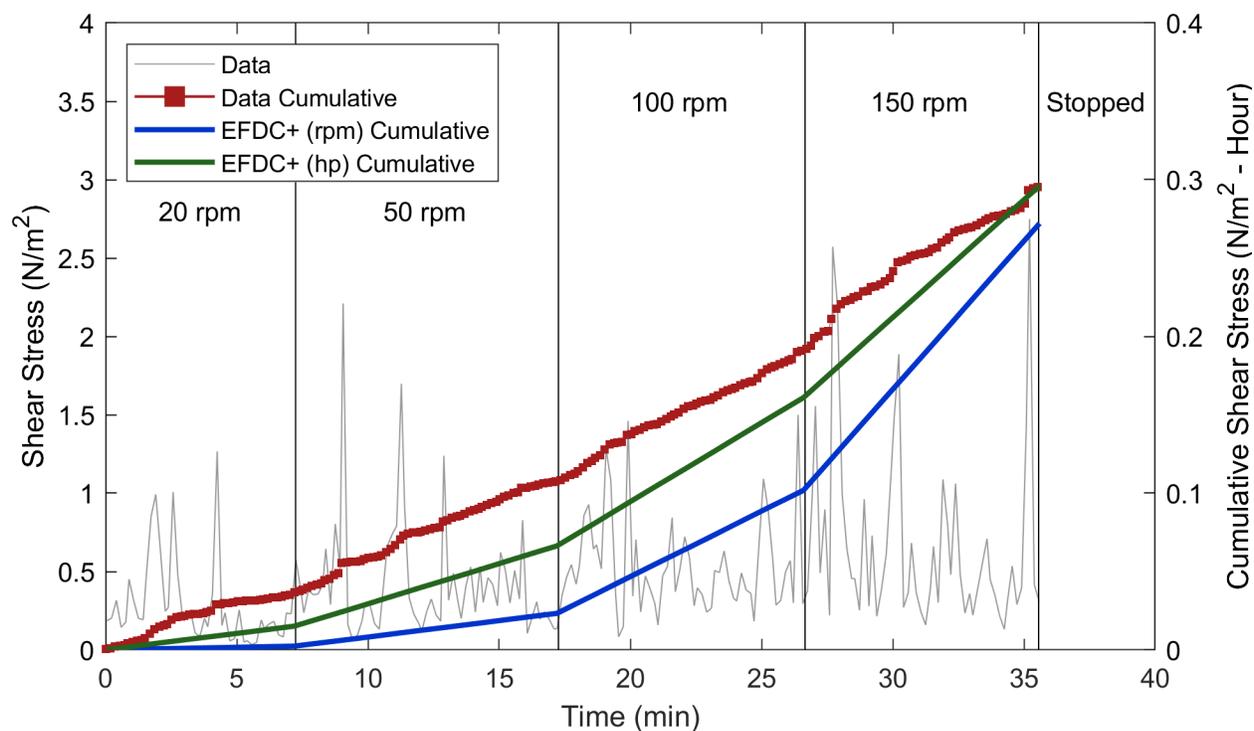
Figure 6.5: Propeller wash shear stress from modified TKE method-based data and model results at 110 m behind tugboat Tractor C-14.

In Figure 6.5, the measured bottom shear stress (N/m^2) from the modified TKE method (grey line) presents several spikes during the propeller operations. Overall, the measured data generally showed higher shear stresses at higher propeller rpm, but the peak magnitude was not proportional

to the propeller speeds. Specifically, the peak magnitude of the observed shear stress varies at each rpm period as: 1.2 N/m^2 for 20 rpm, 2.2 N/m^2 for 50 rpm, 1.4 N/m^2 for 100 rpm, and 2.6 N/m^2 for 150 rpm. To examine the total effects of the propeller wash shear stress including the mean and temporal variations over time, the cumulative shear stress (N/m^2-Hour) was calculated for the measurements during the study period, about 36 min. The red line with markers represents the cumulative distribution of the measured shear stress (N/m^2-Hour), which integrates the measured instantaneous shear stress (gray line). The cumulative shear stress curve presents higher increase rates (slope) as the propeller speeds increase, and it also shows several jumps at the 150 rpm period due to the high magnitude spikes. The total cumulative shear effects reached about 0.295 N/m^2-Hour at the end of the propeller operations.

Figure 6.5 also displays the model results for the bottom shear stress as the cumulative distribution: the blue line is for the propeller rotation speed-based simulation (20, 50, 100, 150 rpm) and the green line is for the engine power-based simulation (320, 800, 1600, 2400 hp). Recall that the EFDC+ propeller wash module computes the propeller wash bottom shear stress as a function of the propeller wash velocity at the bottom (see Equations 3.1 and 3.2). So, for both rpm- and hp-based models, the slope of the cumulative shear stress curve increased as the applied propeller speed or engine power increased during the simulation. These model results are consistent with the behaviors shown in the measured cumulative shear stress data curve. At the end of the propeller operations, the rotation speed-based simulation result (0.272 N/m^2-Hour) underestimated the measured cumulative effects by only 8%, and the engine power-based simulation result reached 0.296 N/m^2-Hour, which is almost identical to the measured cumulative shear stress of 0.295 N/m^2-Hour. These results support the conclusion that the EFDC+ propeller wash module performs well in estimating propeller wash-induced bottom shear stress.

6.2.3 Erosion Depth

Wang et al. (2016) also collected PIV images from the bottom at 110 meters behind the tugboat Tractor C-14 during the study period and evaluated the bottom elevation changes due to the tugboat propeller wash using the PIV images captured at different times. In this study, the erosion depths simulated for an EFDC+ model grid cell at a given PIV location were compared to the PIV-measured erosion depths. Note that the model-to-data comparison for erosion depths is conducted based on the model grid cell, whereas the comparison analyses for near-bed velocity and shear stress were performed based on the sub-grid point. Figure 6.3 displays the model grid cells, propeller wash sub-grid points, and PIV location specified in this study.

Figure 6.6 compares the PIV-measured data and the model results for the propeller wash-induced erosion depth. In this figure, the x-axis shows relative times (in minutes) from the time the propeller-induced velocity was first detected, and the vertical black lines represent the effective starting time for each rpm operation. The y-axis indicates the cumulative erosion depth (in mm) during the study period, showing the depths increasing from top to bottom.

In Figure 6.6, the measured PIV data (red markers) indicate that bed erosion did not occur during the 20 rpm period, likely due to low shear stress; erosion started while the propeller speed was at 50 rpm. The erosion depth then increased continuously while the propellers were rotating and reached 1.85 mm at 34 minutes. The erosion rate (curve slope) was notably higher at 150 rpm than

during other periods. When the propellers were brought to a stop (after about 36 min), the erosion depth decreased (indicating bottom elevation increase) as the sediments resuspended during the propeller operations were re-deposited on the sediment bed.

The blue line in Figure 6.6 represents the model results for erosion depths from the propeller rotation speed-based simulation (20, 50, 100, 150 rpm), while the green line in the figure represents the engine power-based simulation (320, 800, 1600, 2400 hp). Overall, the measured erosion depths over the study period were well reproduced in the hp-based simulation (green line). The hp-based model simulated the propeller wash erosion starting at the 50 rpm (800 hp) period and predicted the erosion depth of 1.82 mm at 34 minutes, which is consistent with the observed erosion behavior. Additionally, the model reproduced the deposition of the resuspended sediment after the 36 minutes of the propeller operations. From the rpm-based simulation (blue line), the propeller wash erosion did not occur until 17 minutes after the start time, likely due to the low shear stress predicted for the 20 and 50 rpm periods. Consequently, the maximum erosion depth (1.55 mm) was also underestimated by about 16%, although the temporal trend of the erosion depth was sufficiently well reproduced by the rpm-based model.
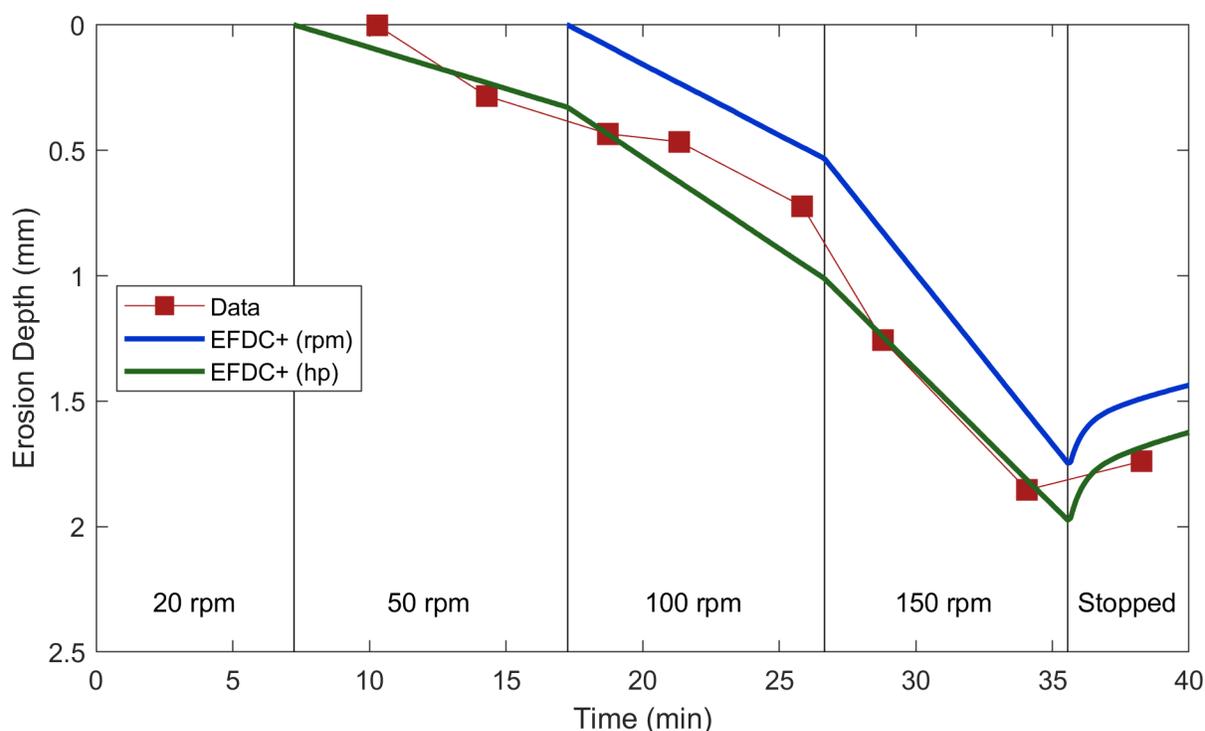
Figure 6.6: Erosion depth from PIV-measured data and model results at 110 m behind tugboat Tractor C-14.

This study also evaluated the model performance for the erosion depth quantitatively using the Nash-Sutcliffe Efficiency (NSE) coefficient, which is calculated as:

$$NSE = 1 - \frac{\sum\limits_{i=1}^{N} (M_i - O_i)^2}{\sum\limits_{i=1}^{N} (O_i - \overline{O})^2} \tag{6.2}$$

where,

N : number of observations

$\overline{O}$: average of observed erosion depths

O_i : observed erosion depth at i^{th} data point

M_i : simulated erosion depth corresponding to i^{th} data point

The NSE coefficient can range from -∞ to 1 where NSE of 1 indicates that the model reproduces the observed data perfectly and NSE of 0 indicates that the model prediction is as accurate as the average of the observed values. The resultant NSE value was 0.80 for the propeller revolution speed-based simulation and 0.97 for the engine power-based simulation. Thus, the quantitative evaluation also suggests that the EFDC+ propeller wash module can accurately predict propeller wash-induced bed erosion at berthing/docking facilities.

6.3.   Demonstration of Sediment Transport Processes

This section presents test cases that demonstrate how the propeller wash modeling features work with the two sediment transport modules available in EFDC+: Original EFDC Sediment Transport (van Rijn, 1984a,b,c) and SEDZLJ Sediment Transport (Jones and Lick, 2001). This demonstration examines several components (i.e., scour profile, erosion depth, and sediment mass balance) to evaluate whether the EFDC+ simulation results provide a good representation of the sediment transport processes induced by the propeller wash.

Figure 6.7 illustrates a synthetic channel's dimensions with the sediment bed and propeller setup used for the demonstration models. These model conditions were determined based on the site and propeller dimensions used in the San Diego Bay tugboat test case (see Section 6.2). Specifically, the modeled channel had a length of 500 m, a width of 100 m, a uniform 0 m elevation for the channel bottom (i.e., sediment bed surface), and a water depth of 10 m. The ambient background velocity of the water was 0.1 m/s flowing from west to east, and the model allowed flow and sediments to exit without reflection through an open boundary at the east end of the model domain. The horizontal model grid had a uniform cell size of 5 m × 5 m over the model domain, and the vertical grid used five layers for the water column. The channel's sediment bed had a 0.1 m thickness using a vertical grid of five layers (2 cm thick each layer). The physical and erosional properties of the sediment bed (i.e., particle sizes, erodibility, and porosity) were specified differently for each demonstration model depending on the purpose of each test. The demonstration models implemented geomorphic feedback between hydrodynamic and sediment transport simulations (i.e., bed elevation changes predicted by the sediment transport computation update the bathymetry used in the hydrodynamic computation for the next time step), leading to more appropriate flow field and sediment transport behavior.

A four-blade propeller with a 2.5 m diameter was placed 5.5 m above the sediment bed surface at a fixed location, as shown in Figure 6.7. Table 6.3 provides the detail specifications of the modeled propeller. The sub-grid configuration for the propeller was set as 400 m in length and 100 m in width, including 160 points in the longitudinal dimension and 40 points in the lateral dimension. All test cases had the same total simulation period of 120 minutes. The propeller was operated at the fixed location to generate a propeller wash eastward for the first 30 minutes during the simulation; the propeller was then stopped, and the resuspended particles were re-deposited to the sediment bed for the remaining 90 minutes. For each test case, the demonstration models applied different fractions of the maximum engine power (5,000 hp) to examine the propeller wash effects on the sediment bed. Note that all demonstration models were set to simulate a hydrodynamic flow field without propeller momentum effects (see "ISPROPWASH" = 1 in Section 4.1). Hence, during the simulation, the resuspended sediments in the water column were transported downstream only by the background ambient current (0.1 m/s flowing from west to east).
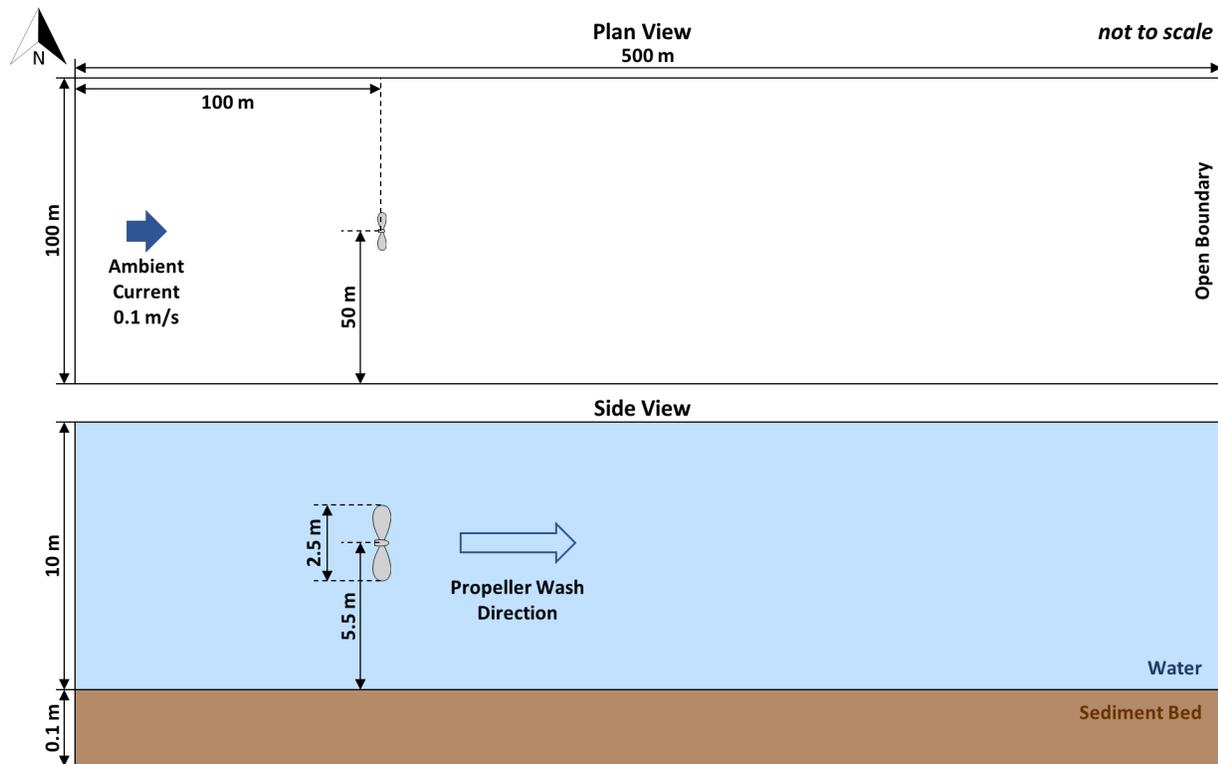
Figure 6.7: Channel dimensions used for sediment transport demonstration models.

Table 6.3: Propeller specifications used for the sediment transport demonstration models.

Characteristics	Values
Number of blades	4
Propeller diameter	2.5 m
Propeller hub diameter	0.2 m
Blade area ratio	0.8
Pitch ratio	1.0
Thrust coefficient	0.45
Maximum engine power	5,000 hp

6.3.1   Original EFDC Sediment Transport Module

The Original EFDC Sediment Transport approach applies separate computation processes for cohesive and non-cohesive sediments based on van Rijn's sediment transport equations (van Rijn, 1984a,b,c). Therefore, this study conducted separate demonstration tests for sediment beds with cohesive particles and non-cohesive particles.

6.3.1.1   Cohesive Sediments

The first demonstration model used a representative cohesive sediment bed condition consisting of 50% fine silt (particle size $d_s = 16$ μm) and 50% coarse silt ($d_s = 50$ μm), with a porosity of 0.8. The physical and erosional properties of the cohesive sediment bed were set to be uniform horizontally and vertically. For the propeller wash computation, the model applied a constant engine power of 500 hp (i.e., 10% of the maximum engine power) for the first 30 minutes of the simulation; then the propeller was turned off, allowing the suspended sediments to settle for the next 90 minutes.

Figure 6.8 displays the 2D plan view of the bottom elevations from the Original EFDC cohesive sediment bed simulation. The model provided a single value of bottom elevation for each grid cell, and this figure applies a smoothed color map for display purposes. In this figure, the colors represent the changes in bottom elevation following the 2-hour simulation; the red area indicates a decrease in bottom elevation (erosion), and the blue area indicates an increase in bottom elevation (deposition). A gray marker indicates the propeller location. The model results showed that the propeller wash formed a major scour area starting at about 20 m downstream of the propeller; the maximum scour depth of 6.7 cm was predicted at 45 m downstream. The propeller wash-induced erosion then decreased with distance and dispersed laterally until about 300 m away from the propeller. The simulation results also indicated that the sediments resuspended by the propeller wash were mostly redeposited to the sediment bed outside the propeller wash-impacted erosional area, with the predicted deposition thickness reaching a maximum of 0.3 cm.

Figure 6.9 presents the longitudinal profiles of the bottom elevations aligned with the propeller axis at different times (5, 10, 20, 30, and 120 minutes) during the simulation. Overall, the model provided similar longitudinal scour patterns at all the times considered. The propeller wash-induced scour started at 20 m behind the propeller, and the erosion depth increased dramatically until 45 m downstream, where the maximum scour depth of 6.7 cm occurred. After the maximum scour point, the erosion depth decreased with distance. In terms of temporal variation, the scour depth increased approximately linearly with the time during which the propeller was rotating (5, 10, 20, and 30 minutes). At the maximum erosion location, the model predicted scour of 2.2 cm for the first 10 minutes, 2.3 cm for the next 10 minutes, and 2.2 cm for the last 10 minutes of the propeller rotating period. At the end of the simulation (120 minutes), the bottom elevations 100 m downstream and farther from the propeller increased slightly compared to the bottom elevations at 30 minutes. This result indicates that the propeller wash-induced resuspended sediments were transported downstream as suspended load and were redeposited to the sediment bed after the propeller stopped.
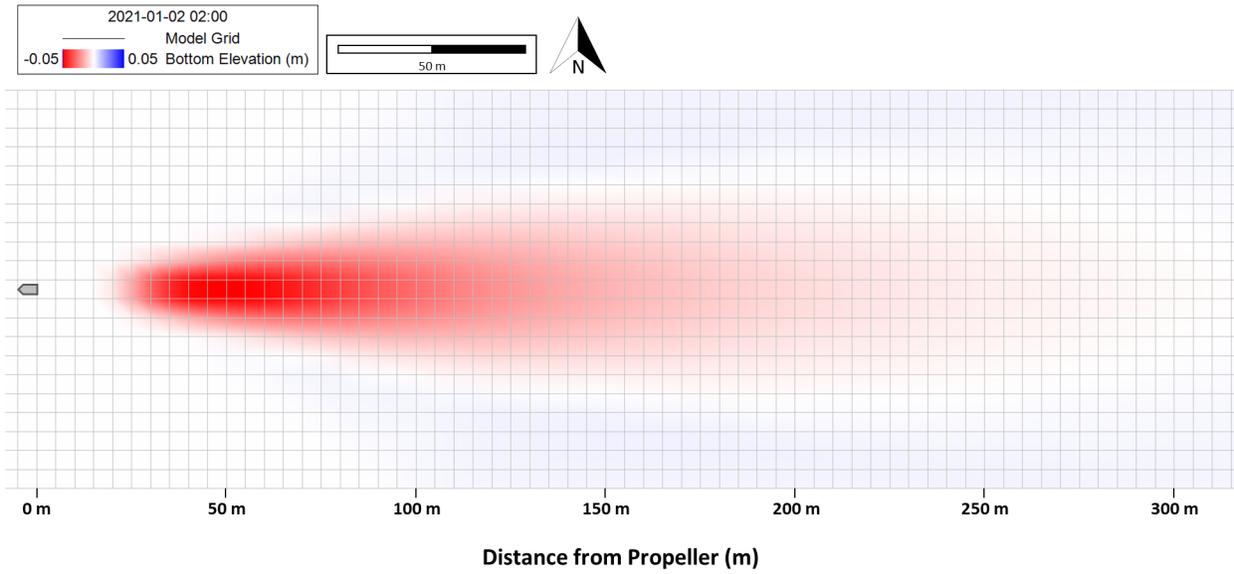
Figure 6.8: Plan view of bottom elevations simulated from a cohesive sediment bed model.
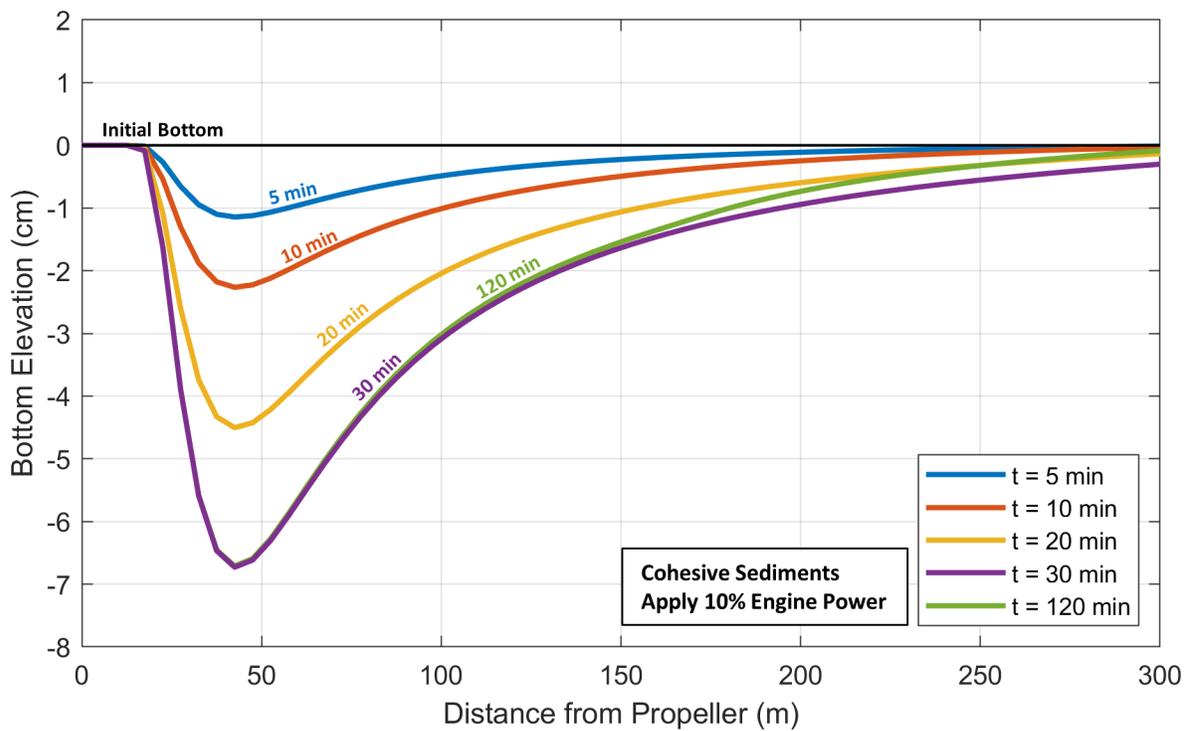
Figure 6.9: Scour profiles at different times from the cohesive sediment bed simulation.

Figure 6.10 presents the changes in thickness of the five sediment bed layers during the simulation at the cell where the maximum scour occurred (45 m behind the propeller), along with the corresponding bottom elevation changes. In this figure, Bed Layer 5 indicates the top layer, and Bed Layer 1 represents the bottom layer of the sediment bed (the Original EFDC Sediment Transport approach assigns a sediment bed layer number from bottom to top). At the beginning of the simulation, each bed layer had a 2 cm thickness specified as an initial model condition. When the simulation started, the thickness of Bed Layer 5 (top layer) decreased as the propeller wash caused the erosion at this cell (channel bottom elevation decrease). Once the top layer's thickness reached zero (after about 8 minutes), Bed Layer 4 began to be eroded as this layer was exposed to the sediment bed surface (water-sediment interface). This erosion process continued for the bed layers below for the 30 minutes during which the propeller wash was applied. Bed Layers 2, 3, 4, and 5 showed an almost identical decrease rate (slope) of their thickness during the simulation, because this demonstration model defined the physical and erosional properties of the sediment bed to be uniform horizontally and vertically. After the 30 minutes of propeller rotating, the total bed layer thickness was reduced from the original 10 cm to 3.3 cm (2 cm for Bed Layer 1 and 1.3 cm for Bed Layer 2), which is consistent with the resultant bottom elevation of -6.7 cm. Through this analysis, it was possible to check how the sediment bed layers behaved vertically while the sediment bed was being scoured due to the propeller wash.
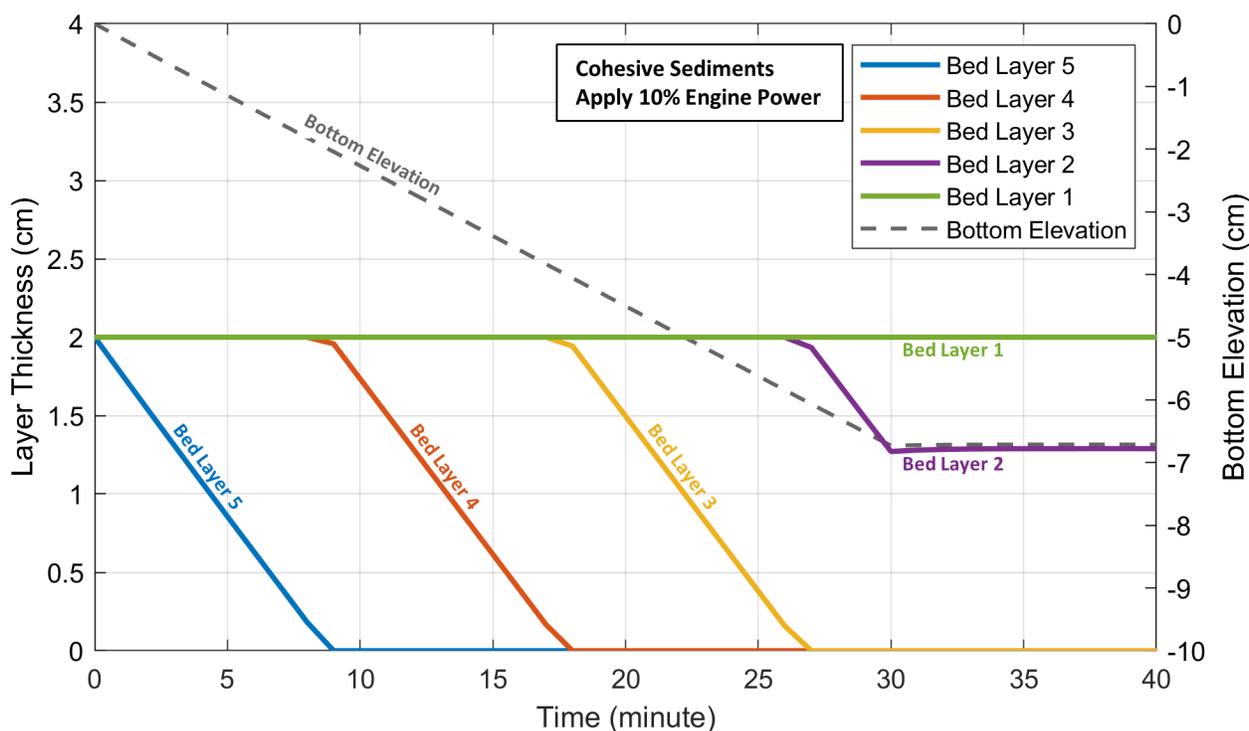
Figure 6.10: Time series of bed layer thickness at the maximum scour cell from the cohesive sediment bed simulation.

Table 6.4 compares the sediment mass in water layers and sediment bed layers between the beginning and end of the simulation. This table also presents the total mass flux of sediments exiting

the model domain through the eastern open boundary during the simulation. Overall, both fine silt and coarse silt classes showed a negligible difference between the beginning and end of the simulation (less than 0.01% of the total mass). The slight difference in the total mass occurred probably because the cumulative mass flux exiting the domain was calculated by integrating the 1-minute interval model outputs of instantaneous mass flux. Therefore, the mass comparison results suggest that the total sediment mass is conserved within the system while EFDC+ implements the propeller wash computation linked with the sediment transport processes.

As shown in Table 6.4, at the beginning of the simulation, fine silt and coarse silt materials were uniformly distributed over the five sediment bed layers, with no sediments in the water layers. At the end of the simulation, the water layers contained 3,253 kg of fine silt and 44 kg of coarse silt; these materials are the resuspended sediments that were remaining in the water column at the end of the simulation. The sediment bed layers showed more mass decrease for fine silt than for coarse silt. Moreover, 28,312 kg of fine silt left the model domain through the downstream end open boundary during the simulation, which was about four times more than the mass of coarse silt exiting the domain (7,059 kg). These results are consistent with expected sediment transport behaviors. Fine silt particles ($d_s = 16\ \mu$m) are more easily mobilized than coarse silt particles ($d_s = 50\ \mu$m). Furthermore, fine silt particles have a much lower settling velocity (typical value is 0.02 cm/s) than coarse silt particles (typical value is 0.22 cm/s), so resuspended fine silt stays suspended longer in the water column and can travel further downstream with the ambient current.

Table 6.4: Sediment mass distributions at the beginning and end of the cohesive sediment bed simulation.

	Fine Silt		Coarse Silt	
	Initial Mass (kg)	Final Mass (kg)	Initial Mass (kg)	Final Mass (kg)
Water Layers	0	3,253	0	44
Bed Layer 5 (Top)	278,250	252,541	278,250	276,634
Bed Layer 4	278,250	273,451	278,250	273,805
Bed Layer 3	278,250	277,257	278,250	277,312
Bed Layer 2	278,250	278,117	278,250	278,130
Bed Layer 1 (Bottom)	278,250	278,250	278,250	278,250
Flux Exiting Domain	0	28,312	0	7,059
Total	1,391,250	1,391,181	1,391,250	1,391,234

Through this test case, we confirmed that the EFDC+ propeller wash module can reliably simulate the resuspension processes for cohesive sediment particles based on van Rijn's theory for suspended load transport (van Rijn, 1984b).

6.3.1.2   Non-cohesive Sediments

The second demonstration model used a representative non-cohesive sediment bed condition consisting of 10% fine sand (d_s = 200 μm), 25% medium sand (d_s = 400 μm), 30% coarse sand (d_s = 800 μm), and 35% very coarse sand (d_s = 1,600 μm), with a porosity of 0.4. Like the cohesive sediment bed case, the physical and erosional properties of the non-cohesive sediment bed were set to be uniform horizontally and vertically. For the propeller wash computation, the model applied a constant engine power of 2,500 hp (50% of the maximum engine power) for the first 30 minutes of the simulation; then the propeller was turned off, allowing the suspended sediments to settle for the next 90 minutes. This demonstration model was also used for testing bedload transport processes of non-cohesive sediment particles induced by propeller wash.

Figure 6.11 displays the 2D plan view of the bottom elevations from the Original EFDC non-cohesive sediment bed simulation. This figure presents the changes in bottom elevations following the 2-hour simulation using a smoothed color map; red for net erosion areas and blue for net deposition areas. A gray marker shows the propeller location. The model results indicate that the propeller wash formed a major scour area between approximately 20 m and 50 m downstream of the propeller; the predicted maximum scour depth in this area was 1.4 cm, occurring 35 m behind the propeller. The sediments eroded by the propeller wash were redeposited to the sediment bed from just behind the major scour hole until approximately 140 m from the propeller, and the predicted maximum crest in the deposition area was about 0.6 cm.
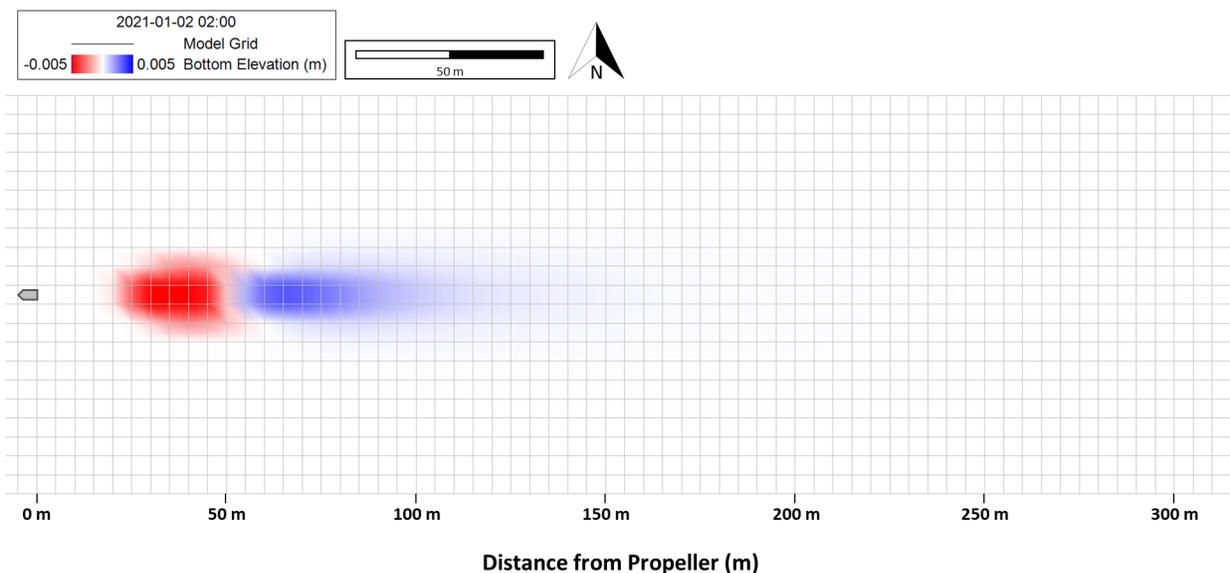
Figure 6.11: Plan view of bottom elevations simulated from a non-cohesive sediment bed model.

Figure 6.12 shows the bottom elevation profiles aligned with the propeller axis at different times (5, 10, 20, 30, and 120 minutes) during the simulation. Generally, the scour profiles from all the times considered showed a scour hole between 20 m and 50 m behind the propeller and a deposition mound further downstream of the scour hole. The scour hole size and maximum erosion depth increased with the amount of time the propeller was rotating (5, 10, 20, and 30 minutes). Unlike the cohesive sediment bed simulation, the bottom elevations at 120 minutes (end of the simulation) were almost identical to the bottom elevations at 30 minutes (i.e., the purple line overlaps the green line along their entire length). This result suggests that the non-cohesive sediments eroded by the propeller wash were transported downstream primarily as bedload (rolling or sliding along the sediment bed surface), so deposition of the resuspended sediments was not observed after the propeller stopped.

To examine the bedload effect, this study ran a model using the same conditions but deactivating the bedload computation process for the Original EFDC Sediment Transport module. In this case, the model was set up to simulate the sediment transport as suspended load only if a shear velocity was greater than the settling velocity of non-cohesive sediment particles, which requires a higher shear velocity than bedload. The bottom elevation following the 2-hour simulation without bedload is shown as a gray dashed line in Figure 6.12, and the resultant scour profile shows a negligible change in the bottom elevations (erosion less than 0.5 mm). This result indicates that the propeller wash barely caused the non-cohesive sediment bed materials to be transported as suspended load (i.e., resuspension) under this model condition.
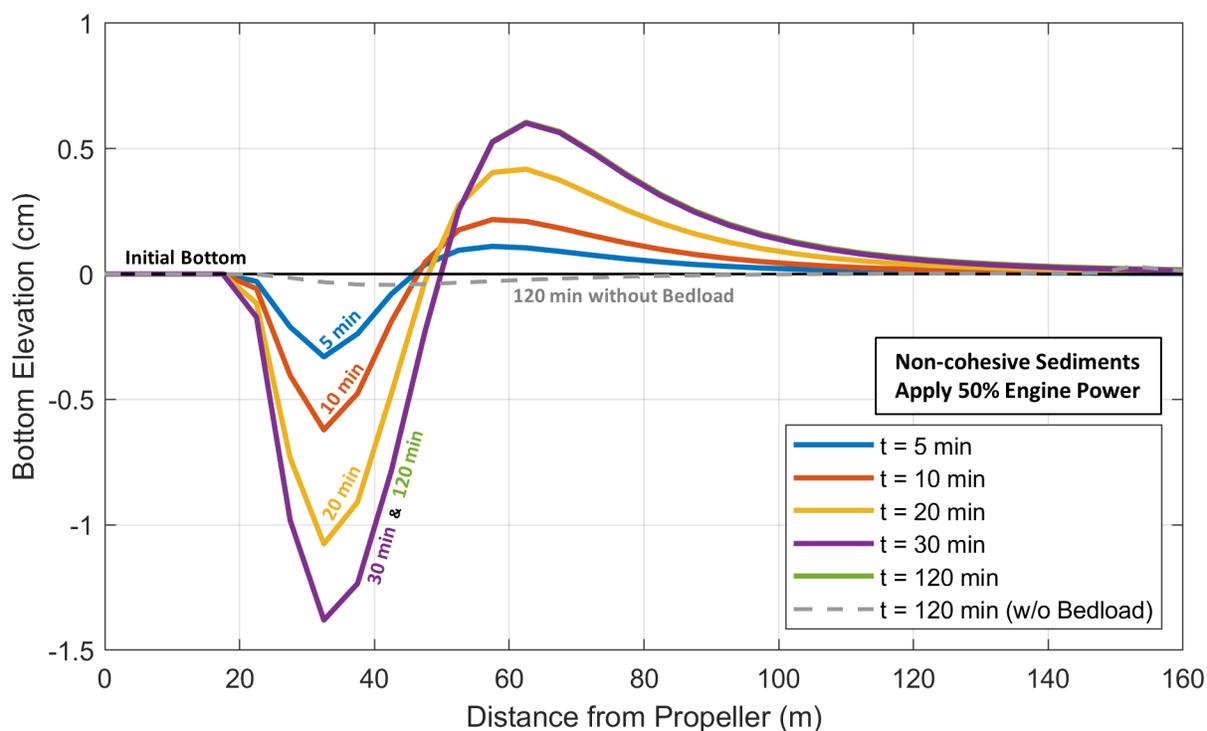
Figure 6.12: Scour profiles at different times from the non-cohesive sediment bed simulation.

This study also investigated the propeller wash-induced scour profiles by varying the applied engine powers to the propeller based on the non-cohesive sediment bed model conditions presented above. Figure 6.13 presents the bottom elevations aligned with the propeller axis following the 2-hour simulations while applying five different engine power levels: 20%, 40%, 60%, 80%, and 100% of the maximum engine power of 5,000 hp. The model results indicated that the scour hole depth increased with applied engine power, and all five simulations predicted the maximum scour location to be approximately 35 m behind the propeller. The deposition mound height also increased with applied power, and the predicted deposition crest was located farther downstream from the scour hole as the applied engine power increased. These simulated behaviors were the expected results, because an increase in applied engine power would erode more particles from the sediment bed and transport them farther downstream as bedload.
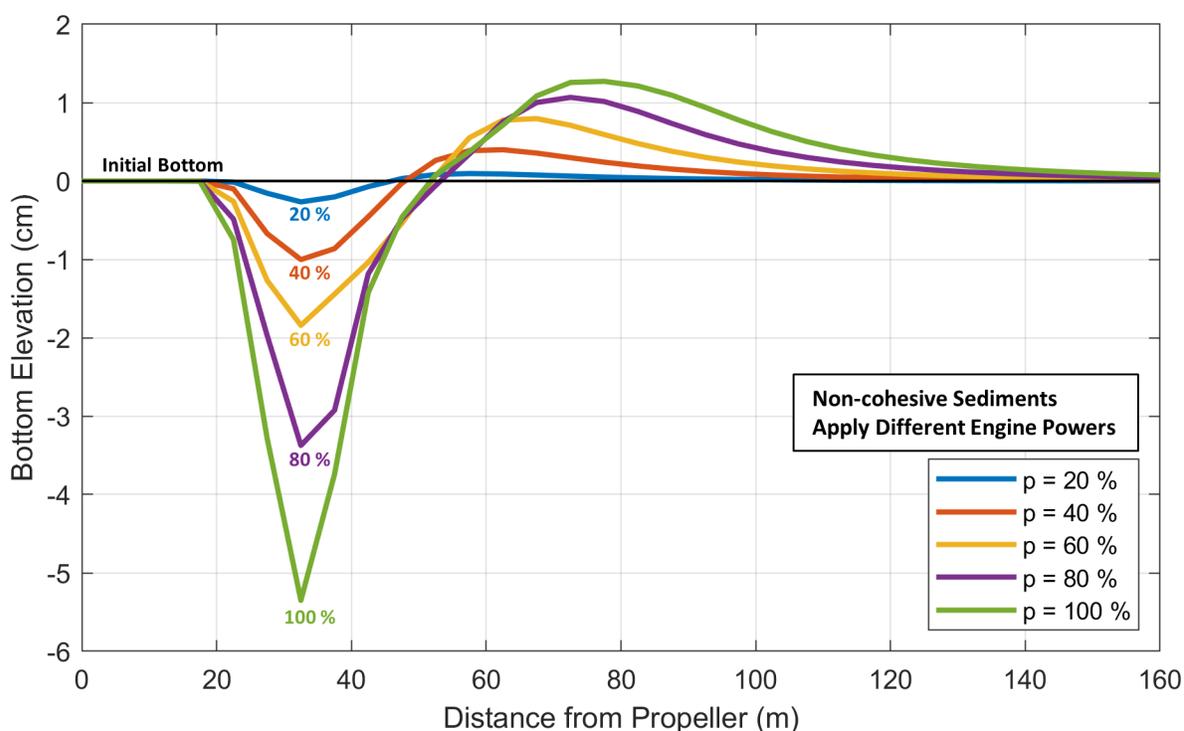
Figure 6.13: Scour profiles of non-cohesive sediment bed simulated by different engine powers.

In addition to the applied power impact analysis, this study examined the bottom elevation changes due to propeller wash by applying different particle sizes to the non-cohesive sediment bed. This test used five representative models: each model defined a sediment bed using a single particle size of $d_s = 500, 1000, 1500, 2000,$ and $2,500$ μm, which covered the size ranges of medium sand to very fine gravel. For the propeller wash simulation, the models applied a constant power of 4,000 hp (i.e., 80% of the maximum engine power) for the first 30 minutes of the simulations; then the propeller was turned off, allowing the suspended sediments to settle for the next 90 minutes. Figure 6.14 shows the bottom elevation profiles aligned with the propeller axis following the 2-hour simulations for the sediment beds with different particle sizes. All five models predicted the maximum scour area to be about 35 m downstream of the propeller, and the predicted erosion

depths were greater for the smaller particle condition, as expected. Accordingly, the deposition mound behind the scour hole had a higher crest and a longer tail downstream for the smaller sediment bed particle simulations. These results indicate that the propeller wash computation for the movements of non-cohesive sediments correctly reflected the behavior of different sediment particle sizes.
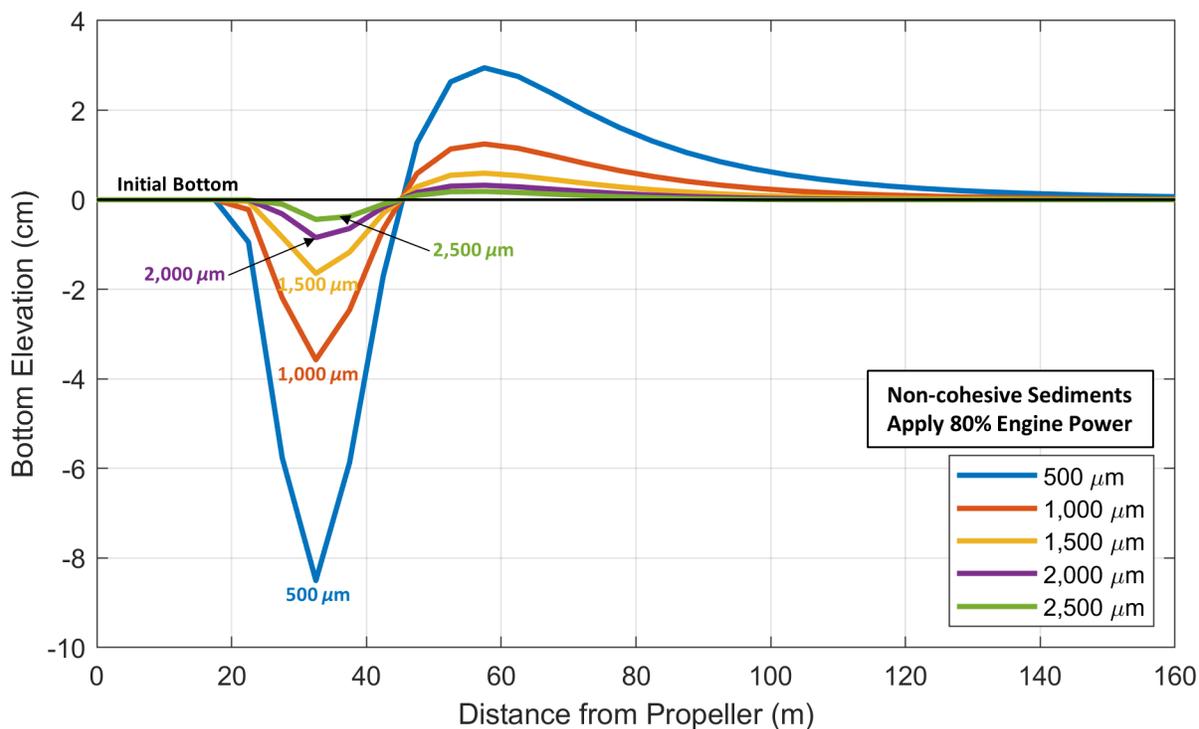
Figure 6.14: Scour profiles of non-cohesive sediment bed simulated by different particle sizes.

Through this demonstration, we show that, following van Rijn's approach (van Rijn, 1984a), the EFDC+ propeller wash module can provide a reasonable representation of propeller wash-induced scour for a non-cohesive sediment bed, including bedload transport processes.

6.3.2   SEDZLJ Sediment Transport Module

The SEDZLJ approach (Jones and Lick, 2001) uses an advanced sediment transport algorithm that accounts for spatially varied erosion properties of sediment beds. For example, a modeler can determine the erosion rates for the modeled sediment bed as a function of bed depth and applied shear stress by employing field core sample measurements (e.g., Sediment Erosion at Depth Flume [SEDFlume] data) or user-defined data. The SEDZLJ methodology can adequately represent site-specific erosion properties of sediment beds (Thanh et al., 2008). Thus, this approach has been widely used with EFDC and other multi-dimensional hydrodynamic codes for modeling sediment transport processes at contaminated sediment sites, especially with cohesive sediment beds.

This study examined the EFDC+ propeller wash module simulation linked to the SEDZLJ Sediment Transport module, focusing on how the model addresses the vertical variation of sediment bed properties. The SEDZLJ demonstration model used a cohesive sediment bed condition consisting of fine silt ($d_s = 16$ μm) and coarse silt ($d_s = 50$ μm), with a porosity of 0.8. The physical and erosional properties of the modeled sediment bed were then defined to vary vertically for this case. Specifically, for the five sediment bed layers, the fraction of fine silt decreased from the top layer (70%) to the bottom layer (30%), whereas the fraction of coarse silt increased from the top layer (30%) to the bottom layer (70%). With regard to the sediment contents and consolidation effects, higher erosion rates were assigned for upper bed layers, and lower erosion rates were assigned for lower bed layers. Thus, the demonstration model represented a typical characteristic of a cohesive sediment bed: erodibility is highest at the sediment bed surface and tends to decrease with depth. As done with the Original EFDC cohesive sediment simulation, a constant engine power of 500 hp (i.e., 10% of the maximum engine power) was applied during the first 30 minutes of the simulation; then the propeller was turned off, allowing the suspended sediments to settle for the next 90 minutes.

Figure 6.15 displays the 2D plan view of the bottom elevations following the 2-hour propeller wash simulation using the SEDZLJ Sediment Transport module. A gray marker indicates the propeller location, and the colors represent the changes in bottom elevations: red for net erosion areas and blue for net deposition areas. Overall, the SEDZLJ simulation resulted in horizontal distributions for the bottom elevation changes that were similar to those produced by the Original EFDC cohesive sediment simulation (see Figure 6.8), since the two simulations used the same particle sizes (16 μm and 50 μm). In the case of the SEDZLJ simulation, the propeller wash-induced erosion started at about 20 m downstream of the propeller, and the maximum scour of 6.2 cm was observed at 45 m behind the propeller. The erosion depth then decreased with distance and dispersed laterally until about 200 m away from the propeller. The model predicted the redeposition of the resuspended sediments outside the propeller wash-impacted erosion area, and the deposition thickness reached a maximum of 0.2 cm.

Figure 6.16 presents the scour profiles aligned with the propeller axis at different times (5, 10, 20, 30, and 120 minutes) during the SEDZLJ simulation. Overall, the simulated bottom elevations showed similar longitudinal patterns over all the times considered here. The propeller wash-induced erosion started at 20 m behind the propeller, and the scour depth increased dramatically until 45 m downstream. After the maximum scour point, the erosion depth decreased gradually with distance. The scour depth increased with the time during which the propeller was rotating (5,
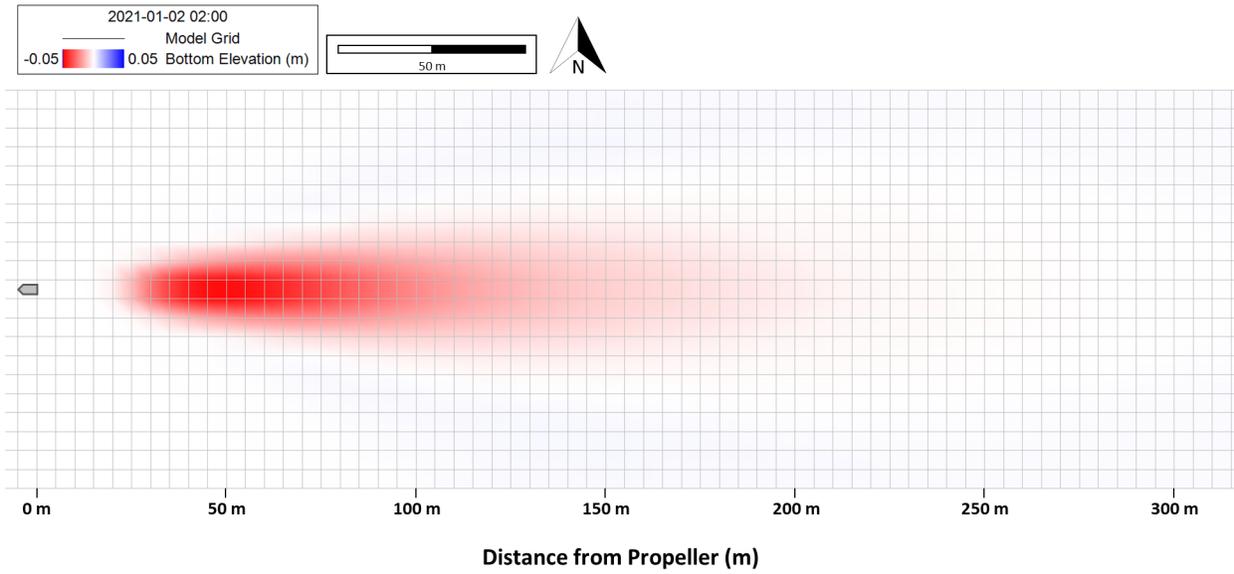
Figure 6.15: Plan view of bottom elevations simulated from a SEDZLJ sediment transport model.
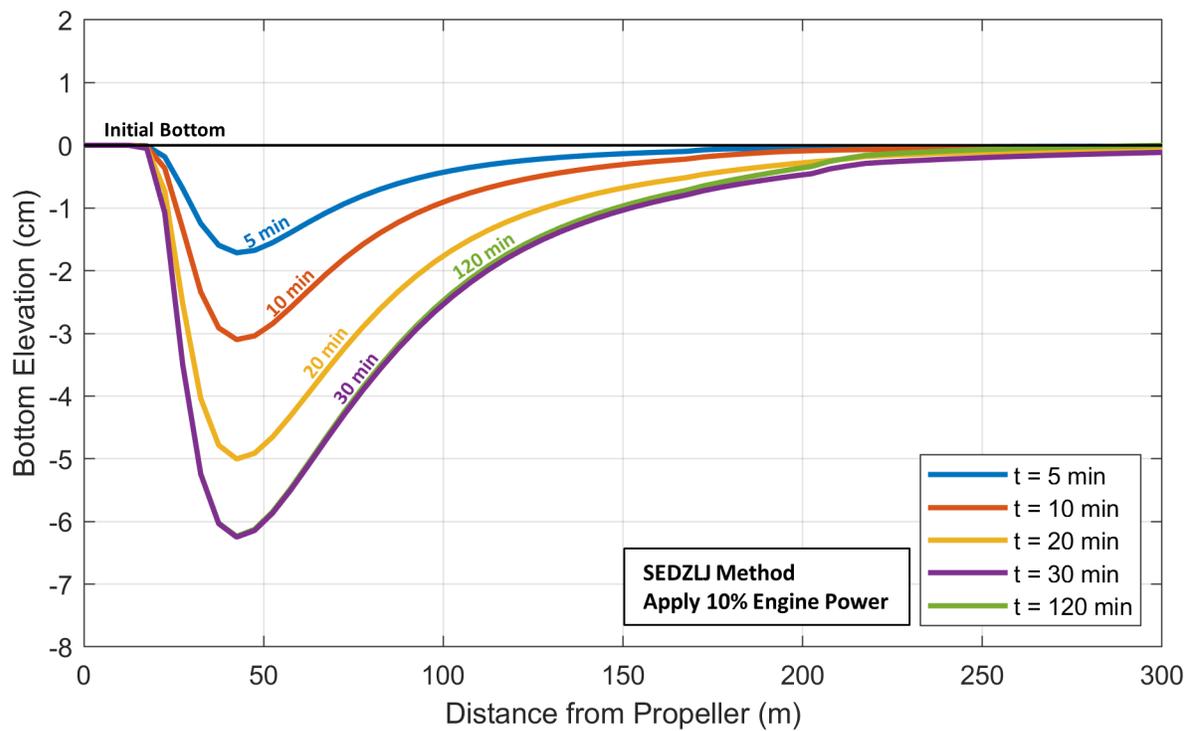
Figure 6.16: Scour profiles at different times from the SEDZLJ sediment transport simulation.

10, 20, and 30 minutes). The bottom elevations then slightly increased at the end of the simulation (120 minutes) in the area 75 m downstream and farther from the propeller, which reflected the deposition of the resuspended particles after the propeller stopped. At the location of maximum scour (6.2 cm), the SEDZLJ model predicted more erosion for the earlier period and less erosion for the later period, whereas the Original EFDC cohesive bed model provided approximately constant erosion rates over time (see Figure 6.9). Notably, at the location of maximum scour, the SEDZLJ simulation predicted a scour depth of 3.1 cm for the first 10 minutes, 1.9 cm for the next 10 minutes, and 1.2 cm for the last 10 minutes of the propeller rotating period. These results indicate that sediment erosion rates decreased as the scour hole got deeper; this behavior is consistent with the sediment bed configuration of the SEDZLJ model in which the upper bed layers were defined to have higher erosion rates than lower bed layers.

Figure 6.17 shows the changes in the sediment bed layer thickness during the SEDZLJ simulation at the maximum scour cell (45 m behind the propeller), along with the corresponding bottom elevation changes. Since the SEDZLJ approach assigns a sediment bed layer number from top to bottom, Bed Layer 1 indicates the top layer, and Bed Layer 5 represents the bottom layer of the sediment bed. The SEDZLJ approach also applies two additional layers on top of the five bed layers to compute the sediment mass exchange process between the water column and the sediment bed. The first of these additional layers is the active layer, where bedload, suspension, and deposition from the water column occur. The second additional layer is the deposition layer; it receives the deposited sediments from the active layer or provides the sediments to the active layer for bedload or suspension. While these two additional layers have a zero thickness as an initial model condition, the active layer thickness varies from about 2 to 10 times the particle sizes, and the deposition layer thickness depends on the sediment transport conditions during the simulation.

In Figure 6.17, Bed Layers 1 to 5 had a thickness of 2 cm at the beginning of the simulation. Once the propeller wash started scouring the sediment bed at this cell, Bed Layer 1 was eroded first, and the thickness of Bed Layer 2 decreased after Bed Layer 1 reached zero thickness. This scour process continued for the bed layers below for as long as the propeller wash was applied (i.e., 30 minutes). The active and deposition layers each had a thickness of less than 0.1 mm during the simulation. It should be noted that the change rates in thickness were different for each of Bed Layers 1, 2, 3, and 4, showing faster thickness decreases for the upper layers. Specifically, the thickness of Bed Layer 1 reached zero after only 6 minutes from the time this layer started to erode, whereas Bed Layer 3 took about 14 minutes to reach zero thickness. As discussed above, these results were also expected because this SEDZLJ demonstration model specified that the physical and erosional properties of the sediment bed vary vertically, having greater erosion rates in the upper bed layers than in the lower bed layers.

Table 6.5 presents the sediment mass distribution in water layers and sediment bed layers from the SEDZLJ simulation, along with the total mass flux of sediments exiting the model domain through the open boundary. Overall, these results indicate that the simulation conserved the total sediment mass for both fine silt and coarse silt classes; the total mass difference between the beginning and end of the simulation is less than 0.01% of the total. As an initial condition, the upper bed layers contained more fine silt than coarse silt, and the lower bed layers had the reverse. There were no sediments in the water, active, and deposition layers at the beginning. Following the 2-hour simulation, the water layers included 2,551 kg of fine silt and 19 kg of coarse silt; these were
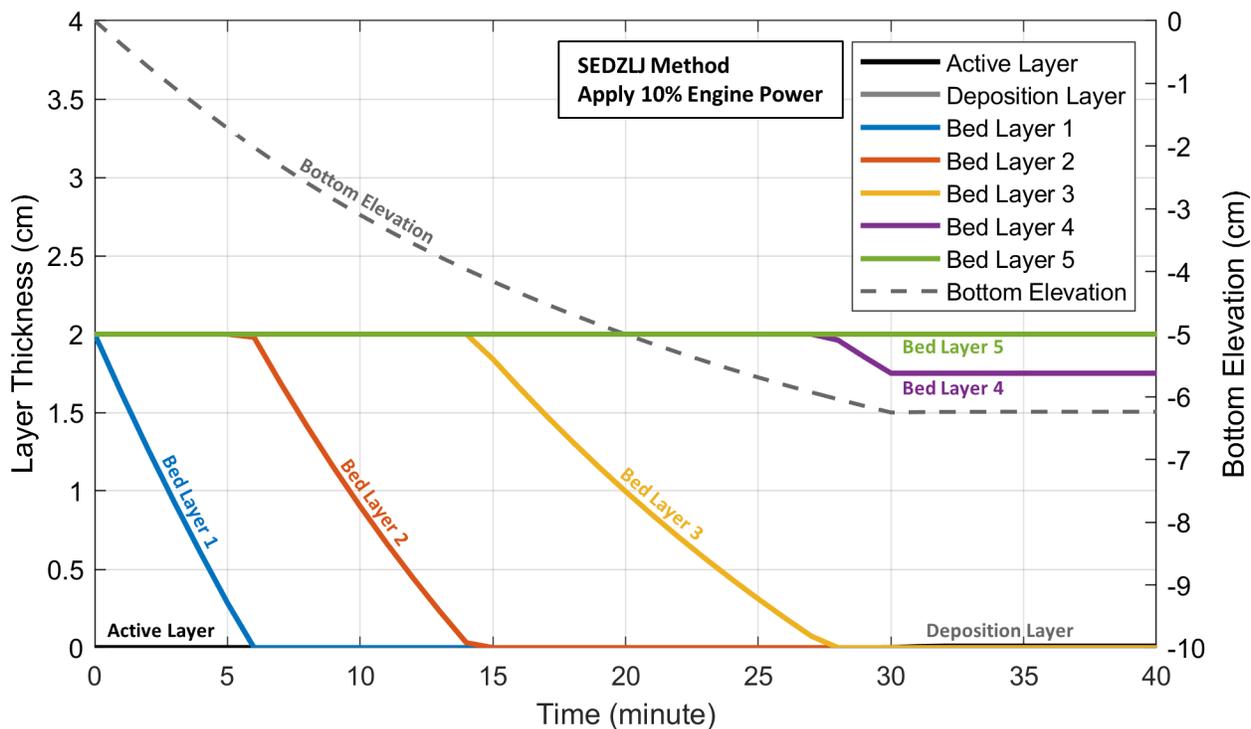
Figure 6.17: Time series of sediment bed layer thickness at the maximum scour cell from the SEDZLJ sediment transport simulation.

Table 6.5: Sediment mass distributions at the beginning and end of the SEDZLJ sediment transport simulation.

	Fine Silt		Coarse Silt	
	Initial Mass (kg)	Final Mass (kg)	Initial Mass (kg)	Final Mass (kg)
Water layers	0	2,551	0	19
Active layer (Top)	0	656	0	698
Deposition layer	0	6,703	0	10,682
Bed layer 1	389,550	358,753	166,950	158,349
Bed layer 2	333,900	329,649	222,600	219,766
Bed layer 3	278,250	277,409	278,250	277,409
Bed layer 4	222,600	222,577	333,900	333,866
Bed layer 5 (Bottom)	166,950	166,950	389,500	389,550
Flux exiting domain	0	25,889	0	867
Total	1,391,250	1,391,137	1,391,250	1,391,207

the resuspended sediments remaining in the water column. The active layer had almost the same amount of coarse silt as fine silt but these amounts were minimal. The deposition layer contained more coarse silt mass (10,682 kg) than fine silt mass (6,703 kg), since coarse silt particles were more accessible to be redeposited than fine silt particles. Additionally, about 30 times more fine silt (25,889 kg) than coarse silt (867 kg) left the model domain through the downstream end during the simulation. These results also represent the expected sediment transport behaviors regarding the sediment particle sizes, as addressed earlier with respect to the Original EFDC cohesive sediment case (Table 6.4).

The findings from this test case demonstrated that the EFDC+ propeller wash module was able to properly perform the propeller wash-induced scour and resuspension processes based on the SED-ZLJ Sediment Transport approach (Jones and Lick, 2001), accounting for the vertical variability in sediment bed properties.

6.4. Demonstration of Sediment Resuspension

This section presents a demonstration of the EFDC+ propeller wash modeling features for sediment resuspension processes induced by propeller wash from moving ships. For this analysis, two demonstration models linked to the SEDZLJ Sediment Transport module were developed. These test cases also examine the impacts of propeller momentum (see Step 12 in Chapter 3) on flow velocity field and the movement of resuspended sediments.

6.4.1 Long Straight Channel with Two Moving Ships

The first demonstration model used a synthetic, long, straight channel with two tugboats moving in opposite directions in the channel. The modeled channel had a length of 3,000 m, a width of 200 m, and a water depth of 10 m. The channel's sediment bed configuration was defined by adopting sediment data sources from other harbor areas: 31% coarse silt, 51% fine sand, and 18% coarse sand. The horizontal model grid applied a uniform cell size of 10 m $\times$ 10 m over the model domain. The vertical grid used ten layers for the water column and five layers for the sediment bed. The background ambient velocity of the water was 0.1 m/s flowing from east to west. Table 6.6 provides the characteristics of the two modeled tugboats (Tractor C-13 and Tractor C-14) moving in opposite directions.

Table 6.6: Properties of Tractor C-13 and Tractor C-14.

	Tractor C-13	Tractor C-14
Ship length	50.00 m	28.65 m
Ship beam	18.00 m	10.36 m
Ship draft	3.35 m	3.35 m
Gross tonnage	300	190
Installed engine power	5,800 hp	4,800 hp
Number of propellers	2	2
Propeller diameter	2.50 m	2.28 m
Distance from water surface to propeller	4.88 m	4.88 m
Applied revolution speed	130 rpm	120 rpm
Moving direction	East to West	West to East
Start position in x direction	2,800 m	100 m
Start position in y direction	155 m	45 m

Figures 6.18 and 6.19 present the flow velocity field and Total Suspended Sediments (TSS) concentrations in water layers (at a time snapshot) from the model simulations when excluding and including the propeller momentum, respectively. In each figure, the top panel is the 2D horizontal view of the channel, showing depth-averaged TSS concentrations (in mg/L using a color ramp) and the two ship tracks (gray marker size reflecting the ship size). The middle and bottom panels show the vertical profiles through the paths of Tractor C-13 and Tractor C-14, respectively. The

color ramp represents the TSS concentrations and the vector arrows indicate the magnitude and direction of the flow velocity.

In Figure 6.18, the top panel shows that the model simulated the depth-averaged TSS concentrations to be increasing behind the two ships as they traveled through the water. The simulated TSS concentrations behind the larger ship (Tractor C-13) were greater than the smaller ship (Tractor C-14). In the two bottom panels, the vertical profiles show the sediment resuspension caused by the ship movement, which increased the TSS concentrations in water column. The propeller wash-induced TSS concentrations were higher at the bottom than at the water surface, and they were also greater for the larger ship than the smaller ship. As the ships proceeded, the resuspended sediments in the path traveled behind the ships were redeposited to the sediment bed, causing a TSS concentration reduction in the water column. In this case, the velocity vectors represent only the ambient currents because the model computed the hydrodynamic flow field not including the propeller efflux momentum.

Figure 6.19 demonstrates that the model results for both TSS concentration and velocity distributions differ significantly depending on whether the simulation added the propeller momentum to the flow field or not. In the top panel, the TSS concentrations dispersed more in both longitudinal and lateral directions, compared to Figure 6.18. In the two bottom panels, the vertical profiles show that the velocity vectors near the ships reflect the change in water flow direction due to propeller movement. The highest velocities occurred at approximately at 5 m depth, which corresponds to the distance from the water surface to the propeller (4.88 m). They also show that the magnitude of the velocity vectors near the larger ship were greater than those near the smaller ship. The resultant flow velocities notably affect the movement of the resuspended sediments (e.g., advection, dispersion, and diffusion). Specifically, the model simulated the TSS concentrations spreading much more in both longitudinal and vertical directions compared to the plan view and vertical profiles in Figure 6.18. The water velocities behind each ship stabilized after a few hundred meters; consequently, the TSS concentrations decreased with distance. Nevertheless, the TSS concentrations simulated at locations far behind the ship were quite high near the water surface in this case. These model results demonstrate that the EFDC+ propeller wash module can predict the sediment resuspension and subsequent transport processes associated with propeller wash-induced currents.

EFDC+ Propeller Wash Module
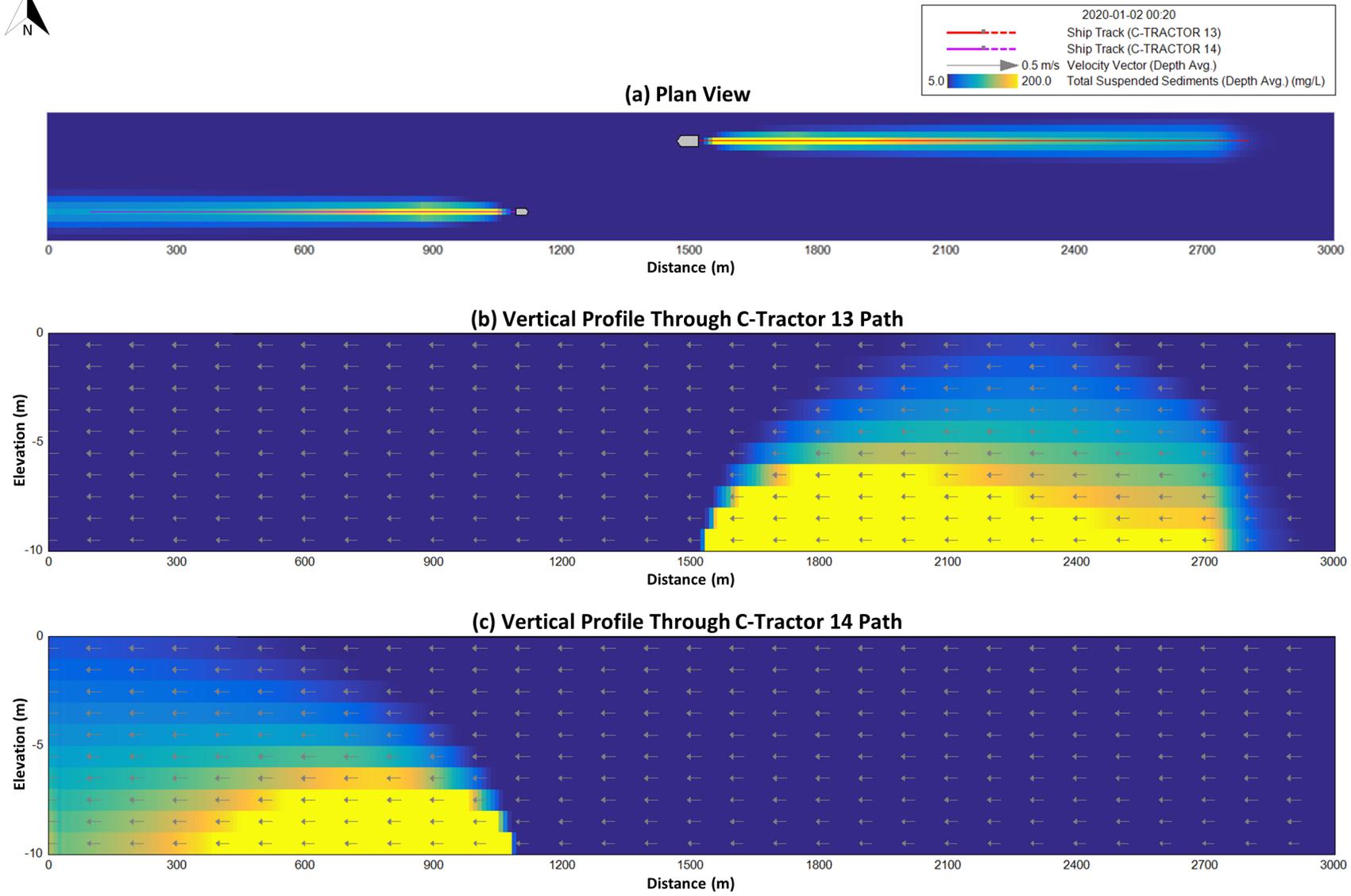
Figure 6.18: TSS concentrations and velocity field from a straight channel simulation without propeller momentum effects.
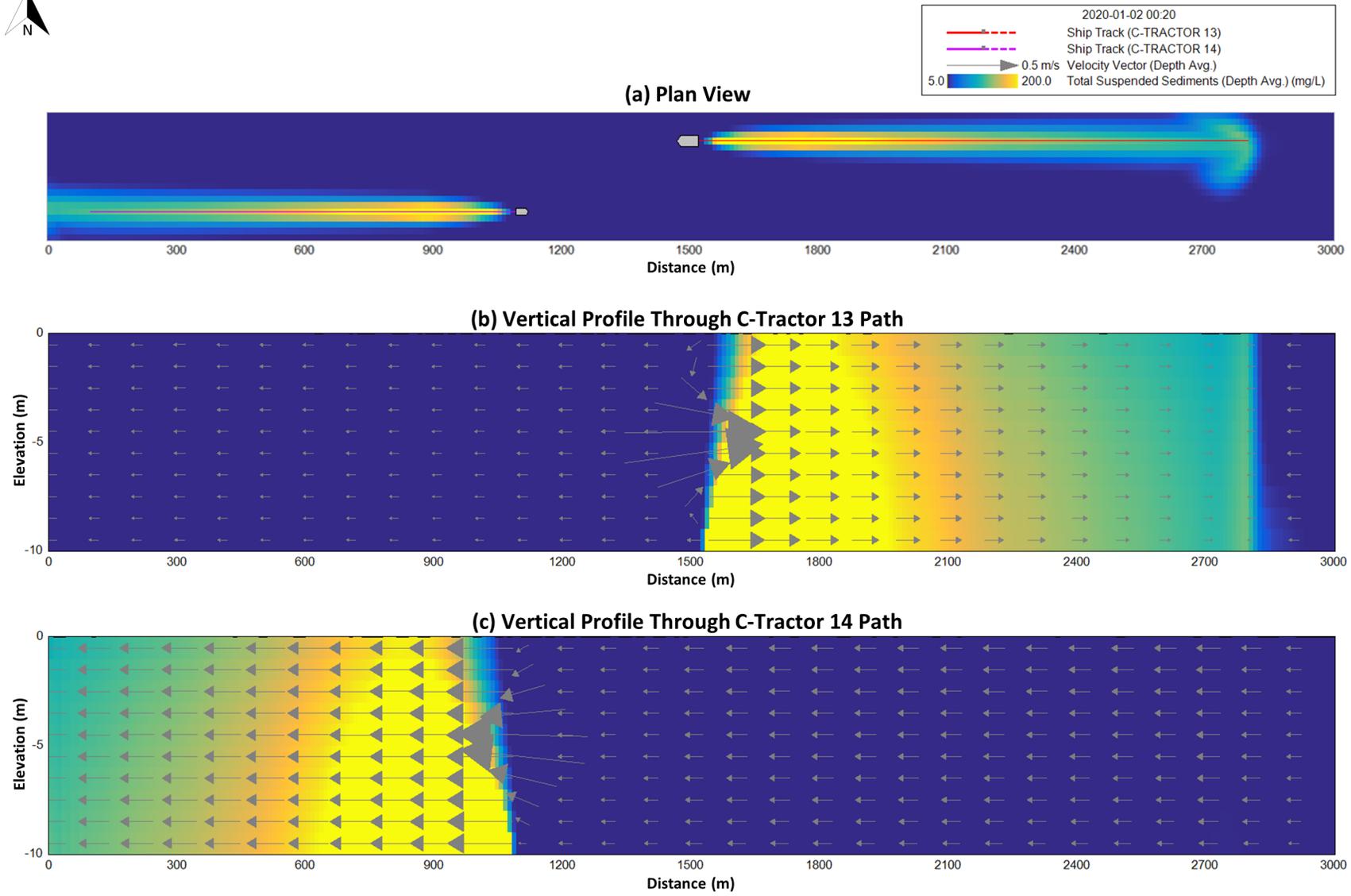
Figure 6.19: TSS concentrations and velocity field from a straight channel simulation including propeller momentum effects.

6.4.2   San Diego Bay Tugboat Test Site

The second demonstration model was developed based on the San Diego Bay tugboat model used for the validation of near-bed velocity, bottom shear stress, and erosion depth (see Section 6.2). The specified model domain, bathymetry, hydrodynamic conditions, sediment bed configurations, and tugboat characteristics were the same as described in Section 6.2. However, for the propeller wash simulation, this demonstration evaluated tugboat Tractor C-14 operating on an approximately circular path around the model domain at 105 rpm for two hours (12:00 to 14:00 PDT on July 19th, 2012).

Figures 6.20 presents the model results for the velocity field and TSS concentrations at 13:52 (near the end of the simulation), comparing two situations: when the model excluded (left panel) vs. included (right panel) the propeller momentum effects for the hydrodynamic flow field computation. In each panel, a black line shows the ship path during the two-hour simulation. Gray vector arrows represent the magnitude and direction of the depth-averaged flow velocity, and a color ramp displays the depth-averaged TSS concentrations (in mg/L).

In Figure 6.20, both velocity distributions and TSS concentrations were significantly different between the two simulations. When the model ignored the propeller momentum effects (left panel), the flow velocities were negligible, since the flow field only represented the background tidal currents, and the TSS concentrations of the resuspended sediments were distributed along the ship's path. As the resuspended sediments in the path behind the tugboat were redeposited to the sediment bed, the TSS concentrations in the water column decreased over time. On the other hand, when the propeller momentum effects were simulated (right panel), the model predicted high-velocity magnitudes behind the tugboat, reflecting the flow direction due to the propeller movement. Consequently, the resuspended sediments were transported more actively, presenting more mixing and dispersion of the TSS concentrations behind the tugboat. Additionally, this simulation shows eddies at the southeast and north sides of the model domain (manifested as higher TSS concentrations), where the areas were restricted by the bank and pier structures. Moreover, the TSS concentration distributions indicate that the simulated eddies also notably influenced the movement of the resuspended sediments. These results would also support the EFDC+ propeller wash module's ability to predict the process of the propeller wash-induced currents conveying the resuspended sediments further, which might represent a meaningful sediment load to adjacent areas.
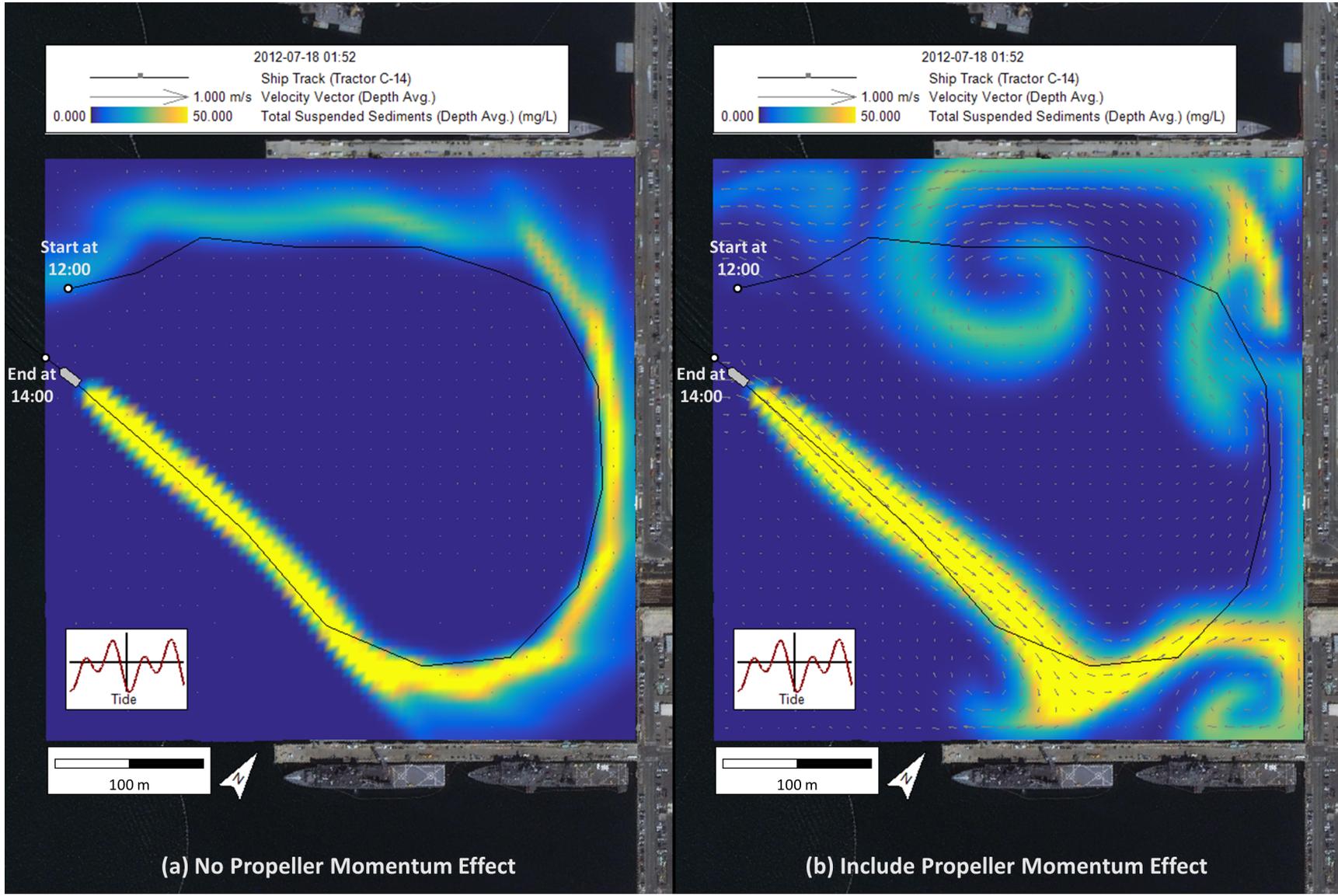
Figure 6.20: TSS concentrations and velocity field from San Diego Bay tugboat simulations without vs. with propeller momentum.

6.5. Application to Kingston Ferry Terminal

This case study presents the application of the EFDC+ model to estimate the impacts of propeller wash on scour around the docking facilities of a ferry terminal in Kingston, WA. For this study, DSI received propeller wash data from the Washington State Department of Transportation (WSDOT) and the University of Washington (UW) Applied Physics Lab, which were collected at the Kingston ferry terminal as reported in Kastner et al. (2019). The field data include ADV measurements for near-bed flow velocity, historical bottom elevation records at piling structures, and detailed specifications for three Kingston ferries. Additionally, through a conference call with a captain of Washington State Ferries (WSF), DSI obtained information on how the engines and propellers are operated while the ferries are arriving and departing at the terminal. This section provides the background of the Kingston ferry terminal propeller wash studies, model configuration, and a discussion of the model results.

6.5.1 Background

The Kingston ferry terminal has three slips, which are docking facilities that can receive and launch ferry ships, as shown in Figure 6.21. WSDOT has monitored the bottom elevations around the structural pilings annually, observing severe seabed scour at Slip 1 in recent years. Specifically, a subsurface bench in the sediment bed near Slip 1 has eroded shoreward and migrated through the bridge seat toward the onshore structures, causing concern for terminal safety. Kingston ferry terminal Slip 1 is actively used for the Kingston-Edmonds ferry route across Puget Sound, operating a total of 46 trips between Kingston and Edmonds every day using three ferries: Motor Vessel (M/V) Puyallup, M/V Spokane, and M/V Walla Walla.

Figure 6.21 shows the AIS-tracked ship paths of these three ferries on March 18, 2018, indicating that a majority of the ferry traffic occurred in Slip 1. Table 6.7 presents the characteristics of the three ferries. M/V Puyallup can carry a maximum of 2,499 passengers and 202 vehicles with 16,000 hp engine power. Both M/V Spokane and M/V Walla Walla, which are smaller than M/V Puyallup, have a maximum capacity of 2,000 passengers and 188 vehicles with 11,500 hp engine power. These ferries are double-ended with symmetric propulsion systems, as shown in Figure 6.22, allowing the ferries to arrive and depart at the terminal without changing orientation. Propeller wash from the ferries directly impacts the slip, since the slip-facing propeller is active for braking on arrivals and propulsion on departures (Kastner et al., 2019).

As part of efforts to mitigate erosion at this site, Kastner et al. (2019) conducted a field study to investigate the influence of ferry traffic on the severe erosion at the Kingston ferry terminal. They deployed two ADVs on the base of the north and south bridge seat pilings at Slip 1 from March 15 to March 28, 2018, to measure the flow velocities close to the seabed, as shown in Figure 6.21. The deployment elevation was -9.8 m for the north piling and -5.9 m for the south piling (MLLW vertical datum), which were dependent on the seabed bottom elevation at each location. During the measurement period (March 15-28, 2018), the ADVs collected the velocity data in 512-second bursts followed by 208 seconds of no collection, for a total cycle of 12 minutes at a frequency of 16 Hz. The survey found that the peak flow velocities observed during the ferry
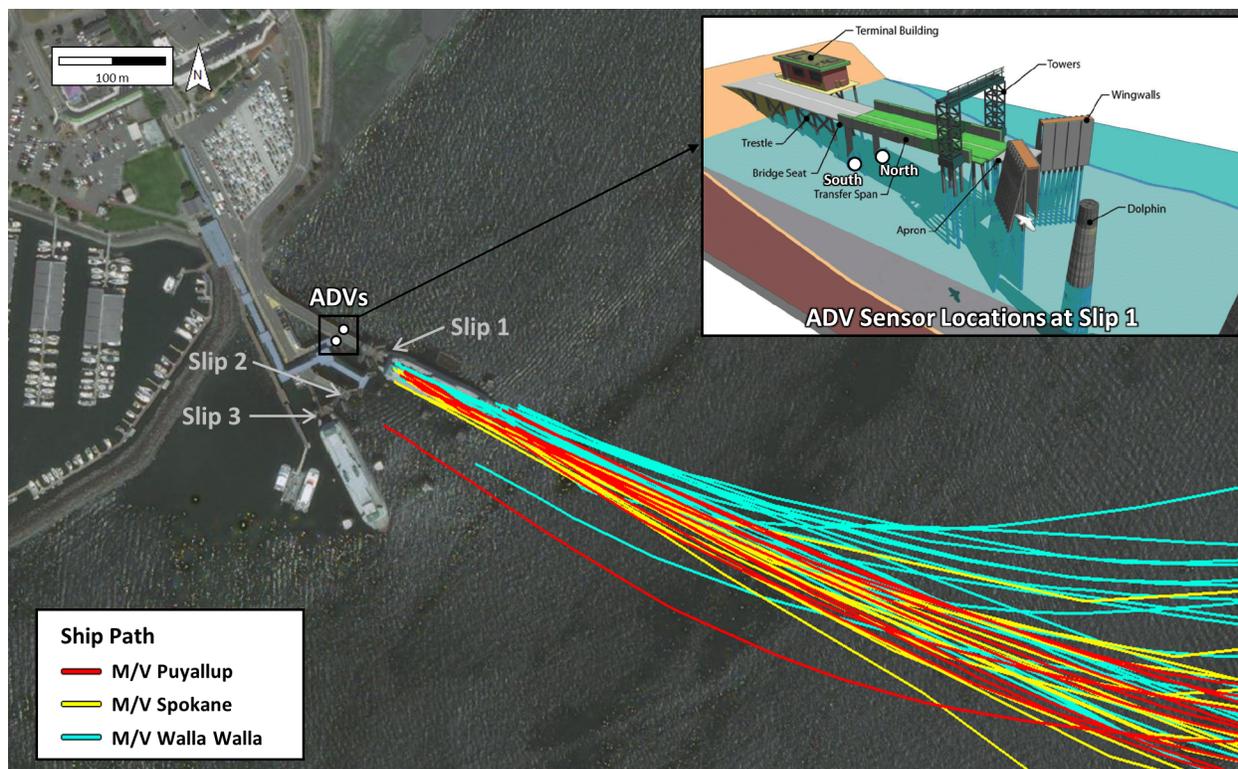
Figure 6.21: Aerial image of Kingston ferry terminal, AIS-tracked ship paths for three ferries on March 18, 2018, with ADV sensor location diagram (after Kastner et al., 2019).

Table 6.7: Ship and propeller characteristics of three ferries on the Kingston-Edmonds route.

Ship Name	M/V Puyallup	M/V Spokane M/V Walla Walla
Class	Jumbo Mark II	Jumbo
Passenger Capacity	2,499	2,000
Vehicle Capacity	202	188
Ship length	140 m	134 m
Ship beam	28 m	26 m
Ship draft	5.6 m	5.5 m
Service speed	18 knots	18 knots
Installed engine power	16,000 hp	11,500 hp
Maximum propeller speed	210 rpm	180 rpm
Propeller diameter	3.962 m	3.962 m
Number of blades	5	4
Blade area ratio	0.75	0.6
Pitch ratio	0.96	1.05
Distance from ship stern to propeller	7.0 m	6.7 m
Distance from ship stern to AIS antenna	114.5 m	110.0 m
Distance from ship bottom to propeller axis	-2.2 m	-2.0 m
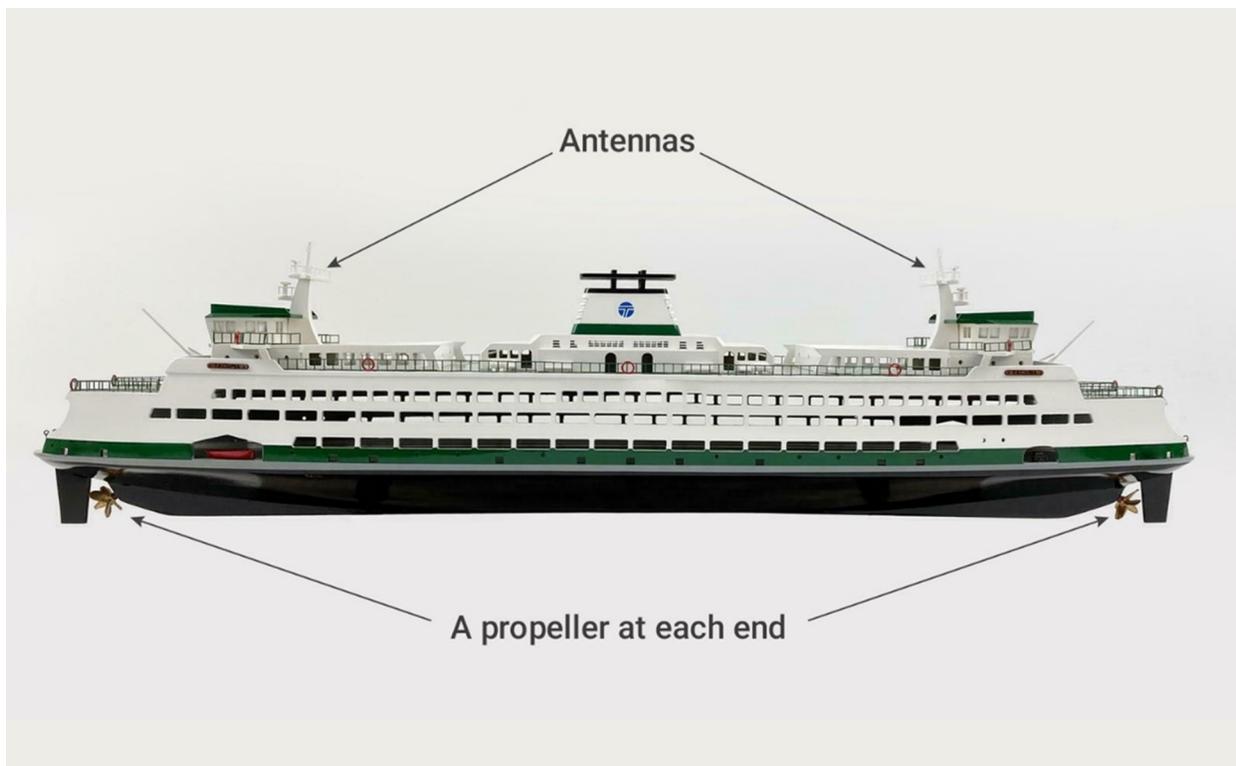
Figure 6.22: Side view of M/V Puyallup.

departures were 30 to 50 times greater than the flow velocities under quiescent conditions. Using the ADV-measured velocity data, Kastner et al. (2019) also calculated the Reynolds shear stress (Chou, 1945), which addresses longitudinal and lateral velocity fluctuations by assuming that the turbulence is isotropic and the flow is steady. The bottom shear stresses during ferry arrivals and departures were estimated to be 10 to 100 times greater than during the quiescent periods. The estimated bottom shear stresses were higher during departures than during arrivals, which might be due to higher propeller speeds when accelerating the ferries for departures. Moreover, lower tidal stages corresponded to higher bottom shear stresses because the ferries' propeller was closer to the seabed when the water level was low. Accordingly, the shallower seabed location (-5.9 m depth at the south piling) was also exposed to higher shear stress than the deeper seabed location (-9.8 m depth at the north piling).

6.5.2   Model Development

In this study, DSI developed a propeller wash model for the Kingston ferry terminal area to demonstrate the propeller wash effects of the ferry traffic on the seabed at Slip 1. Figure 6.23 presents the model grid cells, bottom elevations, ADV locations, and a ferry moored at Slip 1 as an example. The model domain covered about 2.6 km^2 using a telescoping horizontal grid with 34,456 cells, applying the smallest cell dimension of 4 m $\times$ 4 m to the ferry terminal area and increasing the cell sizes at the outer extents. The vertical grid used five layers for the water column. The model bottom elevations were specified by combining the publicly available datasets: Digital Elevation

Model (DEM) data from January 2005 for the entire model domain (Finlayson, 2005) and bottom elevation records at structure pilings in 2018 for the terminal areas (Kastner et al., 2019). The bottom elevations over the entire model domain ranged from -81.21 m to 12.97 m, and the bottom elevations varied between -13.06 m and -0.10 m around the Kingston ferry terminal, based on the MLLW vertical datum.
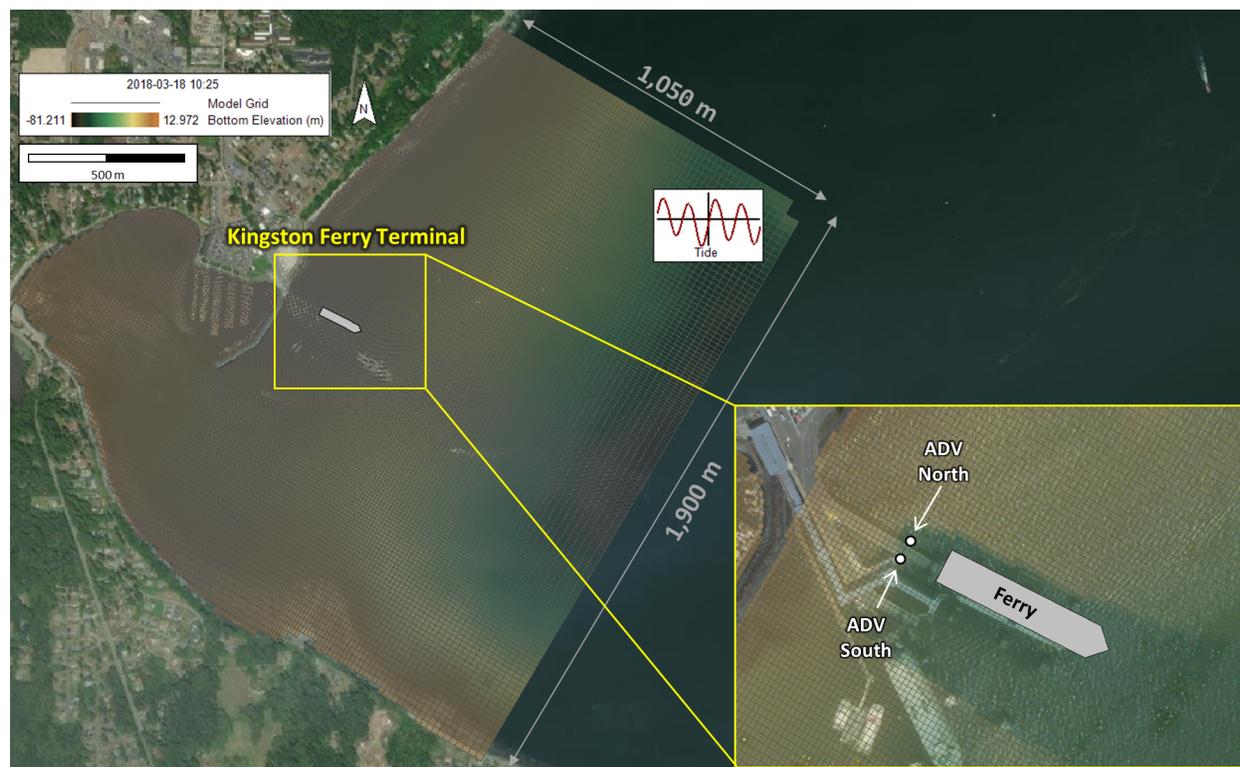
Figure 6.23: Model conditions for the Kingston ferry terminal case.

The study selected the period from 06:00 to 24:00 PDT on March 18th, 2018, for the model simulation because all three ferries were actively running during this period and because ADV-measurements were available. For the hydrodynamic conditions, the model specified a higher bottom roughness for nearshore areas and applied a time series of tide data to the eastern and northern open boundary cells facing the ocean. Because no sediment data were available to define the physical or erosion properties of the seabed in the terminal area, the model did not simulate the sediment transport processes for this demonstration. This study compared the simulated bottom shear stress to critical shear stress by sediment size classification to predict the approximate conditions for seabed scour due to propeller wash.

For the propeller wash module, the model defined the three ferries and their propellers based on Table 6.7. The sub-grid configuration for each ferry was determined as 1,200 m in length and 400 m in width, including 300 points in the longitudinal dimension and 100 points in the lateral dimension. In addition, the model was set to incorporate the propeller momentum effects into the hydrodynamic flow field computation (see "ISPROPWASH" = 2 in Section 4.1). The model simulated 22 departure trips of the three ferries; the ship paths were specified using the AIS tracking data for the simulation period. The arrival trips were not simulated because the EFDC+ propeller

wash module does not perform the propeller wash computation for the braking operation on arrivals. As a reminder, previous measurements indicated higher shear stress for departures than for arrivals because of the higher propeller speeds for ferry propulsion. Per the WSF port captain, the ferries are usually operated with about 10 to 20% of total engine power when they are departing the terminal. Based on this information, the model used the applied power for the departure moments of the three ferries as 20% of their installed engine power. The model then gradually increased the applied power as the ferries got farther away from the terminal, up to 75% of the engine power for sailing at service speed (see Section 4.5.3).

6.5.3   Model Results and Discussion

To begin with, the study compared the model results for propeller wash velocities at sub-grid points at the ADV locations to the ADV-measured velocities at those locations. Both the sub-grid-based model results and the ADV data represented the propeller wash-induced velocities at the water-sediment interface. Figure 6.24 shows the simulated near-bed flow velocity for sub-grid points behind M/V Walla Walla at 10:26 PDT on March 18th, 2018, when M/V Walla Walla was departing the Kingston ferry terminal. The sub-grid points indicate the propeller wash velocity magnitude with a color ramp. The ADV locations at the north and south pilings of Slip 1 are also displayed in this figure. The highest propeller wash velocity at the seabed appeared at approximately 80 m behind the ferry from this departure event in this figure. As the ferry moved forward, the sub-grid mesh also migrated, attaching behind the ferry for the subsequent propeller wash computation. Accordingly, this study collected the propeller wash velocities computed from the three ferries' sub-grid points that passed the north and south ADV locations during the simulation (06:00 to 24:00 PDT on March 18th, 2018) and compared them to the ADV-measured velocities.

Figure 6.25 compares the ADV data and EFDC+ model results for near-bed propeller wash velocity at the south piling (-5.9 m depth) of Slip 1 associated with the 22 ferry departures on March 18th, 2018. In this figure, red dots indicate the ADV-measured flow velocities with 12-second low-pass filtering, and blue dots represents the sub-grid-based simulation results from the traffic of the three ferries. Overall, the model reasonably reproduced the ADV-observed velocities due to the ferries' departure, since a strong correspondence is apparent in the timing of the velocity spikes between the data and model results. The difference in the peak velocity magnitude between the data and model results might be due to uncertainties from various sources. For example, the ADVs collected the velocity data in 512-second bursts followed by 208 seconds of no collection for a total cycle of 12 minutes, so the instruments might have failed to observe the peak magnitude if a ferry departure happened during the no ADV sampling period (208 seconds). The AIS data precision with respect to path and heading might cause uncertainty in the ferry positions, affecting the simulation results. Additionally, this study specified the applied power for the departure moments as 20% of the installed engine power of the three ferries, but the actual applied power could vary depending on weather conditions or the operators' discretion (i.e., there is no standard procedure for embarking and disembarking, per the WSF port captain).

This study also analyzes the model results for the hydrodynamic flow field with the propeller momentum effects. Figure 6.26 displays the simulated depth-averaged flow velocities at 10:28 PDT on March 18th, 2018, two minutes after M/V Walla Walla departed from the terminal. A
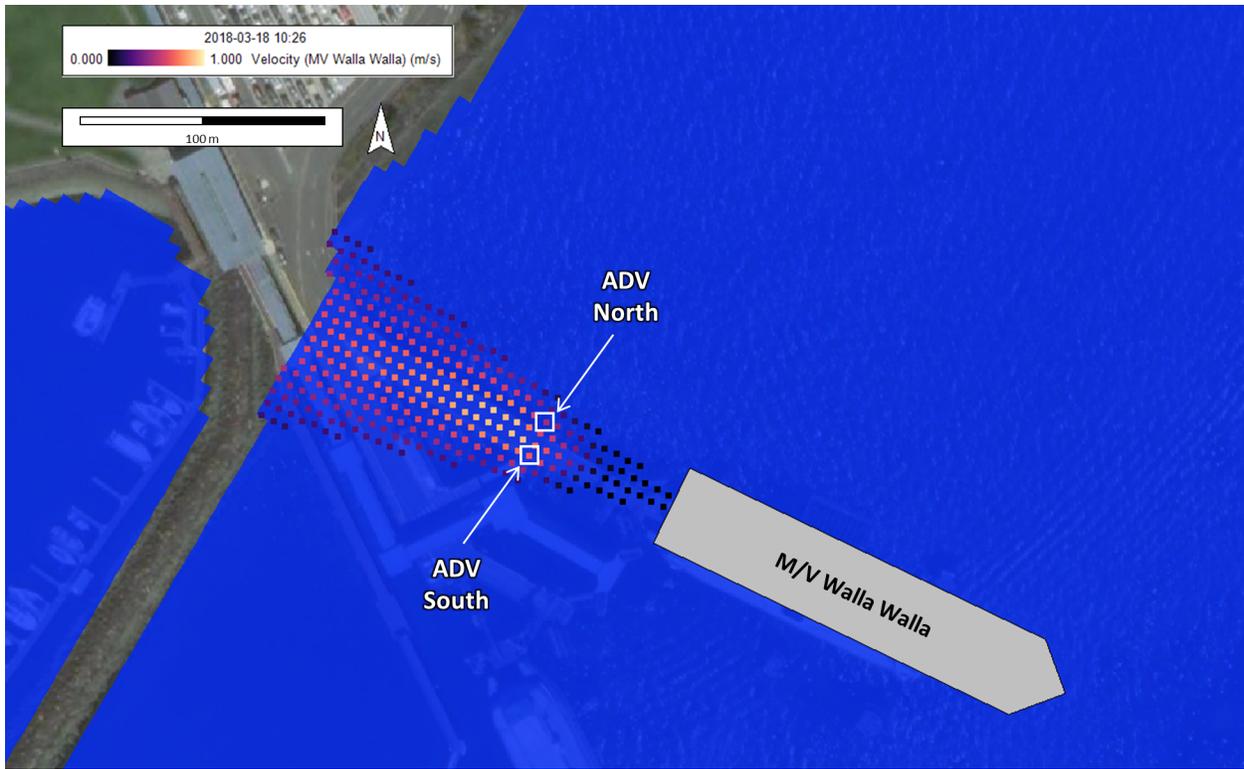
Figure 6.24: Near-bed flow velocity due to M/V Walla Walla at 10:26 PDT on March 18th, 2018.
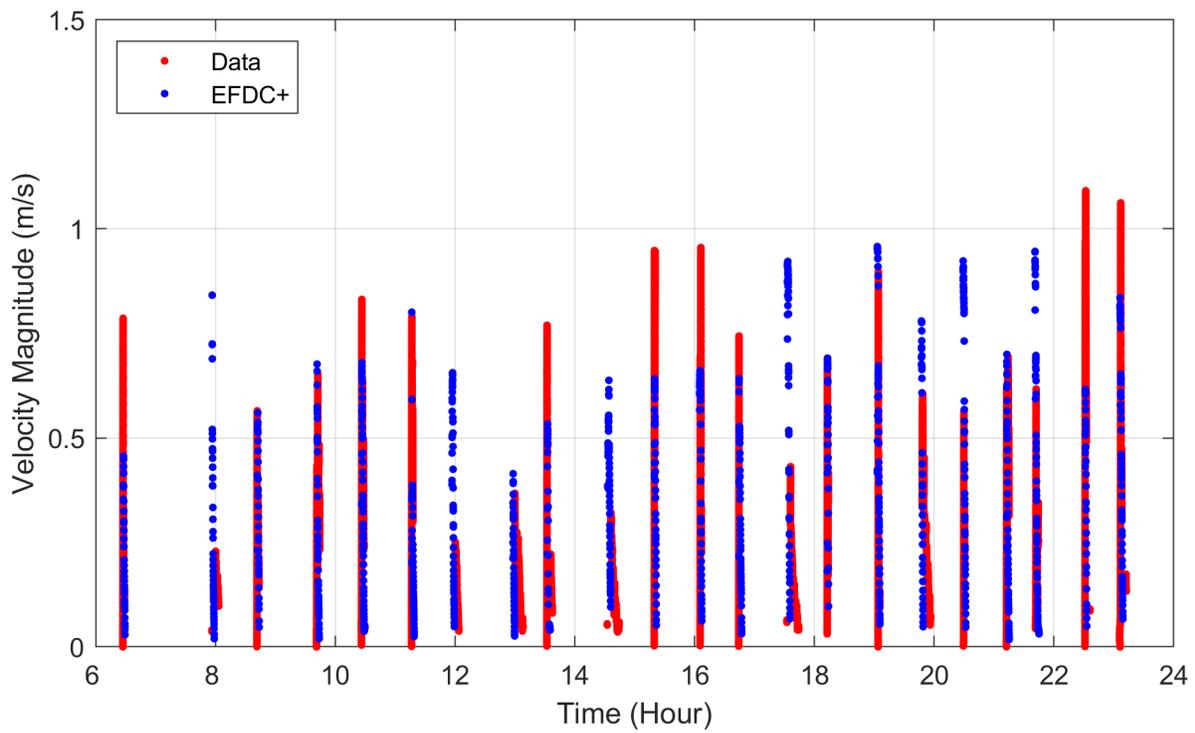
Figure 6.25: ADV data and EFDC+ model results for near-bed flow velocity at the south piling.
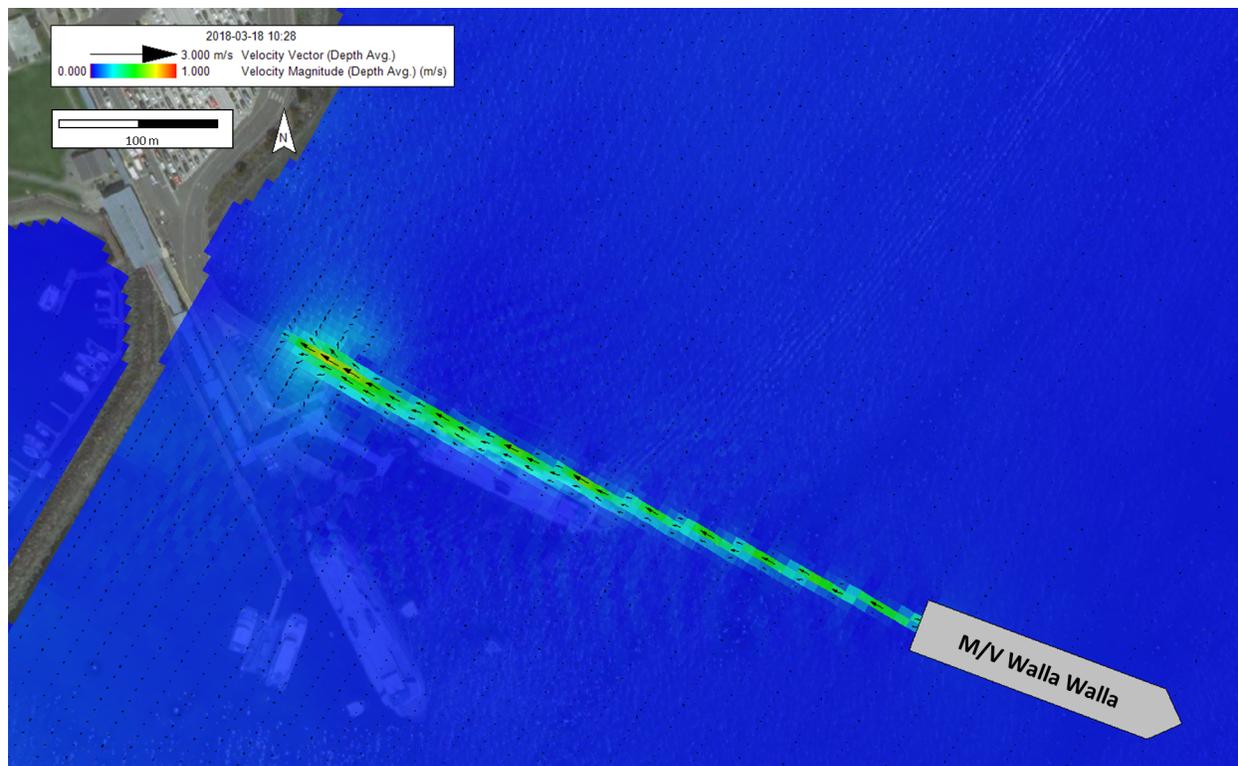
Figure 6.26: Simulated depth-averaged flow velocity field due to departure of M/V Walla Walla at 10:28 PDT on March 18th, 2018.

color ramp indicates the magnitude of the depth-averaged flow velocity at each model grid cell, and the black vector arrows indicate the magnitude and direction of the flow velocities for the model grid cells. Figure 6.26 shows the high-velocity jet behind the ferry as the simulation incorporated the impacts of the propeller momentum into the 3D flow velocity field. The high flow velocities induced by the propeller momentum remained in the terminal area even after the ferry had traveled far away from the terminal. The remaining propeller-induced velocities dispersed with time and dissipated when the jet reached the nearshore areas.

The study then evaluates the propeller wash effects on seabed scour by investigating the model results for bottom shear stresses caused by the ferry propeller wash at the ADV locations. Figure 6.27 shows the sub-grid-based bottom shear stress (N/m^2) simulated at the north and south pilings of Slip 1, along with the tide data. To generate this figure, the propeller wash shear stress computed from the three ferries' sub-grid points that passed the north and south ADV locations during the simulation were collected. Overall, the shear stresses estimated at the south piling (-5.9 m depth) were generally greater than the shear stresses at the north piling (-9.8 m depth). The peak bottom shear stresses were predicted to reach 1.79 N/m^2 at the south piling and 1.12 N/m^2 at the north piling. The simulated bottom shear stresses were also higher for lower tidal stages than higher tidal stages because the ferries' propeller was closer to the seabed. These model results are consistent with the observations from Kastner et al. (2019).

Figure 6.27 also includes horizontal dashed lines to indicate the critical shear stress (in N/m^2) for each sediment size classification, labeled on the left axis. The critical shear stress is the shear stress

required to mobilize the sediments, and it is determined as a function of the sediment particle size and specific gravity. According to Julien (2002), fine sediments (clay + silt) can be mobilized even if the shear stress is less than 0.11 N/m^2, while shear stress greater than 0.11 N/m^2 can scour the sand-sized sediments. Shear stress greater than 1.26 N/m^2 is required to erode gravel-sized sediments. Overall, the model results indicated that all ferry departures induce shear stress greater than 0.11 N/m^2 for both the north and south pilings, which can cause severe scour in a sand bed. The model predicted shear stresses exceeding 1.26 N/m^2 (up to 1.79 N/m^2) at the south piling of Slip 1 due to several ferry departures during the low tide period. Such high shear stress is expected to cause significant erosion even in a gravel bed. It should also be noted that the critical shear stress for each sediment size class (Julien, 2002) was developed by assuming a flat sediment bed, so the sediments in this area would likely be even more easily eroded because of the bench face slope at Slip 1 (Kastner et al., 2019).

In conclusion, the findings from this analysis suggest that the propeller wash from ferry departures has a significant impact on the seabed scour around the structural pilings of Slip 1 in the Kingston ferry terminal. Furthermore, this case study demonstrated the functionality and capabilities of the EFDC+ propeller wash module as an effective tool for evaluating scour issues. Based on these findings, it can be concluded that the EFDC+ propeller wash modeling approach will be beneficial for researchers, engineers, and regulators in their efforts to properly evaluate propeller wash effects for contaminant remediation planning, scour mitigation, and structure design.
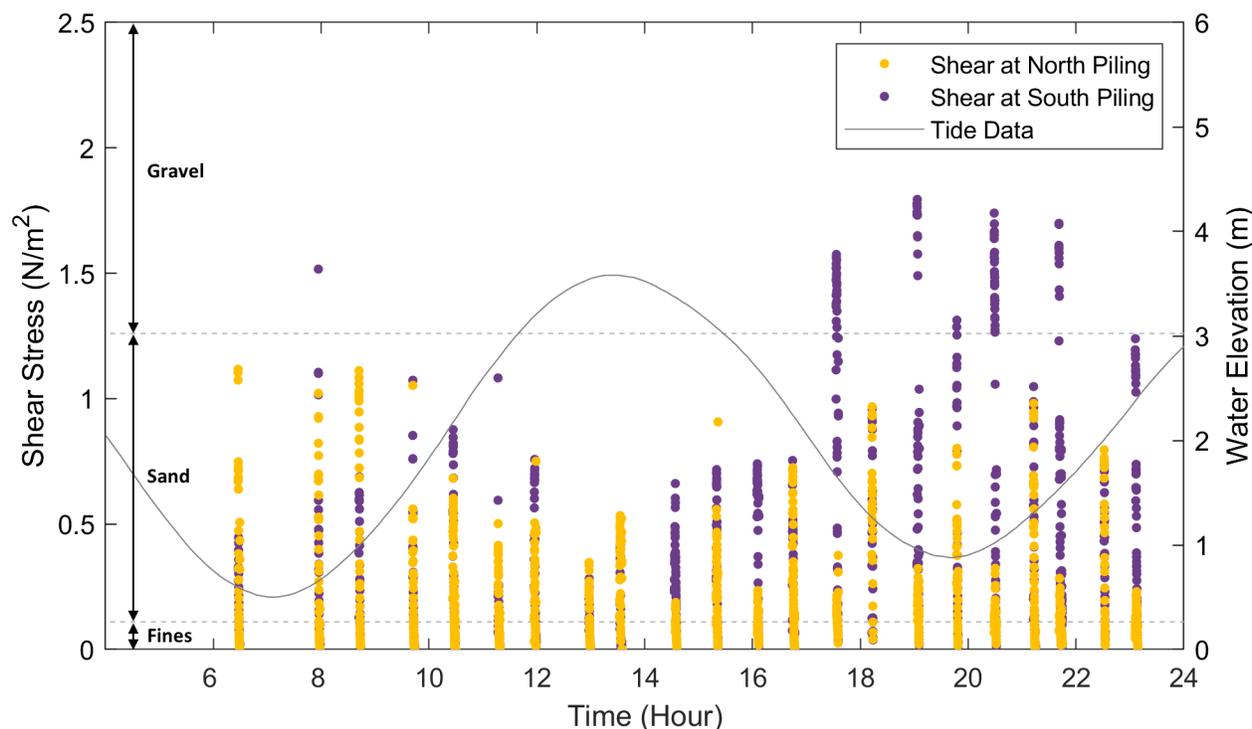
Figure 6.27: Simulated bottom shear stress at north and south pilings, tide data, and critical shear stress ranges for each sediment size classification.

Acknowledgments

References

Blaauw, H. G. and van de Kaa, E. J. Erosion of bottom and sloping banks caused by the screw race of manoeuvring ships. Technical Report 202, Delft Hydraulics Laboratory, Delft, Netherlands, 1978.

Chadwick, D. B., Rivera-Duarte, I. D., Rosen, G., Wang, P. F., Santore, R. C., Ryan, A. C., Paquin, P. R., Hafner, S. D., and Choi, W. Demonstration of an integrated compliance model for predicting copper fate and effects in DoD harbors. Technical Report ER-0523, Space and Naval Warfare Systems Center Pacific, San Diego, CA, United States, 2008.

Chou, P. Y. On velocity correlations and the solutions of the equations of turbulent fluctuation. *Quarterly of Applied Mathematics*, 3(1):38–54, 1945.

Damen Shipyards. Design of Safety Standby Vessel 4711, 2021. URL https://products.damen.com/en/ranges/safety-standby-vessel/ssv-4711. [Online; accessed: 05.01.2021].

DSI. EFDC+ Theory Document, 2020. URL https://www.eemodelingsystem.com/wp-content/uploads/EFDC_Theory_Document_Ver_10.2_2020.05.21.pdf. [Online; accessed: 08.01.2021].

Finlayson, D. P. Combined bathymetry and topography of the Puget Lowland, Washington State. Technical report, School of Oceanography, University of Washington, WA, 2005. URL https://www.ocean.washington.edu/data/pugetsound/psdem2005.html.

Fuehrer, M. and Römisch, K. Effects of modern ship traffic on inland and ocean waterways and their structures. *Permanent International Association of Navigation Congresses (PIANC)*, 24:79–94, 1977.

Garcia, M. H., Admiraal, D. M., and Rodriguez, J. F. F. Sediment entrainment functions for navigation-induced resuspension. Technical Report HES 61, Department of Civil and Environmental Engineering, University of Illinois at Urbana-Champaign, IL, 1999.

Gucinski, H. Sediment suspension and resuspension from small craft induced turbulence. Technical Report EPA-600/S3-82-084, United States Environmental Protection Agency, 1982.

Hamill, G. A. *Characteristics of the screw wash of a manouvering ship and the resulting bed scour*. PhD thesis, Queen's University of Belfast, 1987.

Hamill, G. A. and Kee, C. Predicting axial velocity profiles within a diffusing marine propeller jet. *Ocean Engineering*, 124:173–265, 2016.

Hamill, G. A., Kee, C., and Ryan, D. 3D efflux velocity characteristics of marine propeller jets. *Proceedings of the ICE - Maritime Engineering*, 168(2):62–75, 2015.

Hashmi, H. N., Ghumman, A. R., Hamill, G. A., and Stewart, D. P. J. Propeller-wash induced erosion and methods for its prediction. *Technical Journal*, 12:29–37, 2007.

Hong, J. H., Chiew, Y. M., and Cheng, N. S. Scour caused by a propeller jet. *Journal of Hydraulic Engineering, ASCE*, 139(9), 2013.

Hong, J. H., Chiew, Y. M., Hsieh, S. C., Cheng, N. S., and Yeh, P. H. Propeller jet–induced suspended-sediment concentration. *Journal of Hydraulic Engineering, ASCE*, 142, 2016.

Jiang, J., Lam, W., Cui, Y., Zhang, T., Sun, C., Guo, J., Ma, Y., Wang, S., and Hamill, G. Ship twin-propeller jet model used to predict the initial velocity and velocity distribution within diffusing jet. *KSCE Journal of Civil Engineering*, 23, 2019.

Jones, C. A. and Lick, W. SEDZLJ: A sediment transport model. Technical report, University of California, Santa Barbara, California, 2001.

Julien, P. Y. *River Mechanics*. Cambridge University Press, 2002.

Kastner, S. E., Stearns, C., Horner-Devine, A. R., and Thomson, J. M. Ferry vessel propeller wash effects on scour at the Kingston ferry terminal (WA, USA). Technical Report WA-RD 899.1, Washington State Department of Transportation, United States, 2019.

Kim, S. C., Friedrichs, C. T., Maa, J. P. Y., and Wright, L. D. Estimating bottom stress in tidal boundary layer from acoustic doppler velocimeter data. *Journal of Hydraulic Engineering, ASCE*, 126, 2000.

Lam, W., Hamill, G. A., Song, Y. C., Robinson, D. J., and Raghunathan, S. A review of the equations used to predict the velocity distribution within a ship's propeller jet. *Ocean Engineering*, 38(1):1–10, 2011.

MAN. *Basic Principles of Ship Propulsion*. MAN Energy Solutions, 2018.

Maynord, S. T. Interim report for the upper Mississippi River - Illinois waterway system navigation study: Physical forces near commercial tows. Technical Report 19, US Army Corps of Engineers, 2000.

Michelsen, T. C., Boatman, C. D., Norton, D., Ebbesmeyer, C. C., and Francisco, M. D. Transport of contaminants along the Seattle waterfront: effects of vessel traffic and waterfront construction activities. *Water Science and Technology*, 37:9–15, 1998.

NYSDOT. Newtown Creek navigation analysis: Kosciuszko Bridge project. Technical report, New York State Department of Transportation, 2005.

PIANC. *Guidelines for Protecting Berthing Structures from Scour Caused by Ships*. Permanent International Association of Navigation Congresses Secrétariat Général, 2015.

Stewart, D. P. J. *Characteristics of a ship's screw wash and the influence of quay wall proximity*. PhD thesis, Queens University Belfast, 1992.

Thanh, P. H. X., Grace, M. D., and James, S. C. Sandia National Laboratories Environmental Fluid Dynamics Code: Sediment transport user manual. Technical Report SAND2008-5621, Sandia National Laboratories, 2008.

Toutant, W. T. Mathematical performance models for river tows. In *Winter Meeting, Great Lakes and Great Rivers Section*. Society of Naval Architects and Marine Engineers, Clarksville, IN, 1982.

TugboatInformation.com. Tugboat Information, 2021. URL https://www.tugboatinformation.com. [Online; accessed: 03.01.2021].

van Rijn, L. C. Sediment transport, Part I: Bed load transport. *Journal of Hydraulic Engineering, ASCE*, 110(10):1431–1456, 1984a.

van Rijn, L. C. Sediment transport, Part II: Suspended load transport. *Journal of Hydraulic Engineering, ASCE*, 110(11):1613–1641, 1984b.

van Rijn, L. C. Sediment transport, Part III: Bed forms and alluvial roughness. *Journal of Hydraulic Engineering, ASCE*, 110(12):1733–1754, 1984c.

Verhey, H. J., Blokland, T., Bogaerts, M. P., Volger, D., and Weyde, R. W. Experiences in the

Netherlands with quay structures subjected to velocities created by bow thrusters and main propellers of mooring and unmooring ships. *Permanent International Association of Navigation Congresses (PIANC)*, 58:69–88, 1987.

Voulgaris, G. and Trowbridge, G. H. Evaluation of the acoustic doppler velocimeter (adv) for turbulence measurements. *Journal of Atmospheric and Oceanic Technology*, 15, 1998.

Wang, P. F., Rivera-Duarte, I. D., Richter, K., Liao, Q., Farley, K., Chen, H. C., Germano, J., Markillie, K., and Gailani, J. Evaluation of resuspension from propeller wash in DoD harbors. Technical Report ER-201031, Space and Naval Warfare Systems Center, San Diego, CA, United States, 2016.